ALMA MATER STUDIORUM
UNIVERSITÀ DI BOLOGNA

DOTTORATO DI RICERCA IN

Automotive Engineering for Intelligent Mobility

Ciclo 37

Settore Concorsuale: 09/E2 - INGEGNERIA DELL'ENERGIA ELETTRICA

Settore Scientifico Disciplinare: ING-IND/32 - CONVERTITORI, MACCHINE E AZIONAMENTI ELETTRICI

OPTIMIZED ELECTRIC MOTOR TECHNOLOGIES FOR SUSTAINABLE MOBILITY

Presentata da: Giampaolo Devito

Coordinatore Dottorato
Davide Moro

Supervisore
Davide Barater

Co-Supervisore
Stefano Nuzzo

Esame finale anno 2025

TABLE OF CONTENTS

LIST OF FIGURES

LIST OF TABLES

LIST OF ACRONYMS

AC	Alternating Current
ASM	Asynchronous Motor
CFD	Computational Fluid Dynamics
EV	Electric Vehicle
FE	Finite Element
FSAE	Formula Society of Automotive Engineers
IPM	Interior Permanent Magnet
MOGA	Multi-Objective Genetic Algorithm
PM	Permanent Magnet
PMaSynRM	Permanent Magnet-Assisted Synchronous Reluctance Motor
PMSM	Permanent Magnet Synchronous Motor
PWM	Pulse With Modulation
RE	Rare Earth
SPM	Surface Permanent Magnet
SRM	Switched Reluctance Motor
SynRM	Synchronous Reluctance Motor
WRSM	Wound Rotor Synchronous Motor

ABSTRACT

The urgency for a shift towards sustainable automotive technologies is indisputably a priority in the current global context, characterized by severe environmental challenges and a growing scarcity of critical resources. This doctoral thesis delves into the exploration of high-efficiency electric machines that reduce or eliminate the use of rare materials, thus promoting the principles of a circular and sustainable economy. At its core, the work presents an in-depth analysis and a series of proposals in the design of electric motors for vehicles, aiming to overcome traditional dependencies on rare-earth-based materials with more environmentally friendly solutions.

The focal point of the thesis is the development of valid technological strategies for designing electric motors that integrate optimized design techniques to enhance performance and reduce environmental impact. Various approaches to motor design for automotive applications are analysed, extending the discussion to critical usage contexts such as high-performance racing vehicles and heavy-duty equipment for mining. This treatment demonstrates the flexibility and scalability of the proposed solutions, highlighting their applicability across a broad range of transportation scenarios.

Methodologically, the thesis adopts an interdisciplinary approach that uses advanced computational modelling to evaluate the effectiveness of new motor configurations. This rigorous technical analysis confirms the operational feasibility and efficiency of the proposed systems laying the groundwork for a critical discussion on their performance compared to traditional systems.

In summary, this academic work contributes to the debate on sustainable automotive technologies and offers a cutting-edge design vision for the future of propulsion systems. The solutions presented are configured as pragmatic and effective alternatives to meet the need for a greener and more responsible automotive industry. Ultimately, the thesis establishes a benchmark for further research and technological developments, aiming to solidify the foundations for a new generation of electric motors that will be central to achieving a globally sustainable automotive ecosystem.

ABSTRACT (ITALIANO)

L'urgenza di una transizione verso tecnologie automobilistiche sostenibili è indiscutibilmente una priorità nell'attuale contesto globale, segnato da gravi sfide ambientali e dalla crescente scarsità di risorse critiche. Questa tesi di dottorato esplora la progettazione di macchine elettriche ad alta efficienza che riducono o eliminano l'uso di materie rare, promuovendo così i principi di un'economia circolare e sostenibile. Al centro del lavoro vi è un'analisi approfondita e una serie di proposte per la progettazione di motori elettrici per veicoli su ruota, mirate a superare la dipendenza tradizionale da materiali a base di terre rare mediante soluzioni più abbondanti ed ecologiche.

Il cuore della tesi è lo sviluppo di strategie tecnologiche valide per progettare motori elettrici che integrino tecniche di design innovative e ottimizzate, al fine di migliorare le prestazioni e ridurre l'impatto ambientale. Vengono analizzati vari approcci alla progettazione di motori per applicazioni automobilistiche, estendendo la discussione a contesti d'uso critici come veicoli da corsa ad alte prestazioni e attrezzature pesanti per l'estrazione mineraria. Questo approccio dimostra la flessibilità e la scalabilità delle soluzioni proposte, evidenziando la loro applicabilità in una vasta gamma di scenari industriali.

Dal punto di vista metodologico, la tesi adotta un approccio interdisciplinare che attraverso una modellazione computazionale avanzata valuta l'efficacia delle nuove configurazioni presentate. Tale analisi confermano la fattibilità operativa e l'efficienza dei sistemi proposti, ponendo le basi per una discussione critica sulle loro prestazioni rispetto ai sistemi tradizionali.

In sintesi, questo lavoro accademico apporta un contributo significativo al dibattito sulle tecnologie automobilistiche sostenibili e offre una visione progettuale all'avanguardia per il futuro dei sistemi di propulsione. Le soluzioni presentate si configurano come alternative pragmatiche ed efficaci per rispondere alla necessità di un'industria automobilistica più verde e responsabile. Infine, la tesi stabilisce un punto di riferimento per ulteriori ricerche e sviluppi tecnologici, con l'obiettivo di consolidare le fondamenta per una nuova generazione di motori elettrici che saranno centrali nel raggiungimento di un ecosistema automobilistico sostenibile a livello globale.

1. INTRODUCTION

1.1 Background and Motivation

The automotive industry is undergoing a transformative shift towards sustainability, driven by the global imperative to reduce carbon emissions and diminish the reliance on finite resources. Among the challenges faced is the dependency on RE elements, which are extensively used in the manufacturing of traditional electric propulsion systems. While these elements enhance motor performance, they also pose significant concerns due to environmental degradation, geopolitical tensions, and supply chain vulnerabilities associated with their extraction and processing.

EVs represent a pivotal advancement in sustainable transportation. However, the environmental sustainability of EVs can be compromised by the reliance on RE materials, creating a critical need for developing alternative motor technologies that either eliminate or substantially reduce the use of these materials. This situation presents a paradox where the vehicles intended to be part of the solution to environmental issues also contribute to them through their production processes.

Recent developments in materials science and engineering have facilitated the exploration of high-efficiency electric machines that minimize or completely avoid the use of RE elements. These innovations are crucial for leading the automotive industry towards more sustainable practices, in line with the principles of the circular economy, which emphasizes the reuse, recycling, and longevity of materials to minimize waste and reduce the continual extraction of raw resources.

The dual focus of this thesis is to develop new electric motor designs that significantly reduce or eliminate the dependency on RE materials [1]-[9]. This research aims to contribute to the automotive industry's transition to technologies that are not only environmentally friendly but also economically viable and technologically sound. The expected outcomes include viable motor designs that can meet the rigorous performance standards required by contemporary vehicles while using minimized quantities of rare materials.

This research is further justified by the global push towards the electrification of transport systems, with governments and industries setting ambitious targets for reducing greenhouse gas emissions. The rising demand for innovative and

sustainable technologies in the automotive sector underscores the relevance and timeliness of this thesis. It seeks to provide actionable insights and scalable technologies that can be leveraged to accelerate the transition towards sustainable automotive solutions.

In summary, the motivation behind this thesis is to develop electric motor technologies that not only reduce the environmental impact associated with the use of RE elements but also enhance the overall sustainability of electric vehicles. This research endeavours to address the technological gaps and expand the knowledge base, paving the way for the adoption of more sustainable electric motor technologies in the automotive industry.

1.2 Thesis objectives

The primary objective of this doctoral thesis is to develop electric motor designs that significantly reduce or eliminate the reliance on RE materials, in alignment with global sustainability goals across the automotive, mining, and aerospace sectors. The research focuses on optimizing existing motor topologies for various transportation sectors to achieve environmentally sustainable designs. The specific objectives of the thesis are structured as follows:

1.2.1 Optimization of Existing Motor Designs

- Material Substitution: Explore alternative materials to reduce the dependency on RE elements in established motor topologies. This includes the application of ferrite magnets and enhanced designs of WRSMs to maintain performance standards.
- Design Adaptation: Adapt and refine existing motor designs to fit specific applications in the automotive, mining, and aerospace sectors, ensuring they meet the required performance specifications while using fewer critical materials.

1.2.2 Performance Improvement

- Optimization through Simulations: Use FE analysis, to optimize motor designs and ensure that they meet the required performance benchmarks in terms of torque density, power output, and thermal management.

1.2.3 Contribution to Academic and Industrial Knowledge

- Dissemination of Research Findings: Share the research findings through publications in peer-reviewed journals, presentations at conferences, and participation in workshops. This will contribute to the academic knowledge base and support further developments in the field.
- Knowledge Transfer to Industry: Collaborate with industry stakeholders to ensure that the research outcomes are aligned with practical industry needs and can be effectively implemented in real-world applications.

By achieving these objectives, the thesis aims to provide a substantive contribution to the field of sustainable electric motor technology, offering practical and scalable solutions that can be adopted across multiple sectors to achieve environmental and performance targets.

1.3 Structure

The thesis is organized into ten chapters, each addressing specific aspects of the research on developing sustainable electric motor technologies with a focus on reducing or eliminating RE materials across various applications. The structure is as follows:

1.3.1 Chapter 1: Introduction

This chapter outlines the motivations and challenges related to the use of RE materials in electric motors, particularly in the automotive industry. It sets the context for the research objectives aimed at developing more sustainable motor technologies and defines the scope of the thesis.

1.3.2 Chapter 2: Literature Review

This chapter provides an overview of the current state of electric motor technologies, with a specific focus on the use of RE materials and their alternatives. It discusses the environmental, economic, and technical issues associated with these materials and identifies gaps in the existing research that this thesis aims to address.

1.3.3 Chapter 3: Methodological Framework and Trends in Sustainable Electric Motor Technologies

This chapter combines the methodological framework developed for the research with an analysis of technological trends in electric motors. It describes the research approach, simulation tools and design strategies used to reduce the reliance on rare-earth materials.

1.3.4 Chapter 4: Methodology and Example Case Studies

This chapter presents a series of case studies that illustrate the methodology applied in the research. These examples showcase the application of design and optimization techniques across various projects, serving as a reference for the development of sustainable motor solutions.

1.3.5 Chapter 5: Automotive Case Study on RE Reduction

This chapter focuses on specific case studies in the automotive sector, detailing the design and optimization of electric motors that significantly reduces the use of RE materials. The chapter highlights the technical challenges faced and the solutions implemented to achieve high performance while minimizing RE dependency.

1.3.6 Chapter 6: Rare-Earth-Free Electric Motor for a Mining Truck

This chapter presents a case study on the design and implementation of a completely RE-free electric motor for a mining truck. The chapter addresses the high torque and durability requirements unique to the mining industry and demonstrates the feasibility of sustainable motor solutions in such demanding environments.

1.3.7 Chapter 7: Aerospace Application Case Study

This chapter explores the design of a starter generator for the aerospace sector, where weight, size, and performance constraints are critical. The chapter details a case study that applies RE-reduced motor designs to meet the stringent requirements of aerospace applications, showcasing the versatility and scalability of the proposed solutions.

1.3.8 Chapter 8: Analysis of Excitation Systems

This chapter shifts the focus to a different, yet complementary aspect of electric machine design, exploring the development of a mathematical model to predict the performance of hybrid excitation systems of WRSMs. Although this topic is distinct from the motor design focus of earlier chapters, it provides valuable insights into the design of a peculiar electrical machine whose use is intended for power generation on board of vehicles such as aircraft, ships, etc.

1.3.9 Chapter 9: Conclusions and Future Work

This final chapter synthesizes the key findings from all the case studies and research presented, discussing their implications for the broader adoption of sustainable electric motor technologies. It outlines the contributions of the thesis to the field and suggests potential areas for future research, particularly in the further development and integration of RE-free solutions across various sectors.

2. LITERATURE REVIEW

2.1 The Shift Towards Sustainable Motor Design

The automotive industry has been increasingly driven by the need for sustainability, leading to significant advancements in electric motor technologies. Central to this transition is the reduction or elimination of RE materials, which, despite their effectiveness in enhancing motor performance, present serious environmental and economic challenges. As a result, recent research has focused on developing motor designs that align with global sustainability goals through the exploration of alternative materials and topologies [1]-[9].

2.2 Challenges Associated with Materials

RE elements (Fig. 1), known for their exceptional magnetic properties, are crucial in achieving the high efficiency and power density required in modern electric motors. However, their extraction and processing are associated with severe environmental degradation, including soil and water contamination, and their supply is concentrated in a limited number of countries, leading to significant geopolitical risks and market volatility [10][11]. These challenges have highlighted the urgent need for the automotive industry to reduce dependency on these materials and to explore alternatives that can maintain or even enhance motor performance.

Fig. 1. Exemplary image of RE materials.

2.3 Exploring Alternatives: Materials and Motor Designs

In response to these challenges, considerable research has been dedicated to identifying and implementing alternative materials that offer a more sustainable and cost-effective solution. Ferrite magnets, for instance, present an environmentally friendly option, though they traditionally lack the efficiency of RE magnets. To address this, researchers have also focused on reengineering motor designs, such as developing hybrid excitation systems which can achieve high performance with a reduced reliance on RE elements [12][13]. An example of hybrid excitation system for a WRSM is reported in Fig. 2.

The development of these alternatives is not merely a matter of substituting materials but also involves rethinking motor topologies to optimize performance. This includes innovations in rotor and stator design, where adjustments to configurations such as fractional slot concentrated windings and the use of advanced steel materials can lead to significant improvements in efficiency and power density [15]-[19]. These innovations reflect a broader trend in the industry towards creating more sustainable motor technologies that do not compromise on performance.

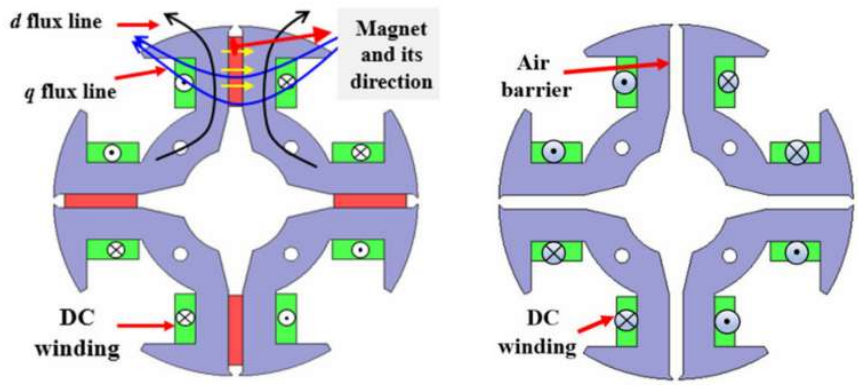

Fig. 2. Example of hybrid excitation system for a wound rotor synchronous motor from [13].

2.4 Improvements in Motor Topologies

The exploration of different motor topologies has been crucial in addressing the limitations of traditional designs that rely heavily on RE materials. ASMs, SRMs, and SynRMs (Fig. 3) have emerged as promising alternatives due to their ability to operate efficiently without these materials. These topologies offer benefits such as lower production costs, simpler manufacturing processes, and improved sustainability [20]-[22].

Significant advancements have been made in optimizing the design of these motors to enhance their performance. For instance, increasing the anisotropy of rotor structures and refining stator winding topologies have been shown to partially offset the reduction in torque and power density associated with the absence of RE materials. These innovations are critical in ensuring that the new motor designs can meet the high standards of efficiency and performance required in the automotive industry [13]-[23].

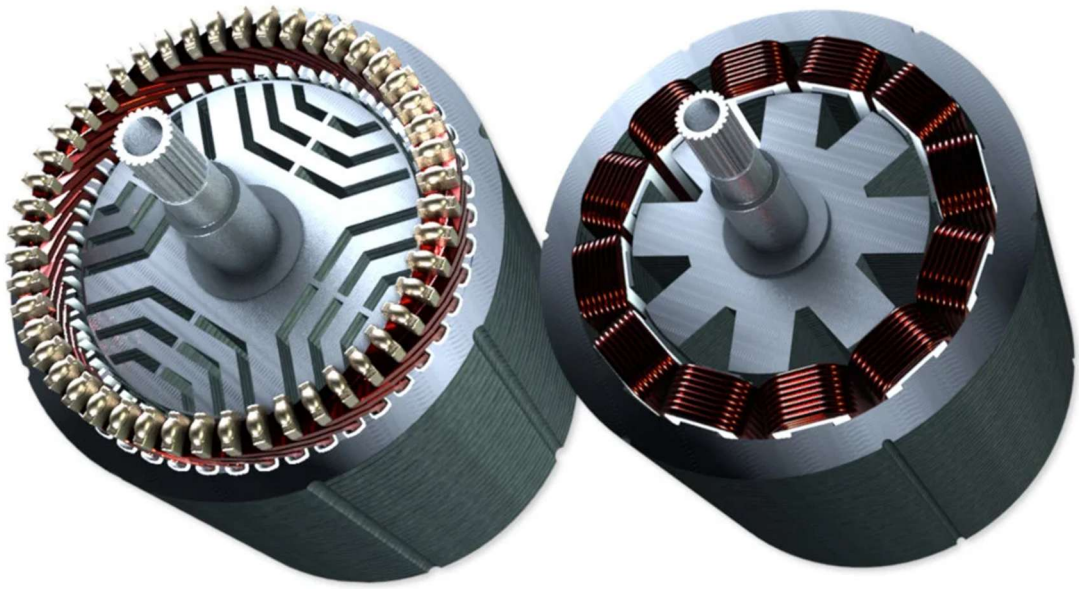

Fig. 3. Examples of synchronous reluctance motors (left) and switched reluctance motor (right).

2.5 Advancements in Wound Rotor Synchronous Motors

Would Field Synchronous Motors (WRSMs) represent a key area of development in the quest to create more sustainable and high-performing electric motors. WRSMs offer several advantages, particularly in applications where precise control of the excitation system is required, allowing for greater flexibility in achieving desired performance characteristics. Unlike traditional PM motors, WRSMs do not rely on RE materials, making them a more environmentally and economically sustainable option [4],[12]-[32].

The versatility of WRSMs lies in their ability to operate efficiently across a wide range of speeds and loads, making them suitable for demanding applications such as heavy-duty vehicles and industrial machinery. Recent advancements in WRSM technology have focused on improving the rotor design to enhance torque density and reduce losses, thus addressing some of the traditional drawbacks of this motor

type, such as higher losses and complex control requirements. Furthermore, innovations in excitation systems and cooling mechanisms have significantly improved the overall efficiency and reliability of WRSMs, positioning them as a viable alternative to more conventional motor designs in both automotive and industrial sectors [49].

2.6 The Role of Advanced Simulation Tools

Advanced simulation tools have been instrumental in the development of these new motor designs. FE Analysis and CFD are extensively used to model and predict motor performance, allowing researchers to optimize designs before physical prototypes are created. These tools are particularly valuable in identifying potential issues related to electromagnetic behaviour, thermal management, and mechanical integrity, enabling more efficient and cost-effective development processes.

By integrating these simulation tools into the design process, researchers can iteratively refine motor designs, ensuring that they meet the desired performance criteria while minimizing the use of RE materials. This approach not only accelerates the development timeline but also reduces the environmental impact associated with prototyping and testing.

2.7 Conclusions

The advancements in electric motor technologies reflect a significant shift towards more sustainable practices within the automotive industry. This evolution is characterized by a strategic re-evaluation of materials and design processes to align with environmental sustainability goals while ensuring high performance. As the industry progresses, these innovations are expected to play a pivotal role in reducing environmental impact and enhancing the viability of electric vehicles. The ongoing research and development in this field will be critical in shaping the future of sustainable transportation, with electric motors at the forefront of this transformation [1]-[101].

3. Methodological Framework and Trends in Sustainable Electric Motor Technologies

3.1 Introduction

The evolution of electric motor technologies has been marked by a growing emphasis on sustainability, driven by the dual imperatives of reducing environmental impact and improving energy efficiency. This chapter combines the methodological framework developed for the research and an overview of market trends to provide a comprehensive foundation for the case studies analysed in subsequent sections.

The methodologies adopted in this research play a central role in addressing the challenges posed by traditional electric motor designs, particularly the reliance on RE materials. By integrating simulation tools, design strategies, and a structured research approach, this chapter contextualizes the technological advancements shaping the development of sustainable electric motors.

3.2 Methodological Framework

3.2.1 Literature Review and Research Approach

The development of innovative electric motor designs aimed at reducing or eliminating the use of RE materials required a methodical approach that combined theoretical analysis, computational modelling, and experimental validation. Initially, a thorough literature review was conducted to identify existing motor designs and the limitations associated with RE materials. This analysis revealed the need for alternative materials and motor topologies, guiding the selection of design strategies tailored to specific applications.

3.2.2 Advanced Simulation Tools

A central aspect of the methodology was the integration of advanced simulation tools to optimize motor performance. FE analysis was extensively used to simulate the electromagnetic, thermal, and structural behaviours of the motor designs. These simulations allowed for precise calculations of key performance parameters such as torque, power density, and efficiency. Thermal simulations identified potential hotspots and ensured effective heat dissipation, while structural analyses

confirmed the mechanical robustness of the designs under various stress conditions.

3.2.3 Design Strategies

Design strategies were focused on the optimization of motor topologies to reduce RE dependency without compromising performance. This involved refining rotor and stator configurations, such as employing fractional slot concentrated windings and optimized pole shapes to enhance efficiency and minimize torque ripple.

The methodology also emphasized a systematic approach to balancing performance and sustainability across different motor applications. For instance, WRSMs and PMSMs were developed to address the unique requirements of sectors like automotive, mining, and aerospace. Each design iteration was informed by rigorous simulation results, ensuring that the motors met the specific demands of their intended applications.

3.2.4 Future Experimental Validation

Although the research primarily relied on computational modelling, plans are in place for experimental validation of the prototypes. This future phase will involve comprehensive testing to evaluate torque output, efficiency, and thermal behaviour under real-world conditions.

The methodological framework established in this research demonstrates a holistic approach to addressing the challenges of sustainable electric motor design. By combining theoretical analysis and advanced simulation techniques this methodology lays a robust foundation for the development of next-generation electric motors.

3.3 Trends in Electric Motor Technologies

This section provides an extensive examination of key innovations and ongoing challenges in electric motor design ([2]-[4],[9],[16],[31]-[13],[33]-[54]). It highlights the broader context that sets the foundation for the following case studies, focusing on the critical technological advancements that include minimizing the use of rare materials and optimizing motor configurations.

The analysis presented here delves into how torque, speed, environmental factors, and cost constraints shape the optimization process of motor technologies across various applications. The section will continue by exploring the specific torque-

speed characteristics that are distinct to each vehicle category, such as passenger cars, racing vehicles, trucks, and tractors, demonstrating how these technical requirements influence the strategic choices in motor design and implementation. Each type of vehicle employs tailored motor technologies to enhance drivability and performance. For example, in high-performance sectors, innovative multi-motor systems are emerging as sophisticated solutions that cater to both consumer expectations and regulatory demands. In the case of motors designed for heavy-duty or challenging environments, advanced thermal management systems are integrated to improve durability and operational efficiency under rigorous conditions [8][30].

This review draws on insights from foundational and modern research to present a comprehensive overview of the evolving landscape of electric motor technology. It explores how these advancements are shaping the future of sustainable transportation by aligning performance improvements with environmental goals. By combining methodological rigor with practical insights, this chapter establishes a robust framework for analyzing and designing sustainable electric motor technologies.

3.3.1 Market Vehicles Overview

This section provides an overview of the torque-speed characteristics of the previously discussed categories of vehicles (passenger cars, trucks and tractors), offering market examples to illustrate the practical application of these concepts. The detailed analysis of the topological and technological choices for each vehicle type will be presented in the next sections, utilizing real-world projects as examples to further our understanding.

A. Passenger Cars

The categorization of passenger cars within the realm of electric vehicles can be strategically analyzed based on varying price ranges, which significantly influence the technological sophistication and performance characteristics. This segmentation into economic, mid-range, and high-end categories allows for a nuanced understanding of how different market segments address consumer needs and technical specifications.

1. Economic Segment: Typically features vehicles designed for urban commuting where cost-effectiveness and efficiency are paramount. Motors

in this segment, such as those used in the Citroën C-Zero and Renault Zoe, often prioritize lower operational costs and simplicity. For example, the Renault Zoe employs a WRSM, optimizing torque at lower speeds to enhance urban drivability [41][55].

2. Mid-Range Segment: Bridges affordability with enhanced performance. Vehicles like the Hyundai Ioniq Electric use IPM motor to provide a balance of efficiency and power suitable for longer commutes and suburban driving [36][42]. This segment starts to introduce more complex motor technologies that offer better performance metrics without significantly increasing the price.
3. High-End Segment: Focuses on luxury and high-performance vehicles where advanced motor technologies push the limits of electric motor capabilities. Examples include the Porsche Taycan Turbo S and Tesla Model S Plaid, which utilize sophisticated multi-motor setups to achieve high torque and speed, catering to performance enthusiasts [43][44]. The integration of cutting-edge technologies in these vehicles showcases the highest potential of electric motors in terms of speed and torque capabilities.

For each category five commercial examples are reported in Table I, with their motor topology, maximum torque and rotational speed.

Table I
EXAMPLE OF PASSENGER CARS PER CATEGORY

Model	Motor Type	Torque (Nm)	Speed (rpm)
Economic Segment			
Citroën C-Zero	IPM	196	8000
Renault Zoe	WRSM	245	11000
Fiat 500 Electric	IPM	220	12000
Skoda Citigo-e iV	IPM	210	8000
SEAT Mii Electric	IPM	212	9000
Mid-Range Segment			
Chevrolet Bolt EUV	IPM	360	9000
Hyundai Ioniq Electric	IPM	295	10000
Kia Niro EV	IPM	395	11000
Nissan Leaf e+	IPM	340	10000
VW e-Golf	IPM	290	12000

High-End Segment			
Jaguar I-PACE	IPM	696	13000
Mercedes-Benz EQS	IPM	855	13000
Porsche Taycan Turbo S	IPM	1050	16000
Tesla Model S Plaid	IPM	1300	20000
Rimac C_Two	IPM	2300	18000

B. Racing Cars

Racing cars represent a specialized category profoundly shaped by the unique requirements of various championship regulations and budgets. This means that these vehicles could be both tailored for maximum performance, incorporating advanced motor technologies to achieve extraordinary power output, torque, and efficiency in competitive environments and be the best compromise between performance and cheapness where the budgets are extremely low.

The following table presents key specifications of motors used in several prominent electric racing championships, illustrating the performance of electric motors these competitive contexts.

Table II
EXAMPLE OF RACING CHAMPIONSHIPS AND SPECIFICATIONS

Championship	**Motor Type**	**Torque (Nm)**	**R. Speed (rpm)**
FSAE	WRSM	Up to 300	Up to 15000
Formula E	IPM	Up to 320	Up to 20000
Jaguar I-PACE eTROPHY	IPM	Up to 696	Up to 13000
Electric GT Championship	IPM	Up to 660	Up to 16000
Extreme E	IPM	Up to 920	Up to 15000

C. Heavy-duty Vehicles: Trucks

As the demand for sustainable heavy-duty transport solutions increases, the development and application of robust electric motors have become critical in addressing the unique challenges faced by this segment [4][34][50]. Heavy-duty vehicles such as trucks require motors capable of delivering high torque at relatively low speeds, crucial for hauling heavy loads and ensuring efficient operation over long distances and high reliability required by the harsh operating conditions even in mining environments.

This segment benefits from the implementation of advanced IPMs, Induction Motors (IMs) and WRSMs, with the latter being particularly valued for their ability to operate without RE materials, aligning with sustainability goals.

The table below illustrates some examples of cargo and mining trucks and their motor specifications.

Table III
EXAMPLE OF TRUCKS AND SPECIFICATIONS

Model	Motor Type	Torque (Nm)	Speed (rpm)
Cargo Trucks			
Renault Trucks D Z.E.	IPM	900	11000
Volvo VNR Electric	IPM	5500	11000
Tesla Semi	IPM/WRSM	5400	20000
MAN eTGM	WRSM	3100	6000
Nikola Tre	IPM	4300	10000
Mining Trucks			
Hitachi EH4000AC-3	IM	7700	2100
Komatsu 930E-5	IM	6400	2100
Liebherr T 236	IM	10000	2500
BelAZ 7558E	IPM	8800	2000
Caterpillar 798	IM	3500	2100

D. Heavy-duty Vehicles: Tractors

The ongoing advancements in electric motor technology, coupled with a strong emphasis on reducing environmental impact, are setting the stage for broader adoption of these technologies in all sectors. The agricultural sector is also embracing electric technologies, with tractors being at the forefront of this transition [50]-[53]. Electric tractors offer a sustainable alternative to traditional diesel engines, providing farmers with a cleaner and more efficient means of managing agricultural tasks.

In Table IV are some electric tractors currently on the market, along with their traction motor specifications.

Table IV
EXAMPLE OF TRACTORS AND SPECIFICATIONS

Model	Motor Type	Torque (Nm)	Speed (rpm)
Fendt e100 Vario	IPM	650	3000

John Deere SESAM	IPM	400	2500
SDF Group e-Tractor	IPM	800	3500
Kubota LXe-261	IPM	500	2000
Monarch Tractor	IPM	700	3000

Future chapters will delve deeper into the real-world applications and case studies that illustrate these technologies in action, providing a clearer picture of how electric motors will continue to evolve and shape the landscape of transportation and industry.

3.3.2 Practical Applications of Electric Motor Technologies Across Vehicle Segments.

In this chapter, a series of detailed case studies are presented, illustrating the critical design decisions such as motor topology, materials, and winding configurations, across the various segments of four-wheeled vehicles previously presented. These case studies highlight the trends and operational demands in the industry, demonstrating the practical application of the theoretical concepts previously discussed. The chapter is structured as follows: for each vehicle category, the specific needs are first outlined and then the case study is described in terms of motor topology choice, materials, and winding systems.

A. Economic segment

The electrification of the economic segment, primarily characterized by city cars, addresses the need for environmental sustainability by reducing urban pollutants. Several benefits for owners, such as access to restricted traffic zones and free parking, are designed to incentivize their adoption. The required performance for these vehicles is inherently limited in terms of torque and speed, proportional to the urban environment. Given the absence of high-performance requirements and the need for cost containment, the electric motor technologies utilized in these vehicles are not cutting-edge. Commercial solutions that are readily available and easily manufacturable are preferred, as evidenced by the example shown in Fig. 4, which presents the motor design proposed for a city car along with its torque-speed characteristic.

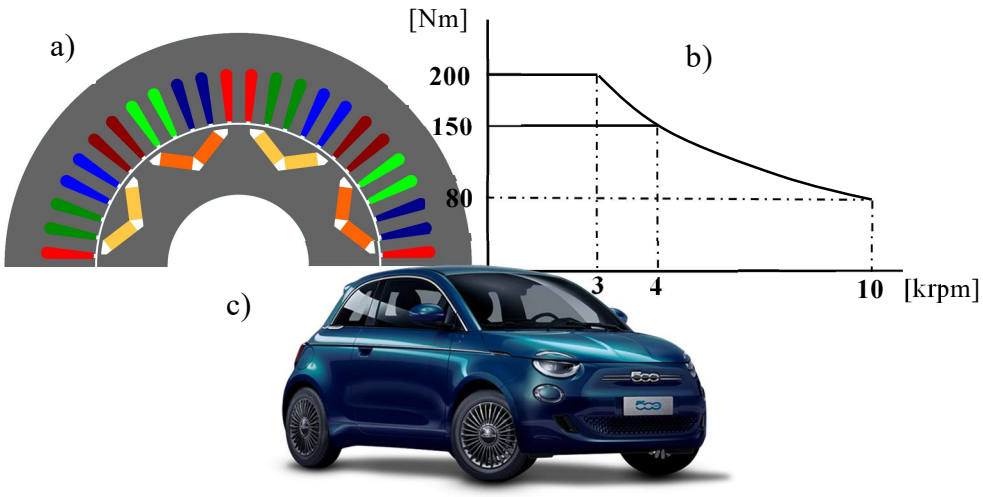

Fig. 4. a) A half of the FE model of the case study. b) Required torque-speed characteristic for the case study. c) Example of a city car (Fiat 500 Electric).

1. Motor Topology Selection

The torque-speed characteristic required opens up a range of potential solutions, including WRSM, IM, Synchronous Reluctance Motor (SynRM) and IPM. The selection is based on several considerations that lead to the exclusion of some topologies and the selection of the ideal candidate. Specifically, these vehicles need to have very reduced volumes, weights, and costs. Therefore, the adoption of a solution that minimizes volume and energy requirements, thus reducing battery pack size, is ideal. Among the candidates, the highest values of efficiency and torque density are achieved with the IPM motor. Despite the presence of RE elements, the choice of a simple design (Fig. 4a) and less expensive materials makes the solution economically viable. The IM, characterized by a lower cost, is excluded due to limited efficiency at the operating points of interest. Constraints on the absence of RE elements would make the WRSM the final choice for efficiency and controllability. However, the overall system cost would be higher, as evidenced by comparing the costs of vehicles in Table I, where the Renault Zoe, the only one with WRSM, has the highest starting price. The logic behind the materials and winding technology selection is discussed below.

2. Materials Selection

The selection of materials is also influenced by the reduced budget, leading to the choice of commercial materials. In the example case, a common Fe-Si steel sheet (M330_35A) with a thickness of 0.35 mm was used as a good compromise between minimizing losses in the stator and rotor cores due to hysteresis and eddy

currents and costs. Larger thicknesses would result in reduced efficiency values (< 90%) in some regions of the operating range. For the magnets, N30SH [54] was chosen for good torque density and availability.

3. Winding System Selection

For the winding system, classic round copper conductors were used, following the same logic specified above. The configuration used is a 4 pole-pair distributed in 48 slots with 2 slots per pole per phase. This solution ensures the achievement of the desired objectives in terms of torque, torque ripple, efficiency, and construction simplicity for cost minimization.

B. Mid-Range Segment

Designing propulsion systems for vehicles in the mid-range segment presents complex challenges, as each detail must strike an optimal balance between performance and cost-effectiveness. Moreover, environmental regulations increasingly influence these design decisions, mandating the adoption of specific technologies over others. The case study for the mid-range segment is exemplified by performance needs depicted in the torque-speed graph (refer to Fig. 5). This figure is consistent with a model currently available in the market within this category.

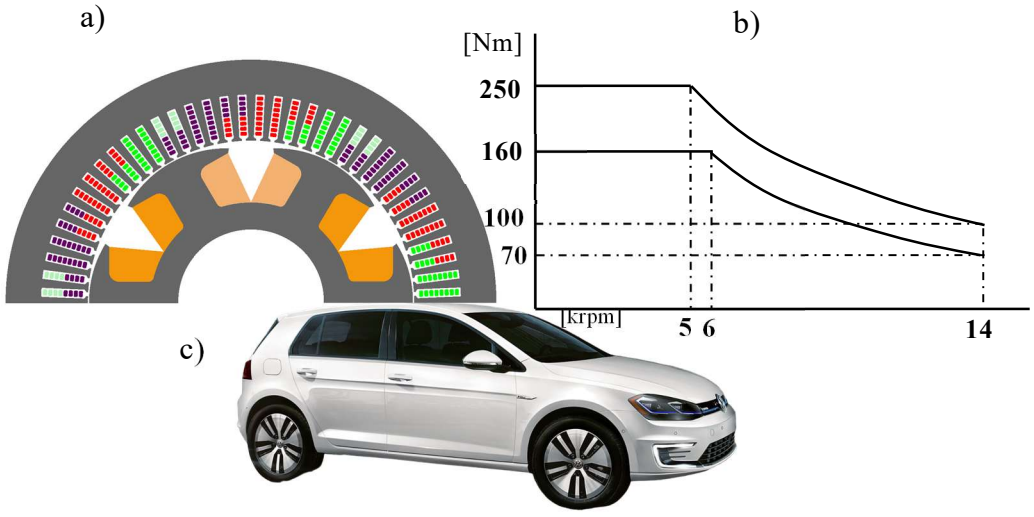

Fig. 5. a) A half of the FE model of the case study. b) Required torque-speed characteristic for the case study. c) Example of a mid-range car (VW e-Golf).

1. Motor Topology Selection

The project under review required careful consideration of several critical factors: minimizing the use of RE elements, controlling production costs, and maximizing efficiency. Given these constraints, a maximum rotational speed not exceeding 15.000 rpm, and a higher budget compared to the economic segment, the WRSM emerged as the best option. The need to enhance efficiency across all operational points and the demagnetization risks inherent in PMaSynRM motors further solidified the choice of the WRSM over other topologies.

2. Materials Selection

The selection of materials is driven by both affordability and performance. In WRSM, thermal management is particularly complex due to the windings on the rotor. Thus, minimizing losses and maximizing performance, crucial for all electric machines, become especially important for ensuring high efficiency and maintaining temperatures compatible with the materials' insulation class. However, high-performance materials often come at a higher cost, potentially making the propulsion system incompatible with the vehicle segment's price range. Given that copper is the only viable choice for the windings within the operating range [47], the flexibility lies in the choice of materials and lamination thickness for the stator and rotor ferromagnetic cores. In this project, the optimal balance was achieved by using an electromagnetically efficient material (NO_35) with a lamination thickness of 0.35mm. Further reduction in thickness would significantly increase costs, while using more common materials like M330_35A would lead to reduced performance and efficiency.

3. Winding System Selection

The choice of the winding system is similarly driven by the need to balance maximizing performance, minimizing losses, and containing costs. A hairpin winding solution was selected, featuring 3 pole pairs and 72 slots, with 4 slots per pole per phase and a pitch shortening of 2. This configuration ensures an optimal distribution of the winding function, reducing harmonics causing iron losses and torque ripple. The selection of 3 pole pairs strikes a balance between minimizing the maximum electrical frequency, which affects the cost of power electronics and losses, and maximizing torque. Hairpins guarantee maximum torque densities by achieving a fill factor greater than 70%, and their optimized shape ensures higher

efficiency compared to round conductors at the vehicle's most frequently used operating points.

C. High-End Segment

Designing propulsion systems for the high-end vehicle segment not only allows for the integration of the most advanced technologies available on the market but also benefits from the more lenient economic constraints that characterize this category.

Environmental considerations hold less weight in this sector. This stems from the direct relationship between environmental sustainability and operational costs. By reducing the use of RE elements in production, significant cost reductions can be achieved due to the reduced expensive to the raw materials involved. Moreover, the mining and processing of these elements are known to have substantial ecological impacts. Thus, minimizing the use of RE elements not only cuts production costs but also diminishes environmental pollution. In the realm of hypercars and luxury vehicles, where budgetary constraints are less pressing compared to other segments, the push for RE-free solutions is not as strong. It is also worth noting that the production volumes in this elite segment are significantly lower, resulting in a minimal environmental footprint relative to other sectors. It can be added that, the pursuit of pure performance makes supercores (like Jnex900) and conductors such as Litz wire adoptable for this category. These advanced materials and winding configurations ensure that the motor meets the high performance and efficiency requirements typical of the high-end segment.

This section outlines the electric motor design for a hypercar propulsion system, which features a total maximum torque of 1040 Nm, distributed across four motors, one for each wheel. Fig. 6 displays the motor tailored for the rear axle of a high-end vehicle, complete with its projected torque-speed characteristics. Further details of the chosen solution are elaborated in subsequent subsections.

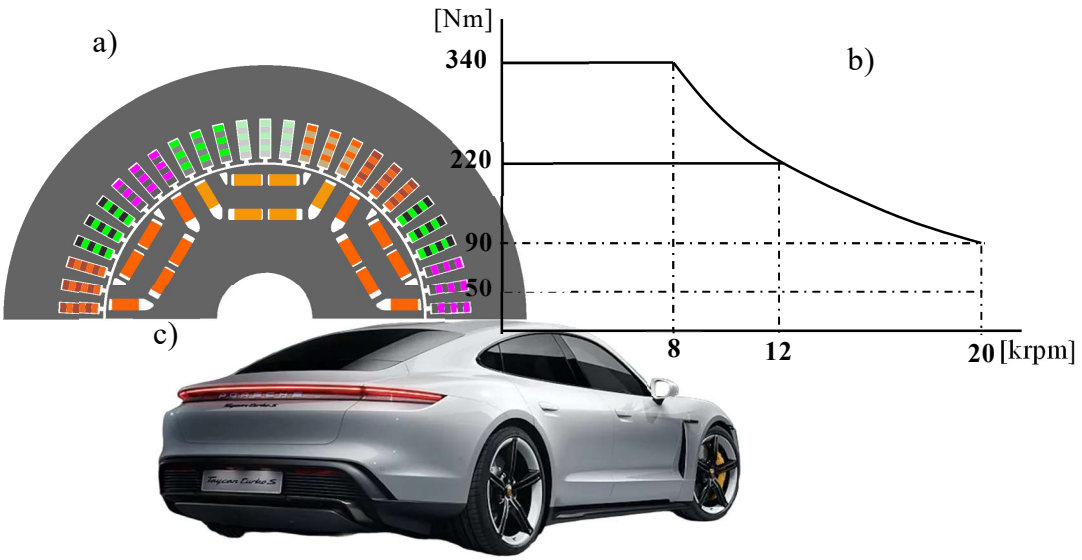

Fig. 6. a) A half of the FE model of the case study. b) Required torque-speed characteristic for the case study. c) Example of a high-end car (Porsche Taycan Turbo S).

1. Motor Topology Selection

The requisite torque-speed characteristics, efficiency exceeding 96% at key operational points, and rigorous thermal management, necessary for power levels nearing 1 MW, combined with a maximum speed of 20,000 rpm and requirements for reduced weight and space, necessitated the selection of an IPM solution featuring high-performance materials. Alternative topologies were deemed unsuitable as they failed to meet one or more of these stringent criteria. Specifically, IMs were dismissed due to their lower efficiency, while WRSMs were discounted due to thermal and structural challenges at high rotational speeds. However, research continues to adapt the WRSM for these demanding applications as well. (For the front axle, a more sustainable version of the rear axle motor was designed, capable of delivering a maximum torque of 180 Nm [3]).

2. Materials Selection

In the high-end segment, material selection is primarily guided by performance imperatives, allowing for the use of superior, high-performance materials. For instance, NO_20 was chosen with lamination thickness of 0.2 mm in both the rotor and stator ferromagnetic cores, complemented by N48H magnets. These materials are pivotal in maximizing torque, power density, and efficiency.

3. Winding System Selection

The winding system is designed to optimize performance and reduce losses. The need for high torque densities exceeding 10 Nm/kg, along with the goal of achieving high efficiencies to maximize the vehicle's range, necessitated the choice of an advanced hairpin winding system. This system features 54 slots and allocates 3 slots per pole per phase. The configuration is carefully chosen to limit the maximum electrical frequency of 1 kHz. This strategic setup ensures efficient power transmission while keeping electrical losses to a minimum.

D. Racing Cars

Designing electric motors for racing cars involves navigating unique challenges, as stringent and varied championship regulations impose specific demands. These racing categories range from contexts akin to the high-end segment to scenarios closely resembling the economic sector. This section offers an example of designing a propulsion system for a FSAE vehicle, demonstrating how these constraints influence design choices. The required torque-speed characteristics for each motor (Fig. 7) are tailored to the real-world demands of championship tests, with consideration given to the reduction ratios used.

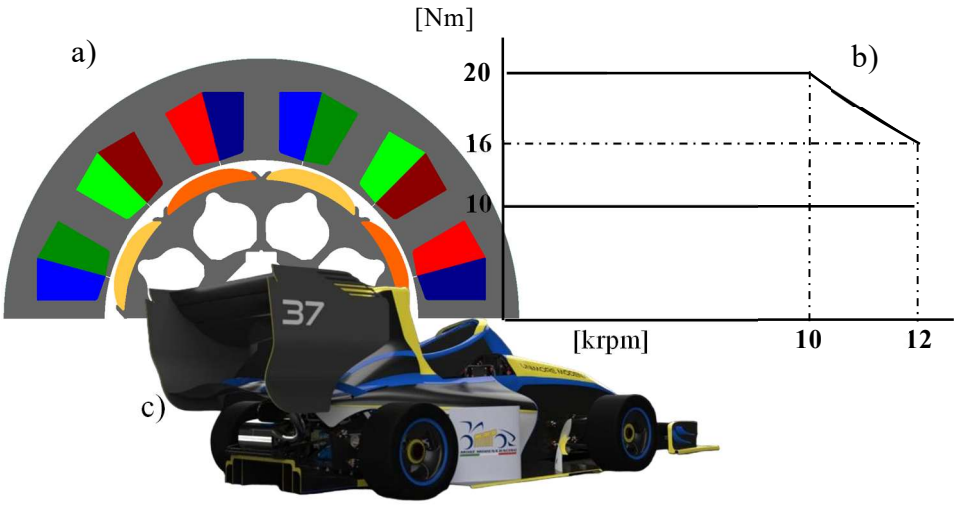

Fig. 7. a) A half of the FE model of the case study. b) Required torque-speed characteristic for the case study. c) Example of a FSAE racing car (Unimore FSAE car 2023).

1. Motor Topology Selection

The torque-speed characteristic, imperative for cost minimization, and the necessity to maximize efficiency to reduce battery pack size, are ideally suited to a SPM solution. The very narrow flux-weakening region, as illustrated in Figure

Y, mitigates the primary limitation of this motor type, enabling the harnessing of its full potential. This includes high efficiency associated with a nearly unity power factor, simplicity in both construction and control, and one of the highest torque densities available. In this context, environmental considerations are tackled through economic incentives. Specifically, the reduction in RE element usage, achieved through optimized motor geometry, is primarily driven by the need to lower costs associated with their acquisition. Additionally, production volumes are exceptionally limited; in this particular case, only three units were produced; one prototype for verification purposes and two motors for installation on the vehicle's rear axle. This limited production scale inherently minimizes the environmental impact.

2. Materials Selection

The selection of materials for the motor is strategically aimed at balancing cost efficiency with performance optimization. Specifically, silicon steel M350_50A, featuring a lamination thickness of 0.5 mm, was chosen for the rotor core, while M300_35A with a 0.35 mm thickness was selected for the stator. This choice was targeted to minimize costs while effectively containing iron losses. In SPM motors, the rotor core encounters very limited hysteresis and eddy currents, enabling the use of more economical and slightly lower-performing materials compared to those utilized in the stator. Despite prevailing economic considerations, SmCo magnet technology was employed to mitigate the risk of demagnetization, especially at maximum operating temperatures exceeding 140°C. This decision was also aimed at reducing the costs associated with the cooling system, thereby enhancing overall system efficiency and cost-effectiveness.

3. Winding System Selection

The dual objectives of minimizing costs and achieving satisfactory performance make the use of traditional round conductors alongside a concentrated three-phase winding system an appealing choice. This arrangement is designed to shorten the length of the end-windings, which in turn reduces both the quantity of copper required and the dimensions of the external casing. To further optimize this design, the electrical frequency is capped at 800 Hz through the selection of a 4 pole-pair

configuration. This carefully considered setup not only ensures cost-efficiency but also maintains the system's performance within desired parameters.

E. Heavy-duty vehicles: Cargo Trucks

The heavy-duty work vehicle sector is undergoing a robust transition toward electrification, similar to passenger cars but with distinct torque and speed requirements. It is usual for these vehicles to require torque exceeding 4000 Nm, albeit at generally lower rotational speeds with respect to cars. Environmental considerations are especially critical in this sector, propelling efforts to minimize or eliminate the use of RE elements in new models. There is also a concerted effort to leverage existing platforms to mitigate the economic impacts of these technological changes. The budgets for these motors typically allow for the adoption of fairly advanced technological solutions, ranging from mid to high-end specifications. This narrative is exemplified by a motor design for a cargo truck [34]. Fig. 8 illustrate the FE model, torque-speed characteristic, and vehicle example within this category, showcasing how the sector addresses the dual demands of performance and environmental stewardship.

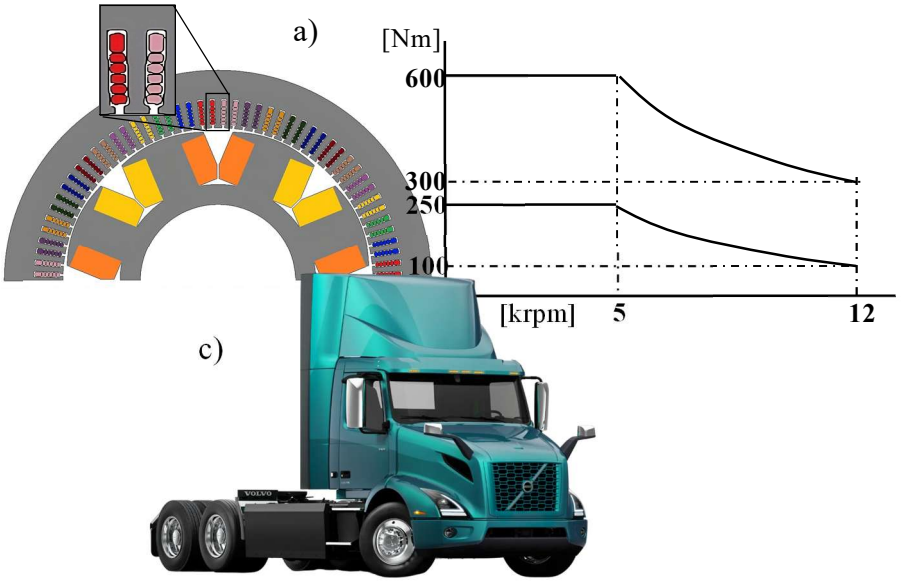

Fig. 8. a) A half of the FE model of the case study with a zoom-in of two slots. b) Required torque-speed characteristic for the case study. c) Example of a cargo truck (Volvo VNR Electric).

1. Motor Topology Selection

For the project under review, a solution devoid of RE elements that could achieve efficiency values exceeding 96% at certain operational points was mandated.

Among the various options considered, as detailed in section 3.A, the WRSM emerged as the preferred choice. This decision was influenced by the motor's extended overspeed capability and superior controllability through the adjustment of its two field sources, making this topology particularly effective for attaining high efficiency near the upper limits of rotational speeds. Such capabilities are crucial for extending the operational range, a key requirement for this category. Additionally, the selection of the winding system and materials was driven by the dual objectives of maximizing efficiency and bolstering environmental sustainability.

2. Materials Selection

The requirement for sustained rotational speeds throughout the motor's operational lifespan necessitated the use of NO_20 material, with a thickness of 0.2 mm for both the rotor and stator cores, to effectively minimize losses. For the conductors, an aluminum-based solution was chosen due to its lighter weight and high recyclability. This choice not only meets the performance criteria but also aligns with the project’s commitment to environmental sustainability, showcasing a conscientious approach to material selection that supports eco-friendly practices.

3. Winding System Selection

A hairpin winding system, featuring 6 phases, 96 slots, and 2 slots per pole per phase, was implemented to optimize performance in terms of power density and efficiency. Aluminum was selected for the conductors to meet specific recyclability objectives. This necessitated meticulous optimization of the winding system and pin dimensions to accommodate the properties of aluminum. Notably, the final pin in each slot is designed to be larger than the others (which are uniform in size). This strategic arrangement of the slot space is intended to reduce alternating current (AC) losses, thereby enhancing the overall efficiency of the system.

F. Heavy-duty vehicles: Mining Trucks

As the industry shifts away from the use of RE elements, mining trucks are at the forefront of adopting more sustainable propulsion systems. Traditionally, these vehicles have relied on robust and economical induction motors due to their durability and lower costs as highlighted in Table III. However, the trend is

increasingly towards adopting WRSMs. A notable example of this transformation is demonstrated by ABB [4], where a WRSM has been developed to replace an existing IPM traction motor on a mining truck. This transition aims to enhance the efficiency of the system. The project strategically preserved the original casing and cooling system to manage costs effectively. This transition exemplifies a broader trend where mining trucks, critical in heavy-duty applications, are moving towards solutions that balance economic, environmental, and performance demands effectively.

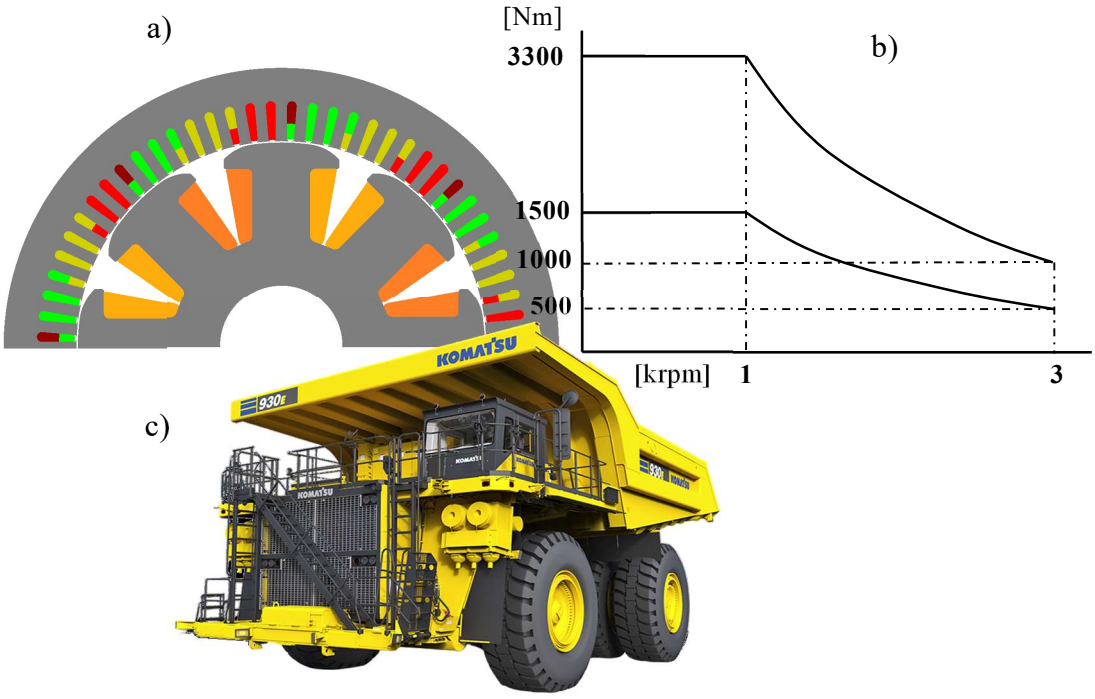

Fig. 9. a) A half of the FE model of the case study. b) Required torque-speed characteristic for the case study. c) Example of a mining truck (Komatsu 930E-5).

1. Motor Topology Selection

The selection of a WSRM, as highlighted earlier, is motivated by several key factors: the imperative to eliminate RE elements, the ability to achieve high controllability, and the attainment of high efficiency levels (exceeding 96%) at typical operating points for the application. In the specific case under review, the maximum rotational speed of less than 4000 rpm substantially mitigates the thermal and structural issues that are often associated with this motor topology, making it a particularly suitable choice for the demands of the application.

2. Materials Selection

The selection of materials was strategically guided by the need to meet efficiency requirements using the most commercially viable and cost-effective solutions available. Specifically, the target values were successfully met using M350_50A steel with a lamination thickness of 0.5 mm. This thickness was deemed appropriate due to the motor's low rotational speeds, which help reduce the generation of eddy currents and hysteresis losses in the ferromagnetic core. For the winding system, copper was chosen for its superior performance at low electrical frequencies, significantly enhancing the system's overall efficiency by minimizing losses.

3. Winding System Selection

The motor features a winding system composed of circular conductors arranged in parallel strands, a design choice aimed at balancing cost-effectiveness with performance. This configuration achieves a fill factor of approximately 50%. The economic rationale that guided the selection of laminations was also applied here, starting with an analysis of the most cost-effective technologies and progressing until the required performance benchmarks were met. The resulting configuration utilizes a distributed three-phase system, equipped with 4 pole pairs, 72 slots, and 3 slots per pole per phase. Additionally, a pitch shortening of 1 is implemented to minimize torque ripple, further optimizing the motor's performance.

G. Heavy-duty vehicles: Tractors

The agricultural sector is progressively embracing electric solutions, albeit at a slower pace compared to other industries. In agriculture, the potential for electrification extends beyond simple traction, encompassing a wider array of functions such as power take-offs (PTO), lifting, distribution, and heat pumps. These functions can sometimes be of equal importance and are often electrified independently. For instance, in tractors, the spectrum of electrification solutions ranges from single-motor systems, where one electric motor replaces the conventional thermal engine, to multi-motor configurations where individual motors power distinct functions. A notable example is the Goldoni B1E (Fig. 10), which is outfitted with five electric motors, each dedicated to a separate operational function. The choice between single and multi-motor setups largely depends on the available budget and the economic tier in which the product is

positioned. In terms of the technologies used for these electric motors, the agricultural sector does not prioritize high performance. Instead, the emphasis is on simplicity, availability, and cost-effectiveness. Consequently, the environmental concerns related to the use of RE elements are somewhat less critical in this context. The primary environmental benefit is derived from the transition to electrification itself. To illustrate, an example of a SPM motor designed for a tractor PTO is presented [50].

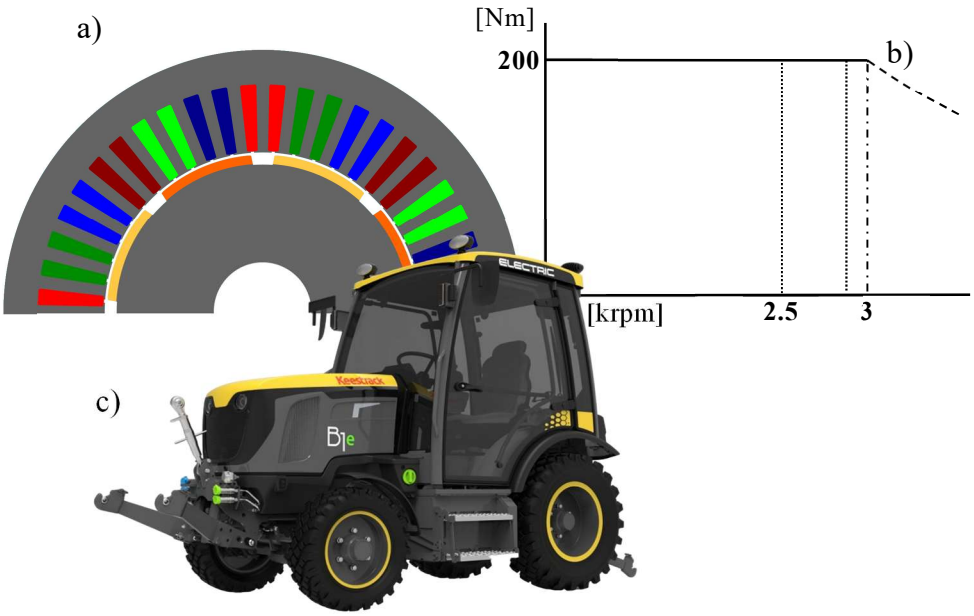

Fig. 10. a) A half of the FE model of the case study. b) Required torque-speed characteristic for the case study. c) Example of a tractor (Goldoni B1E).

1. Motor Topology Selection

Agricultural equipment utilizing PTOs typically operates at a fixed speed or within a very narrow speed range. In the specific case studied, the equipment connected to the PTO demands a rotational speed ranging from 2500 to 2900 rpm, considering reduction ratios. Given these requirements, the need for cost reduction and enhanced efficiency, coupled with the ability to operate nearly at a fixed speed and at relatively low speeds, makes the SPM motor an ideal solution. This configuration optimizes performance while aligning with the operational demands of agricultural machinery.

2. Materials Selection

The selection of materials adheres to the previously outlined strategy of minimizing costs by leveraging readily available commercial technologies, which

ensure satisfactory efficiency and adequate torque density. Consequently, M330_35A, featuring a lamination thickness of 0.35 mm, was chosen for the core material. For the magnets, N28UH was selected to complement the core, providing a balance between performance, cost, and availability. This combination effectively meets the operational demands of the application while adhering to budgetary constraints.

3. Winding System Selection

The winding system incorporates circular copper conductors, which are evenly distributed across 48 slots. This arrangement is designed to optimize electrical efficiency and ensure uniform torque production throughout the system's operation.

The main data of all presented case studies are summarized in Table V. Is then provided a high-level overview of the global technological trends for vehicles with four or more wheels as described.

3.3.3 Trends of Electric Motor Technologies

In the evolving landscape of electric motor technologies within the automotive industry, several trends emerge, particularly in the design and materials used in these motors. These developments are evident from the diverse applications and configurations detailed in various vehicle segments. Here's an overview of these trends according to the case studies.

1. Motor Topology and Pole Pairs: The choice of motor topology typically varies across different vehicle segments to meet specific performance requirements. Most electric motors, whether for economical city cars or high-performance racing cars, employ either IPM or WRSM for their balance of efficiency and performance. The number of pole pairs is commonly between 3 and 4 across the board, a configuration that offers an optimal balance between torque output and rotational speed without overly complex control strategies or excessive material costs.
2. Material Selection: There is a significant emphasis on the selection of materials that optimize efficiency while being cost-effective. Materials like M330 and M350 (SiFe laminations) are popular due to their favorable electrical properties, such as low resistance and high magnetic

permeability, enhancing overall motor performance. The thickness of laminations in these motors is often a compromise between minimizing eddy current losses and manufacturing costs, typically ranging from 0.35 to 0.5 mm. Enhanced performance are typically obtained through the usage of high-performance materials like NO_20, with typical thickness of 0.2 mm.

3. Winding Configurations: Hairpin windings are becoming increasingly common, particularly in high-performance and mid-range segments. This configuration helps reduce DC copper losses and allows for a more compact motor design, thereby improving the power density and efficiency of the motor. The choice between hairpin and traditional round wire windings is often dictated by specific performance requirements and cost constraints.

A higher-level overview of the global trends in electric motor technologies is provided below. Utilizing a comprehensive summary table, these technologies are categorized based on crucial parameters including budget, material and winding system technology levels, environmental sustainability, and performance. This methodical approach simplifies complex data, providing a clear and accessible schematic representation of the technological landscape.

A standardized star rating system enhances this analysis. The system classifies budget into three levels: economical, where the low initial cost makes vehicles accessible to a wide audience; moderate, which balances affordability with advanced functionality for everyday use; and high, requiring a significant initial investment justified by superior technologies and top-tier performance, often found in luxury or highly specialized vehicles. The technology level of materials follows a similar three-tier system: basic, using standard, easily accessible materials ideal for price-sensitive market segments; advanced, employing higher quality materials that offer better performance and durability; and cutting-edge, which involves state-of-the-art materials optimized for maximum performance and energy efficiency. The winding systems are also categorized by their sophistication from standard, suitable for less demanding applications, to optimized systems designed to maximize efficiency and minimize energy losses. Finally, environmental sustainability is assessed where basic levels indicate a reduced focus on environmental impact, good levels demonstrate active strategies to reduce ecological footprints, and excellent levels utilize technologies that not

only minimize environmental impacts but also pioneer sustainable solutions. The performance ratings mirror this structure, assessing how well the technologies meet varying demands from basic daily tasks to high-demand situations requiring superior performance. Through this narrative, the chapter aims to provide a comprehensive understanding of how electric motor technologies are tailored to meet diverse industry needs and sustainability goals (Table VI).

Table V
PERFORMANCE COMPARISON OF ELECTRIC MOTOR TECHNOLOGIES ACROSS THE CASE STUDIES

Specification	Economic Segment	Mid-Range Segment	High-End Segment	Racing Car	Cargo Truck	Mining Truck	Tractor (PTO)
Motor Topology	IPM	WRSM	IPM	SPM	WRSM	WRSM	SPM
Maximum Torque Tot. (Nm)	200	250	1040	40	2400	6600	200
Number of Motors	1	1	4	2	4	2	1
Max Rotation Speed (rpm)	10000	14000	20000	15000	12000	3000	3000
Number of Pole Pairs	4	3	3	4	4	4	4
Number of Phases	3	3	3	3	6	3	3
Number of Slots	48	72	54	12	96	72	48
Conductor Type	Round	Hairpin	Hairpin	Round	Hairpin	Round	Round
Core Material	M330	NO_35	NO_20	M330/350	NO_20	M350	M330
Lamination Thickness (mm)	0.35	0.35	0.2	0.35/0.5	0.2	0.5	0.35
Conductor Material	Cu	Cu	Cu	Cu	Al	Cu	Cu
Magnet Material	N30SH	--	N48H	SmCo_1040	--	--	N28UH

Table VI
PERFORMANCE COMPARISON OF ELECTRIC MOTOR TECHNOLOGIES ACROSS DIFFERENT VEHICLE SEGMENTS

Vehicle Category	Budget (★ to ★★★)	Materials (★ to ★★★)	Winding Systems (★ to ★★★)	Environmental Sustainability (★ to ★★★)	Performance (★ to ★★★)
Economic Segment	★	★	★	★ to ★★★	★
Mid-Range Segment	★★	★★	★★	★★	★★
High-End Segment	★★★	★★★	★★★	★ to ★★	★★★
Racing Cars	★ to ★★★	★ to ★★★	★ to ★★★	★ to ★★	★ to ★★★
Trucks	★★ to ★★★	★★ to ★★★	★★ to ★★★	★★ to ★★★	★★ to ★★★

Tractors	★ to ★★	★ to ★★	★ to ★★	★ to ★★	★★

3.3.4 Conclusions

The methodologies and approaches discussed so far have laid the groundwork for the practical application of these concepts in various real-world scenarios. In the following chapter, a selection of case studies will be presented, offering detailed insights into specific applications of multi-physics optimization and performance analysis in electric machine design.

To begin, two key studies will be explored. The first provides a comprehensive framework for multi-physics optimization, focusing on the electromagnetic and mechanical aspects of motor design, while the second offers a methodology for determining the torque-speed characteristics for specific applications, particularly in the context of vehicle performance. These foundational studies, along with others discussed later in the chapter, represent significant milestones in the development of high-efficiency, sustainable motor technologies.

4. BENCHMARK CASE STUDIES

Building on the work discussed in the previous chapter, this section presents a selection of the most significant case studies that shaped the core of this doctoral research. These studies represent key applications of the methodologies introduced earlier, alongside additional articles that have contributed to the development and validation of the proposed approaches.

The first case study, outlined in the article "Design of the Propulsion System for a FSAE Racing Car," ([9]) is crucial for understanding the methodology used to determine the torque-speed characteristics for a specific application and the consequent motor topology selection. This work demonstrates how the design and optimization processes are applied to meet the performance requirements of racing conditions by ensuring the correct integration of speed, torque, and power output based on the constraints and demands of the application.

The second case study, described in the article "Multi-Physics and Multi-Objective Optimization of a PMaSynRM for Traction Applications," ([3]) focuses on the optimization of a PMaSynRM machine, providing a detailed framework for multi-physics optimization. This study integrates electromagnetic, structural, and thermal considerations into the design process, illustrating how conflicting objectives—such as torque ripple reduction and mechanical robustness—can be harmonized to achieve improved overall performance.

These two case studies serve as foundational examples for the subsequent projects discussed in this chapter, which focus on innovative motor designs for hypercars, aerospace applications, and heavy-duty vehicles. Each project addresses the challenges of sustainability and the reduction of RE materials, further validating the methodologies employed throughout this research.

4.1. Design of the Propulsion System for a Formula SAE racing car based on a Brushless Motor

4.1.1 Introduction

The definition of torque-speed characteristics plays a pivotal role in the design and optimization of propulsion systems for FSAE racing vehicles. In these high-

performance and competitive environments, tailoring the motor's behavior to meet the specific demands of race conditions is essential for ensuring optimal performance. Establishing these characteristics is a key technical requirement and forms the foundation upon which subsequent design decisions are made, including motor topology, powertrain configuration, and material selection.

In racing applications, the ability of the propulsion system to deliver the required torque across a broad speed range is paramount. The correct identification and refinement of the torque-speed curve ensures that the motor can meet the dynamic acceleration, handling, and endurance challenges imposed by the competition. This process becomes even more critical when considering the constraints unique to FSAE, including strict budget limitations and the need for compact, lightweight designs that maximize power density. These constraints, combined with the rigorous demands of the competition, drive the search for innovative and efficient solutions that can deliver high performance while maintaining reliability and cost-effectiveness.

The design of electric motors for FSAE vehicles typically involves the consideration of several motor topologies. Among the most prominent solutions are PM synchronous machines, which are widely favored for their superior power density and efficiency. PM synchronous motors, especially those with surface-mounted rotor configurations, are known to offer high torque at low speeds, making them an ideal choice for applications where quick acceleration is critical [16][17]. However, the increasing cost and supply chain volatility of RE materials used in high-performance PM motors have led to a growing interest in alternative motor technologies.

One such alternative is the synchronous reluctance motor (SRM), which, when assisted by low-cost ferrite PMs, presents a viable solution to reducing reliance on expensive RE elements while still achieving adequate performance [20]. However, SRMs often face challenges due to torque ripple and lower power factors, making it essential to carefully balance these drawbacks against the benefits they offer in terms of cost and availability [21]. The decision to use SRMs or PM synchronous motors ultimately depends on a detailed analysis of the motor's torque-speed characteristics and its ability to meet the specific performance requirements of the competition.

This work focuses on the process of establishing and optimizing the torque-speed characteristics for the University of Pisa's FSAE racing team (Fig. 11). By analyzing real-world data from previous competitions, we have refined the motor selection process and designed a propulsion system that maximizes performance while adhering to budgetary and space constraints. The selection of torque-speed characteristics forms the basis for the motor dimensioning strategy, crucial for ensuring that the vehicle achieves the desired levels of acceleration, handling, and energy efficiency during the race. Additionally, addressing the complex interplay between motor performance, weight, and cost is key to achieving optimal designs for competitive motorsports.

In the following sections, we will discuss the methodology used to define these torque-speed characteristics, as well as the technical challenges involved in designing a motor that meets both the performance and economic requirements of FSAE racing. Focusing on this key aspect of motor design aims to contribute to the development of more efficient, sustainable, and competitive propulsion systems that can shape the future of electric racing.

Fig. 11. FSAE 2019 car of the University of Pisa (Italy) student team.

4.1.2 Background

The starting point of this work is the analysis of the tests that a FSAE car needs to perform during a race. These tests, named as “events” from now onward, can be classified as static and dynamic [74] and they will be described in the next subsection. Then, a series of technical constraints imposed by the race regulation will be also detailed.

A. FSAE static and dynamic events

There are three static events in a FSAE race. These are:

1) Engineering design: it consists of presenting the overall project of the car. The design choices and efforts are evaluated as well as their suitability to the market needs.
2) Business plan: it consists of evaluating a business case developed by the team assuming the feasibility of making the car a market product.
3) Cost analysis: it consists of evaluating the team's ability of accurately estimating production and design costs through a technical report and oral discussion.

Besides these static events, there are the following dynamic events:

1) Acceleration: the car has to speed up from zero speed on a 75 m long straight road featuring null slope.
2) Skid pad: this event evaluates the car performance during turning and takes place on a 15.25 m long 8-shape path that has to be covered twice in the minimum time possible.
3) Autocross: this is a demanding event consisting of running two laps on a relatively complex track.
4) Endurance and fuel economy: this is the final and the most important event of the whole competition. It aims to evaluate the whole racing performance of the car over 22 km on a circuit similar to the one used for the dynamic event 3). Energy consumption is also measured and assessed during the event.

B. Constraints

The car project has to meet a series of technical constraints imposed by the competition' rules. These are summarized as follows:

- The diameter of the wheels must be ≥203.2 mm.
- The maximum power P required from the battery must not exceed 80 kW.
- The maximum allowed DC-link voltage V_{DC} must not exceed 600 V.
- There are no limitations concerning the number and the type of electric motors.

Besides the above constraints which are imposed by the FSAE regulations, an economical constraint based on the team's available budget has to be also considered, i.e. the whole vehicle project must not exceed 20 k€.

4.1.3 Initial Design Considerations and Choices

In this section, the analysis of real data recorded during previous editions will be used to justify some initial design decisions, such as the number of motors and their location. In addition, the data are used to define the performance requirements and the motor topology.

A. Propulsion System Architecture

The first design choice refers to the propulsion system architecture. In a 4-wheels vehicle, configurations with 1, 2 or 4 motors can be implemented.

Having a 1-motor layout would minimize the electric motor complexity but would also compromise the optimal management of the available volume. In addition, this solution would lead to increase the weight of the mechanical transmission system as at least one differential gear would be needed. On the other hand, a 4-motors configuration would allow to use 1 motor per wheel, thus maximizing the propulsion capability exploiting the grip of all the four tires. In addition, it wound not require a mechanical differential gear. However, the overall architecture and control would be rather complex and costly, as the steering of the front axle wheels would need to be managed. Hence, recalling that a main design guideline here is the cost minimization, a 2-motors layout is deemed to be the most suitable solution for the case study at hand. In fact, this architecture consists of using 2 motors connected to the rear axle (non-steering) wheels, thus improving the space management compared to the 1-motor case, while also reducing costs and complexities associated to the 4-motors layout.

Regarding the transmission system, an in-wheel solution is disregarded for the sake of simplicity. In fact, although the need of the mechanical transmission would be removed, this solution would require an outer rotor configuration for the motors, that must be sized to match the torque and speed requirements of the wheels. In other words, to reduce the un-sprung masses and to ensure a certain degree of flexibility for the motors' location and design, a transmission system comprising a planetary gear is envisioned. This would permit designing the motors starting from reduced torque and increased speed values compared to the case where a direct coupling motor-wheel is considered. A reduced torque and higher speed demand permits decreasing the motors' weights and volumes. On the other hand, higher speed values result in an increased operating frequency, which in turn would lead to higher iron losses and AC ohmic losses within the conductors.

Therefore, considering the currently available semiconductor technologies and the cost constrains, the maximum allowed fundamental electric frequency is limited to 1 kHz.

Finally, considering the location of the electric components within the reference chassis (i.e. the car's chassis used in 2019 FSAE edition), the motors are positioned on the rear axle to increase the tires' grip, and as lateral as possible in the chassis to maximize the thermal exchange and leave space for the battery pack and inverters. Fig. 12 shows the components' location within the considered chassis.

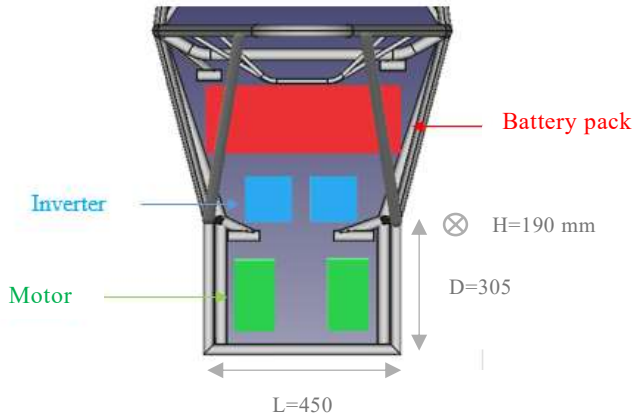

Fig. 12. Component's location in the chassis.

B. Performance requirements

One of the most important event for the definition of the performance requirements is the acceleration (see Section 4.1.2.A). Based on the car's performance during past editions, the target is to complete the test in ≈4 s. Assuming a uniformly accelerated motion, the predicted acceleration a for a distance d = 75 m starting from zero speed is calculated as in (1).

$$a = \frac{2\,d}{t^2} \simeq 9.3\ \frac{m}{s^2} \tag{1}$$

Considering that the total mass of the vehicle is M ≃ 300 kg, the necessary force to propel the vehicle is calculated as in (2). Under the assumption that 65% of the total vehicle mass is distributed on the rear axle, the necessary fractional coefficient μ can be determined as in (3), where g is the gravity acceleration. The

obtained value for μ is 1.46, which fits the typical values for race tyres. Using 13-inch rims with a tyre's diameter D of ≃445 mm, the maximum transferable torque without considering the dynamic axle load shifting is determined as in (4).

$$F = a\,M \simeq 2800\ \text{N} \tag{2}$$

$$\mu = \frac{F}{0.65\,M\,g} \simeq 1.46 \tag{3}$$

$$T = \frac{F\,D}{2} \simeq 600\ \text{Nm} \tag{4}$$

Contrarily, taking into account the dynamic axle load shifting, the maximum transferable torque in dynamic condition is $T_{MAX} \simeq 760$ Nm, i.e. during the acceleration the rear axle load increases ensuring more grip. A difference of around 20% of the transferable torque is therefore detected compared to the value found in (4). To investigate whether an increase of the available torque up to 760 Nm can play a significant role in reducing the time for completing the acceleration event, simulations are carried out in Matlab, considering the variability of the tyres' grip with respect to the speed. The drag and lift coefficients used are 0.6 and 0.443 (low drag configuration), respectively. In Fig. 13, the results show that the running time reduction amounts to 0.3 s (from 4.3 s to 4 s) when passing from 600 Nm to 760 Nm. Analysing the previous year's results for the acceleration event, the achieved time reduction is deemed to be not sufficient to justify an increase of torque in a logic of optimization.

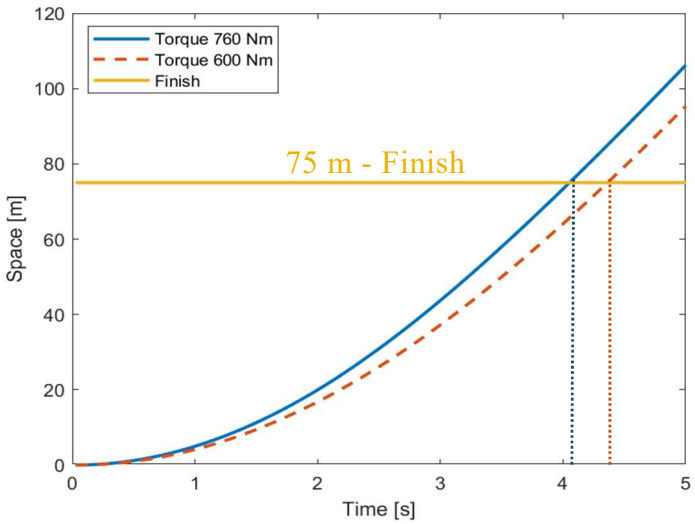

Fig. 13. Acceleration tests – Execution time comparison between 760 Nm (blu) and 600 Nm (orange) of available torque to the wheels.

Considering that a top speed of 130 km/h could be sufficient for this context, according to the latter result (T=600 Nm, i.e. 300 Nm for each motor) in combination with the frequency (1 kHz) and space (see Fig. 12) constraints, a (gear) reduction ratio k_r=10 is selected. In fact, the maximum operating frequency turns out lower than 800 Hz and the motors' dimensions, whose calculations have been carried out leveraging on the Lorenz's force hypothesis, are L≃90 mm and D=H≃180 mm. Those values are perfectly compatible with the available space. Therefore, considering the two wheel-drive and the selected reduction ratio, each motor will be sized for a torque of 30 Nm.

A number of statistical analysis of the motor torque-speed operating points during a real endurance test have been performed aiming to select the most suitable motor technology and characteristics. The most relevant results of the analysis are summarised and reported in Fig. 14Fig. 15 and Fig. 16.

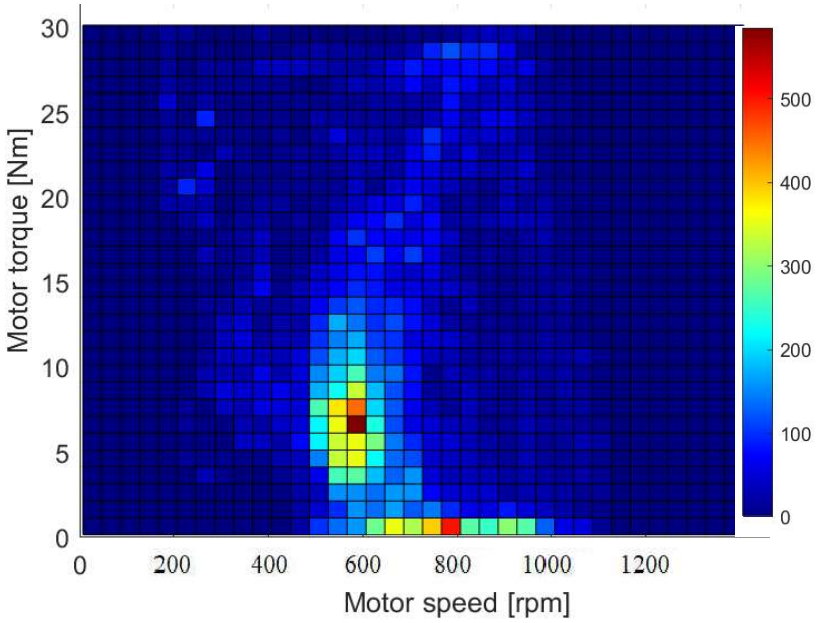

Fig. 14. Motor torque-speed usage during an endurance event. The red cells indicate a high use in that specific torque-speed condition.

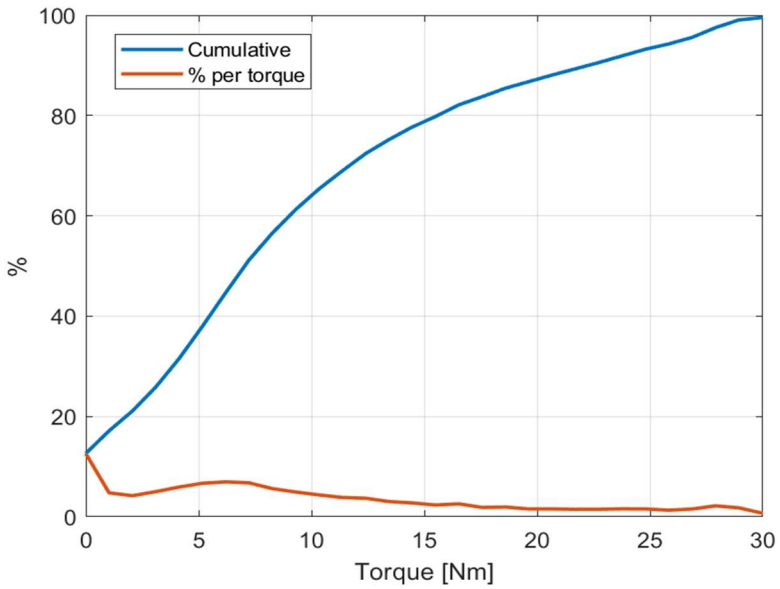

Fig. 15. Motor torque usage distribution. Percentage of usage during the endurance event (orange) and cumulative of the orange curve (blue).

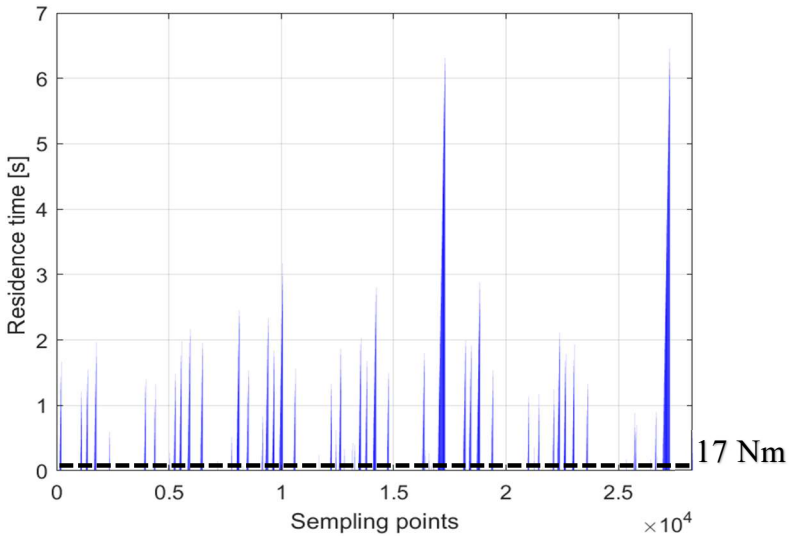

Fig. 16. The consecutive residence time of torque demands higher than 17 *Nm* during the endurance test.

These studies reveal a reduced power usage compared to the maximum available power of 80 kW. In fact, from Fig. 14, it can be noticed that the average torque requests do not exceed 10 Nm and the average speed is lower than 800 rpm. In Fig. 15, the orange curve reports the % usage of each torque values ranging from 0 Nm to 30 Nm, while the blue curve is the cumulative of the orange one. The former trend confirms that 30 Nm is an appropriate value for the motors' sizing, whereas the latter informs on that the torque is lower than 17 Nm for more than 80 % of the time. In addition, analysing the residence time of the torque demands higher than 17 Nm (Fig. 16), it can be noticed that these reach peaks of 6 s consecutive.

C. Motor selection

Having identified the propulsion system architecture and having defined some initial performance requirements, the next step consists of investigating the torque-speed characteristic in order to select the motor typology. Hence, first the base speed n_b is determined as in (5), resulting in ≈12730 rpm.

$$n_b = \frac{60}{2 \cdot \pi} \frac{\mathrm{P} \cdot k_r}{\mathrm{T}} \tag{5}$$

Considering that the maximum car speed is 130 km/h (corresponding to ≃16000 rpm), the torque-speed characteristic features a reduced flux weakening area as observed in Fig. 17. Therefore, a surface mounted PM topology would seem to be the most suitable solution for this application, also recalling that the main design guideline here is the available budget. In fact, surface mounted PM motors have lower production costs in a customized case, compared to interior PM or SR machine layouts. A summary of the selected characteristics at this stage are listed in Table VII.

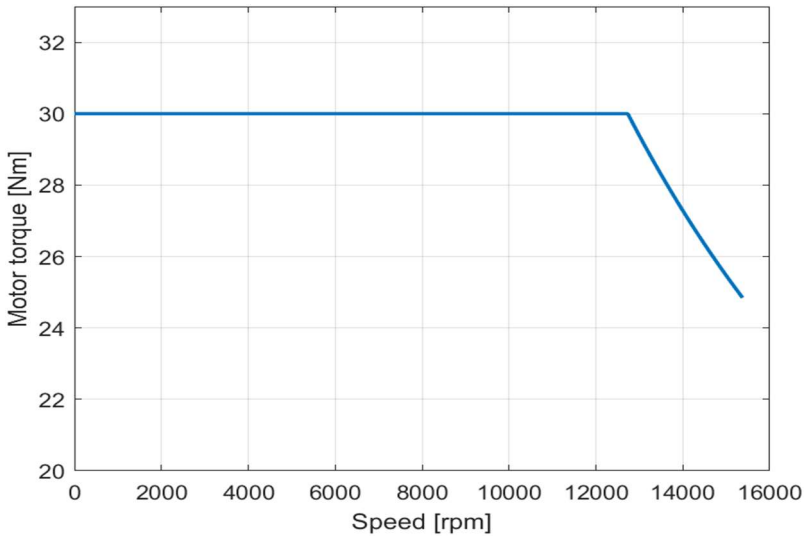

Fig. 17. Motor torque-speed characteristic.

Table VII
INITIAL DESIGN CHOICES

Number of motors	2
Motor topology	Surface mounted PM
Motor's location	Rear axle
Maximum torque to wheels	600 Nm
Reduction ratio	10

Motor torque	30 Nm
Base speed	12730 rpm

4.1.4 Motor Design

Having identified the performance requirements from the analysis of data available in past competitions, it becomes possible to perform a preliminary design of the selected PM motor. The results are subsequently validated via a FE model, which is also used for the design refinement.

A. Preliminary Design

The starting point of the preliminary design is based on the assumption that the stator conductors are directly located in the main air gap, distributed on the inner stator profile in the form of a continuous current sheet. Therefore, the generated torque T_E can be determined as in (6), i.e. applying the Lorentz Force acting on the conductors which are invested by the air gap flux density B. In (6), γ is the parameter mapping the stator geometrical profile, t is the time variable, I_L is the linear current density, l is the active axial length of the machine and r is the mean air gap radius. Assuming a sinusoidal distribution of both $B(\gamma,t)$ and $I_L(\gamma,t)$ and imposing their alignment, the electromagnetic torque is obtained by means of the integral (6) that can be easily solved as in (7), where B_m and I_{Lm} are the amplitudes of $B(\gamma,t)$ and $I_L(\gamma,t)$, respectively.

$$T_E(t)= \int_0^{2\pi} B(\gamma,t)\cdot l \cdot I_L(\gamma,t) \cdot r^2 \cdot d\gamma \tag{6}$$

$$T_E = \pi\, l\, r^2\, B_m\, I_{L_m} \tag{7}$$

The I_{Lm} value is chosen equal to 70 kA/m for the preliminary calculations. The maximum linear current density directly correlates to the conductors' current density, the slot dimensions, the slot fill factor, and the cooling technology envisioned. However, this parameter is mainly limited by the heat removal capability. Assuming for the machine at hand a natural convection cooling system (favoured by the vehicle motion), the RMS current density J_{RMS} is chosen equal to 7 A/mm^2 in continuous operation. Nevertheless, based on the analysis on Fig. 14,Fig. 15 and Fig. 16, this current density value is used for a torque demand of 17 Nm, whereas 30 Nm are assumed to be reached at overload conditions using a

current density J_{RMS_ol}= 13 A/mm^2. This allows to reduce the machine size compared to a design tailored against the peak torque.

The second relevant parameter involved in (6) is B_m, that strictly depends on the characteristic of the soft ferromagnetic materials employed for the stator and rotor cores and of the hard magnetic materials (i.e. PMs). Common Fe-Si "M330-35A" laminations are used for the cores. Medium-quality NdFeB "N28AH" PMs with coercive field H_C at 20°C equal to ≈830 kA/m is selected to guarantee a good performance while keeping the overall costs within the relevant constraint. Therefore, B_m is chosen equal to 0.85 T.

Having selected the initial values for B_m and I_{Lm}, it becomes possible to calculate the rotor volume $\pi \cdot l \cdot r^2$. The ratio r/l is chosen according to the chassis dimensional constraints shown in Fig. 12. The number of pole pairs p is chosen equal to 3 taking into account the frequency limit discussed in Section 4.1.2.A, i.e. <1 kHz. The air gap thickness is preliminary hypothesized equal to 1 mm and the magnet thickness is then determined considering a no-load scenario (i.e. the magneto motive force due to the armature reaction is neglected) and a linear behaviour of the ferromagnetic materials (i.e. the magneto-motive force drops due to the iron parts are neglected). The magnet span is chosen to be 88% of the pole pitch. Regarding the winding design, a full pitch, single-layer layout with a number of slots/pole/phase q=1 is initially assumed. Considering a fill factor equal to 0.6, the current I flowing in the conductors and, subsequently, the number of turns in series per phase can be estimated using (8). The tooth width and the yoke thickness can be finally estimated using the classical relevant sizing formulas [28], imposing 1.6 T in the teeth and 1.4 T in the yoke. A summary of the initial motor design parameters are shown in Table II.

$$N = \frac{I_m \pi r}{3 p I} \tag{8}$$

Table VIII
MOTOR DESIGN PARAMETERS

Magnetic loading	**Electric loading**	**Peak current density**	**Continuous current density**	**Slot fill factor**
0.85 T	70 kA/m	13 A/mm^2	7 A/mm^2	0.6

Magnetic loading	Electric loading	Peak current density	Continuous current density	Slot fill factor
Peak current	**Pole pairs**	**Air gap thickness**	**Rotor radius**	**Active length**
140 A	3	1 mm	45 mm	63 mm
Number of slots	**Magnet thickness**	**Outer diameter**	**Tooth thickness**	**Yoke thickness**
18	4 mm	170 mm	10 mm	14 mm

Once the preliminary design is completed, the obtained geometry is imported in a FE analysis tool for validation and refinement purposes.

B. FE model validation of the preliminary design

A FE model of the surface mounted PM machine designed via the sizing equations reported above is implemented using Flux software. The resulting geometry and details are shown in Fig. 18. A single pole pitch angular span is modelled leveraging on the odd symmetry characterizing the machine.

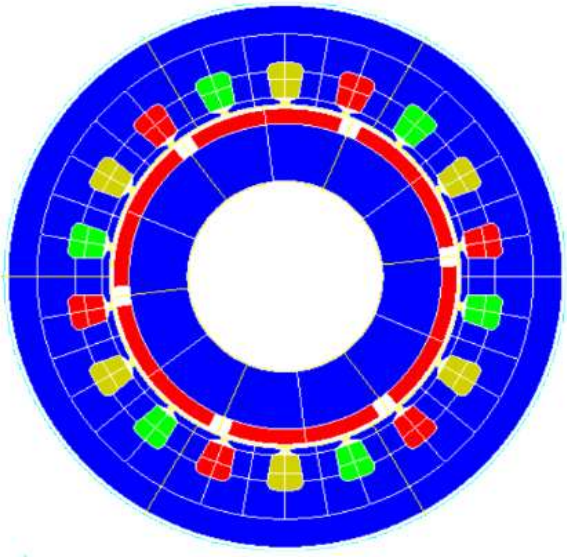

Fig. 18. Preliminary motor design.

At first, a no-load analysis is carried out to validate the analytical sizing tool. The no-load line-to-line three-phase voltages are given in Fig. 19, showing a peak limit of ≈ 330 V, thus complying with the DC-link voltage constraint of 600 V. The field map and flux lines distribution are provided in Fig. 20, where it can be observed how the flux density values in the air gap (0.85 T), in the teeth (1.3 T), and in the

yoke (1.2 T) are close to those assumed in the analytical model, with a maximum error of 8%. For the sake of completeness, the cogging torque is also shown in Fig. 21.

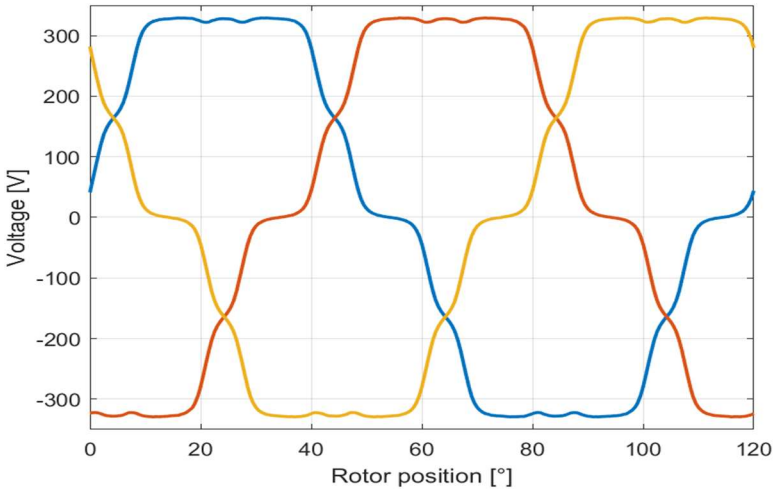

Fig. 19. No-load line-to-line three-phase voltages.

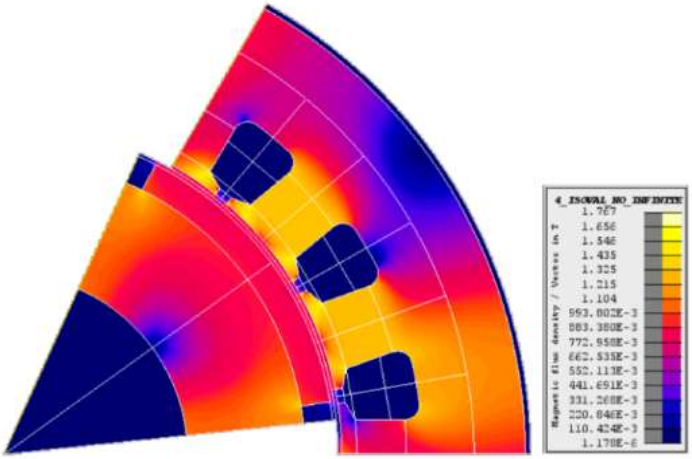

Fig. 20. No-load field map.

At full-load conditions, achieved by feeding the three armature winding with a set of three-phase sinusoidal currents having the amplitude I (see Table VIII), the current density obtained is 11 A/mm^2, with an error of 15% compared to the analytical assumption due to the preliminary consideration of rectangular slots. Finally, the torque is shown in Fig. 22, showing a ≈1% understimation of the FE result compared to the value assumed in the analytical tool.

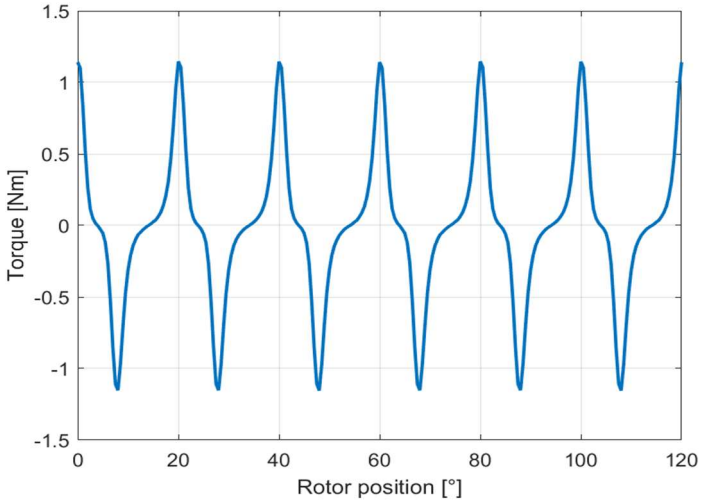

Fig. 21. Cogging torque.

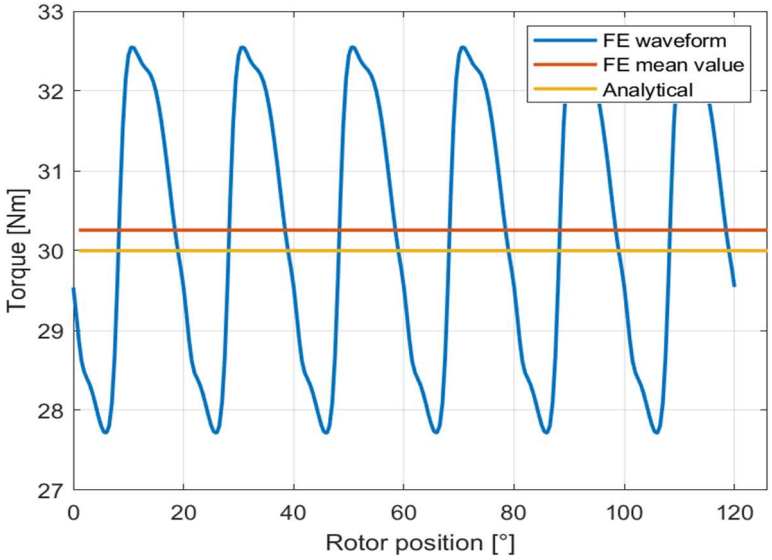

Fig. 22. Torque developed by the motor evaluated via FE simulations (in blue) and its average value (in red). In yellow, the torque value assumed in the preliminary analytical sizing.

All these results prove the validity of the analytical model as a preliminary design tool for the electrical machine under investigation. However, it is clear that there is room for refining the design of the PM machine, e.g. improving the quality of the voltage waveforms, reducing the cogging torque and the full-load torque ripple, etc. To do so, the winding distribution is modified from a full pitch single-layer layout to a short pitch (by one slot) double-layer one, doubling the number of slots/pole/phase. The relevant results are shown in the next section.

4.1.5 Design Refinement and Results

The modified design parameters of the PM motor equipping the double-layer winding are summarized in Table IX, where also the final weight of the active parts is highlighted for completeness.

Table IX
FINAL MOTOR CHARACTERISTICS

Active length	**External diameter**	**Tooth thickness**	**Yoke thickness**	**Weight**
65 mm	165 mm	5 mm	13 mm	≃ 20 kg

The no-load analysis at base speed of the modified version of the motor leads to the field map reported in Fig. 23 and to the line-to-line phase back-EMF waveforms shown in Fig. 24. The amplitude harmonic spectrum of the latter quantities is compared in Fig. 25 with that of the line-to-line phase voltages reported in Fig. 19 for the unrefined motor version. Fig. 25, for clarity, the fundamental harmonics are not reported, although a 2% decrease is registered for the refined design. It can be noticed that the waveform quality improvement is significant and can be mainly imputed to the mitigation of the 5^{th} , $7^{th,}$, 17^{th} and 19^{th} harmonics. The second relevant result deriving from the no-load analysis is shown in Fig. 26, which reports in red the cogging torque for the refined motor and, for the sake of comparison, the cogging torque for the preliminary version of the motor in blue.

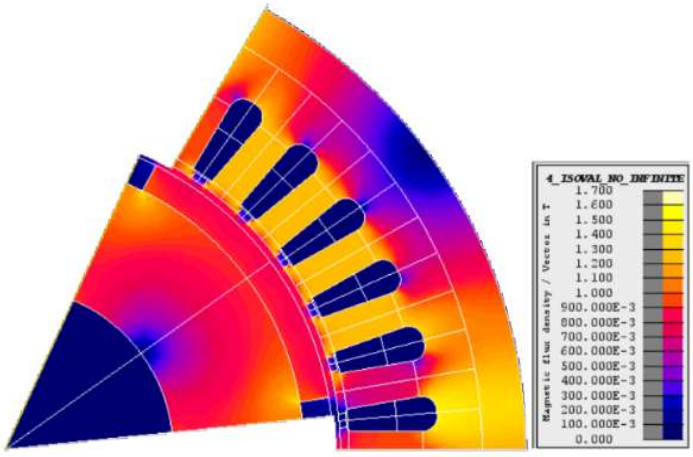

Fig. 23. Final motor design - No-load field map.

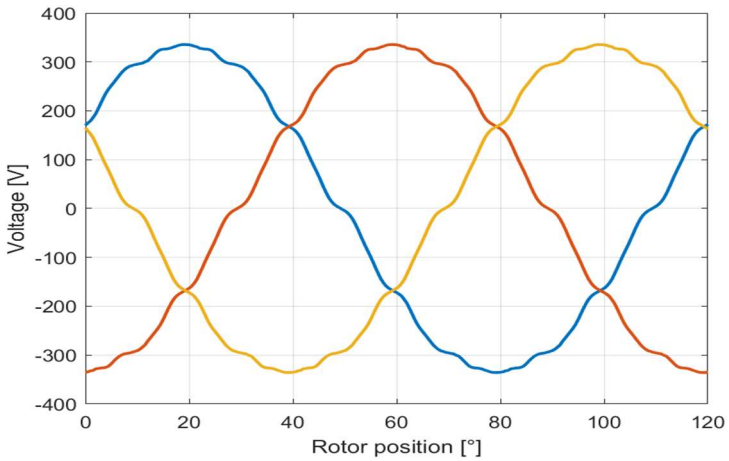

Fig. 24. No-load line-to-line back-EMF waveforms in the refined motor.

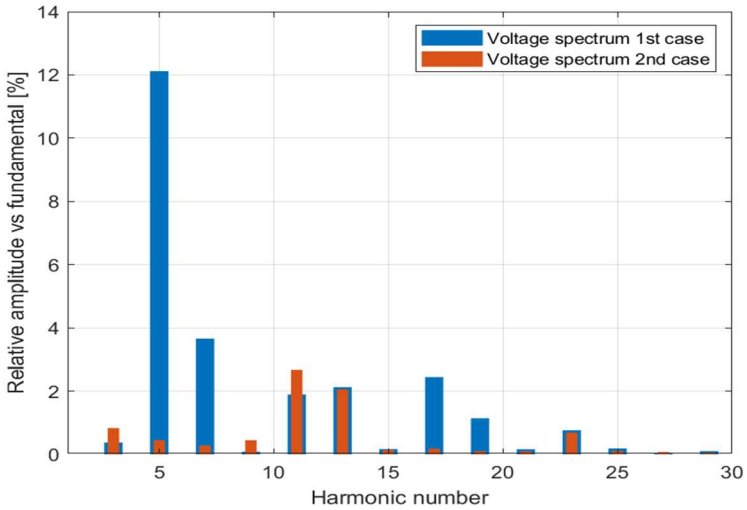

Fig. 25. Comparison in terms of voltage harmonic spectrum between the preliminary versions against the refined version of the PM motor.

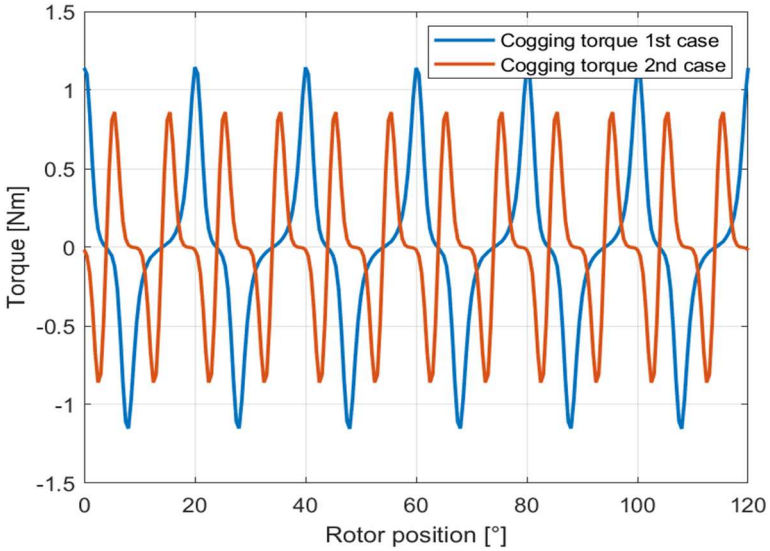

Fig. 26. Cogging torque comparison between 1st and 2nd case.

The electromagnetic torque developed at base speed by the refined motor is reported in Fig. 27 in red. The average torque is ≈30 Nm, thus meeting the specifications. In Fig. 27 the torque waveform is compared to that developed by the preliminary version of the motor, showing a higher average value and a significant torque ripple reduction. As a result of the on-load analysis at base speed, the line-to-line three-phase voltages are also reported below in Fig. 28. The peak value is 355 V, thus meeting the DC-link voltage constraint.

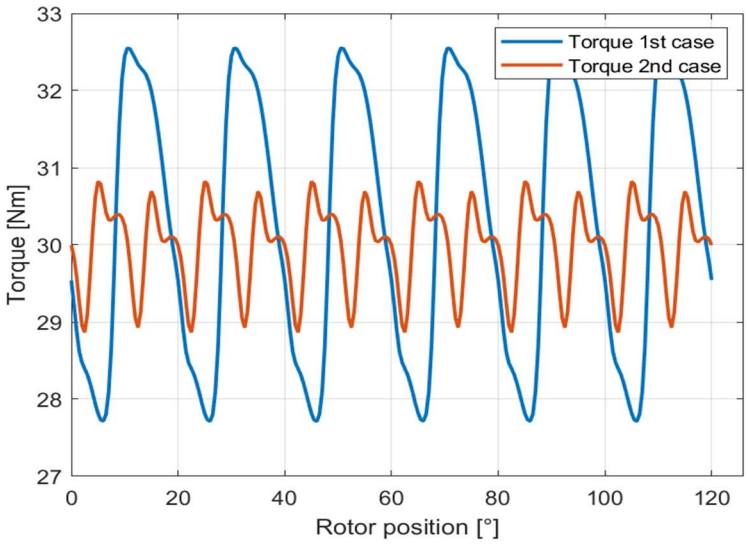

Fig. 27. Comparison between the torque developed by the refined motor (in red, namely "Torque 2nd case") and that developed by the first version of the motor (in blue, namely "Torque 1st case").

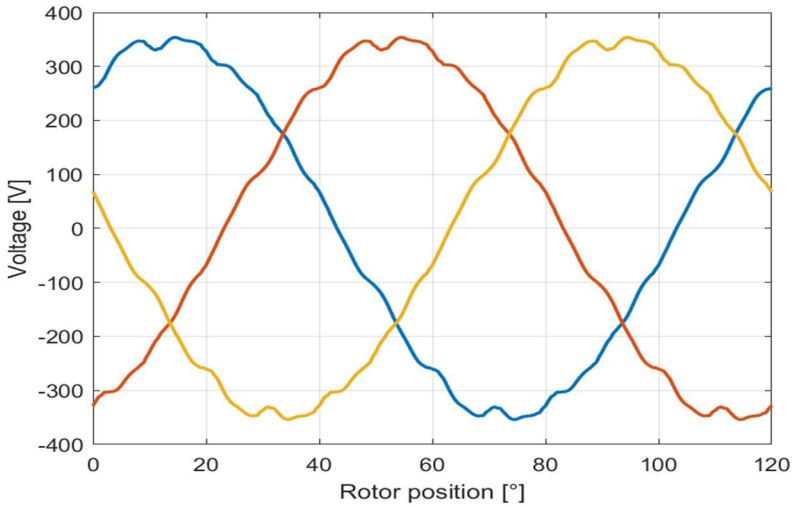

Fig. 28. On-load line-to-line phase voltages of the refined version of the motor at base speed.

4.1.6 Conclusions

The design process of a propulsion system for FSAE cars is presented in this chapter, with special focus on the design of the propulsion motor. The selection of

the system architecture, i.e. a 2-motors layout implemented onto the rear non-steering axle, was mainly based upon budget considerations. Additional constraints, such as the overall dimensions of the chassis and those imposed by the race regulations have been accounted in the definition of the performance requirements in terms of torque and speed which have been based on the analysis of data available from previous editions. In this context, a suitable torque-speed characteristic was envisioned, allowing to select the common SPM motor layout as the most suitable for this application.

The motor design was performed leveraging on the classical sizing equations first. The relevant findings were validated against a purposely built FE model, showing a good similarity. Besides the validation, the FE analysis highlighted some room for improvements in the machine design, especially in the armature winding layout. Therefore, a design refinement was carried out and, as a result, all the technical and economic constraints and performance requirements were met, i.e. a low cost, 20 kg motor achieving 30 Nm up to the base speed of 12730 rpm.

4.2 Multi-Physics and Multi-Objective Optimization of a Permanent Magnet-assisted Synchronous Reluctance Machine for Traction Applications.

4.2.1 Introduction

In the context of sustainability, PMaSynRMs are commonly used in traction applications due to their ability to combine the advantages of reluctance and PM motors. However, these machines typically suffer from limitations such as low torque density, torque ripple, and power factor issues. To address these challenges, several automotive manufacturers have adopted multi-layer IPM designs that incorporate RE PMs to enhance performance.

This study focuses on the analysis of a PMaSynRM for traction applications, integrating both electromagnetic and structural aspects. The goal is to provide a comprehensive approach to setting up FE models for both fields, addressing a gap in the literature where detailed structural analyses of such machines are often lacking.

FEA is a powerful numerical tool that enables the study of multi-physics problems, although electromagnetic and structural fields are often examined separately. For

instance, Barcaro et al. focused exclusively on structural aspects, analysing an IPM rotor under static and fatigue loads. They emphasized the importance of the bridge design, identifying stress concentrations caused by sharp slots where magnets are placed [56].

In the realm of electromagnetic optimization, various researchers, such as Gangl, Zhu, Huang, and Dai, have employed optimization techniques aimed at improving the performance of PM motors [57]-[60]. These studies have focused on maximizing output torque, minimizing torque ripple, and reducing the cost of PMs through hybrid configurations. Structural optimization, however, remains less explored, with many studies emphasizing only the rotor design from a structural perspective [61].

The design of IPM rotors presents significant challenges when both electromagnetic and structural goals must be met. Bridges connecting the magnetic islands in the rotor must saturate magnetically, but also maintain sufficient mechanical strength to avoid failure under operational stress. The trade-off between minimizing bridge size for electromagnetic efficiency and ensuring structural robustness underscores the need for a multi-physics optimization approach [62]-[65].

Al-Ani et al. proposed a multi-physics rotor design, but omitted key details regarding the optimization algorithm. Their approach led to an improved structural design, but with a 10% reduction in torque at 5000 rpm compared to the original layout [66]. In contrast, more recent studies by Di Nardo et al. and Lin et al. employed comprehensive multi-physics optimization algorithms to iteratively improve both electromagnetic and structural properties [67]-[69]. These approaches highlight the importance of simultaneous optimization to avoid suboptimal solutions.

In this contribution, a multi-physics, multi-objective optimization methodology is proposed to address both electromagnetic and structural concerns in the rotor design of PMaSynRMs. The objective functions include maximizing mean output torque, minimizing torque ripple, and reducing mechanical stress, while constraints ensure that both electromagnetic performance and structural integrity are maintained. Additionally, a thermal analysis is conducted to ensure that the operating temperatures do not exceed critical thresholds, avoiding magnet demagnetization.

This work introduces detailed FE structural modeling into the optimization process, which is often simplified or overlooked in the existing literature. Here, attention is given to critical details such as the contact problem between magnets and rotor, stress concentrations, and mesh convergence, providing a more accurate and reliable design solution [70][71].

4.2.2 Materials and Methods

In this section, the geometrical and electrical machine parameters are presented. Then, the numerical analysis set-up is described: at first, the electromagnetic model and, subsequently, the structural one. The simulation approaches are described separately for each field to highlight the adopted assumptions and the expected outcomes.

The sub-sections 4.2.6 and 4.2.7 aim at explaining the methodology employed to find the optimal design of the rotor. In detail, in the first one the design variables of the optimization are selected among the numerous geometric features of the rotor. In the second one, the adopted optimization algorithm and the models are explained.

4.2.3 Original Machine Configuration

An existing PMaSynRM with 8 poles, previously designed for a traction application, is investigated. Fig. 29(a) shows one pole pitch of the rotor and of the stator. The rotor stack is characterized by three flux barriers equipped with brick-type PMs, whereas the stator consists of a short pitch double layer winding. The entire stator comprises 72 slots hosting a three-phase winding, with 3 slots-per-pole-per-phase. Fig. 29(b) shows the global view of the rotor, whose overall length is 155 mm. Table X summarizes the parameters of the initial motor configuration and its material properties. The considered motor operates at the base speed of 5000 rpm and its maximum speed is 15000 rpm, similarly to [66]. The magnets are in N38-UH, whereas the rotor is manufactured of high-performance steel called JNEX 10-900. This steel combines valuable electromagnetic and structural properties. The strength of the JNEX 10-900 is reported since it will be used to evaluate the stress within the rotor.

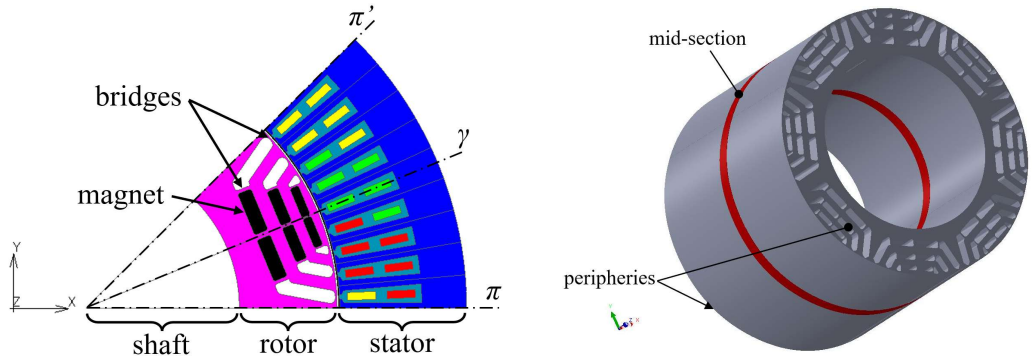

(a) (b)

Fig. 29. (a) A pole pitch of the machine. (b) Global view of the rotor.

Table X

ELECTRICAL AND GEOMETRICAL REFERENCE MACHINE PARAMETERS

Electrical parameters	
Winding type	Short pitch double layer
Slot number	72
Phase number	3
Turn per coil/pole/phase	42
Number of barriers	3
Number of magnets per pole	6
Operating speed	5000 rpm
Maximum speed	15000 rpm
Rated power	233 kW
Rated voltage bus DC	620 V
Geometrical parameters	
Inner diameter of the rotor	124 mm
Outer diameter of the rotor	190 mm
Outer diameter of the stator	288 mm
Angular pole pitch	45°
Air gap thickness	1 mm
Thickness per layer	0.2 mm
Overall length	155 mm
Material properties of the rotor and stator: JNEX 10-900	
Density	7490 kg/m^3
Young's Modulus	200000 MPa
Poisson's ratio	0.33

Yield tensile strength	570 MPa
Ultimate tensile strength	740 MPa
Elongation at break	16.3 %
Material properties of the magnets: N38-UH	
Density	7650 kg/m^3
Young's Modulus	158000 MPa
Poisson's ratio	0.24

4.2.4 Electromagnetic Finite Element Analysis

The electromagnetic model is implemented in the FE-based software Altair Flux. Exploiting the geometrical and winding symmetries characterizing this machine, one pole pitch, which has an angular extent of 45°, is modelled to reduce the computation burden. Odd symmetric boundary conditions are employed at the planes π and π' to contain the number of nodes. This assumption will be useful since combined electromagnetic-structural optimizations will be carried out.

Fig. 30(a) shows the second-order planar mesh where finer elements (0.2 mm) were employed at the air gap, PMs and the flux barrier regions, whereas a coarser mesh (8 mm) is adopted at the shaft and at the outer radius of the stator.

The stator winding is mimicked by the electric circuit shown in Fig. 30(b). A star-connected three-phase winding is supplied by a three-phase set of sinusoidal currents, realized through two current sources. Only two current sources are used in the circuital representation as the system would be over-determined if a third current source was adopted. The model ignores the end-winding effects as a first approximation, aiming at reducing the computational times of the optimization process. To the same purpose, as well as to make a fair comparison against the benchmark machine, the stator and the main airgap are not modified during the optimization, while the rotor geometric variables are investigated as means to achieve the optimization objectives. The electromagnetic analyses and results of the benchmark motor shown in Fig. 30 will be reported in the sub-sections.

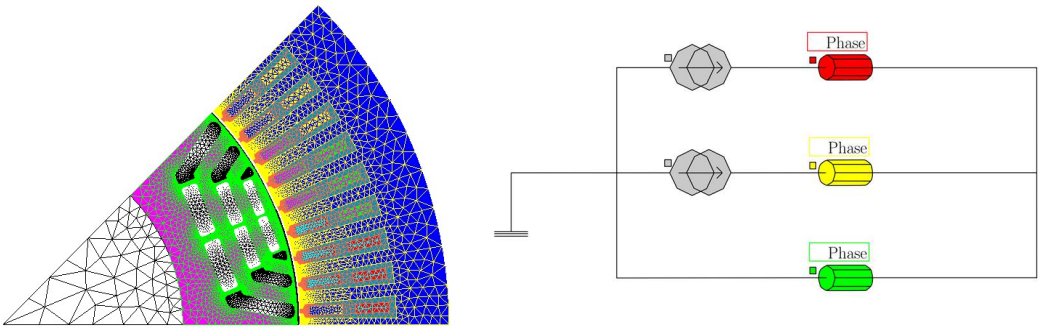

(a) (b)

Fig. 30. (a) The mesh used in the electromagnetic model. (b) The electrical circuit coupled to the FE model.

4.2.5 Structural Finite Element Analysis

Non-linear FE analysis is performed for determining the stress field of the rotor. The stress should remain below a determined value not to jeopardize its structural integrity.

The non-linearities are due to the contact problem between PMs and rotor slots, or if local plastic strains of the rotor occur.

The model considers only 1/16 of the entire rotor identified by the planes γ and π, since symmetry boundary conditions are applied to the abovementioned planes, see Fig. 29(a).

Assuming that the stress and the strain of each layer are not influenced by its axial location, a plane FE model is implemented instead of a three-dimensional one. Among the hypotheses needed for this simplification, it is mandatory to identify an axial direction and a cross-section orthogonal to this axis. In particular, each cross-section exhibits the same geometry and the same loading condition. In our application, the axial direction coincides with the axis of the rotor, while the cross-section is identified by the angular sector of the lamination, see Fig. 29(a).

Furthermore, the structural behaviour of the laminations is included between two edge cases. The first case is identified by the laminations at the middle of the axial extent of the motor, while the further case is identified by the laminations located at the motor axial periphery, see Fig. 29(b). In particular, the first case is addressed by the plane strain hypothesis, whereas the second case complies with the plane stress one.

The plane strain model is adopted when no out-of-plane strain is allowed; this condition occurs at the middle axis of the rotor. On the other hand, the plane stress model is adopted when the out-of-plane stress is null; so, this is the case of the laminations at the periphery of the rotor. In fact, only one side of the layer is lapped

by the air, thus no axial stress is generated. In fact, the laminations are stacked together limiting the out-of-plane strain. A critical discussion of plane assumptions is reported in [72][73]. As a consequence, the more actual and conservative plane condition should be identified and then considered for the following steps. The equivalent von Mises stress contour plots are anticipated to justify the modelling strategy, see Fig. 31. No significant differences were found between the two models; the maximum of stress is located at the fillet radius of the innermost lateral bridge.

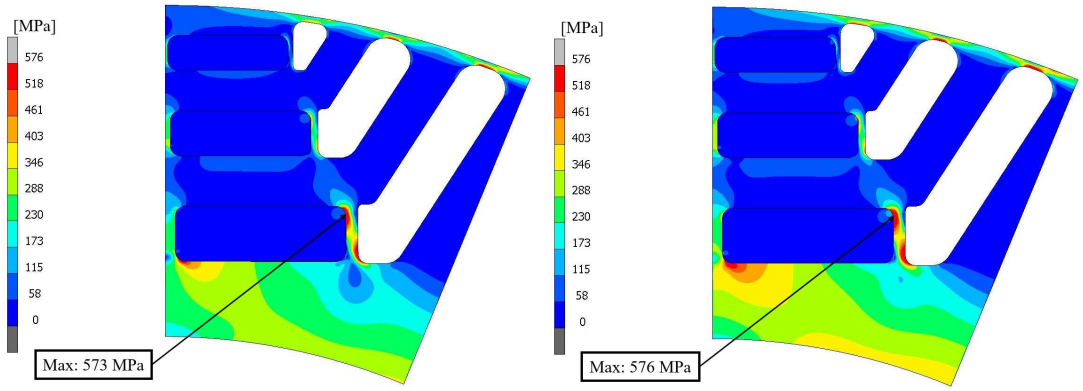

(a) (b)

Fig. 31. Equivalent von Mises stress contour plot: (a) plane strain modelling; (b) plane stress modelling.

The rotor is connected to the shaft employing a threaded ring nut; thus its laminations are compressed, therefore, the plane strain model has better grasped the rotor stress field.

The FE mesh adopted for the plane modelling includes both the rotor and the magnets and it is built using the commercial software Altair Hypermesh. 82.507 QUAD4 quadrilateral elements (four-node, four Gaussian integration points, isoparametric, bilinear element formulated for plane strain assumption) are used.

Five element sizes are employed to assess the numerical convergence of stress and the results are reported in Fig. 32(a), where the maximum equivalent von Mises stress is registered as a function of the mesh size. The mesh size of 0.1 mm is employed to obtain at least 8 elements for the smallest fillet to properly grasp notch effects. By way of example, Fig. 32(b) shows a detailed view of the most stressed fillet of the rotor, while the global view is Fig. 31(a).

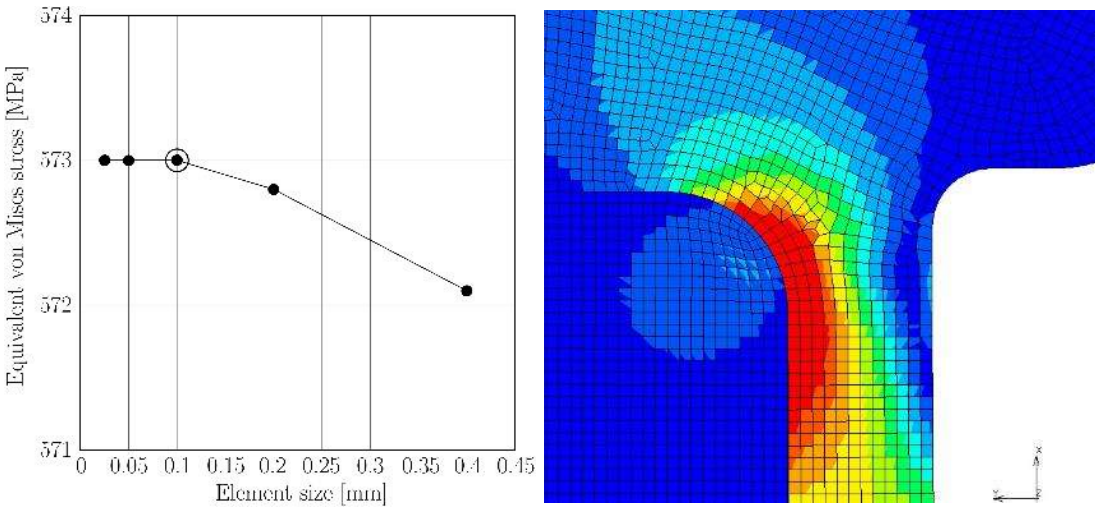

(a) (b)

Fig. 32. (a) Convergence stress results; (b) detail view of the equivalent von Mises stress contour plot.

Differently from us, Barcaro et al. [56] analysed an IPM rotor adopting a coarser mesh omitting the convergence study; only 4 elements are employed for the discretization of the smallest fillet. Therefore, the simulations of Barcaro et al. [56] were remarkably speeded up, but the precision of the resulting stress contour plot might be partially compromised.

A linear elastic stress-strain law is employed for the magnets in N38-UH; whereas, an elastoplastic law with linear hardening is implemented for the rotor material in JNEX 10-900. Fig. 33 shows the true stress-true strain curve of JNEX 10-900 retrieved from [71].

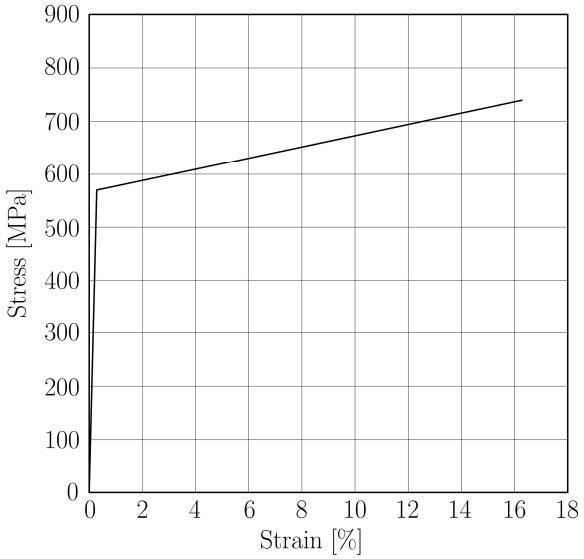

Fig. 33. Stress-strain curve of JNEX 10-900.

The authors accept localized plastic strains of the rotor only; however, these regions need to be small and limited in number. The plasticity is ascribable to the fact that the magnets seat at the rotor slot at the initial start-up of the motor. This phenomenon is well-known as the elastic shakedown effect. The adoption of the elastoplastic law pushes the rotor design to the limits. Conversely, Al-Ani et al. [66] constrained the rotor design into the elastic region using a too conservative approach.

The operating conditions of the motor are mimicked. The FE simulations are solved by the commercial software MSC MarcMentat, which properly manages the contact problem using the non-linear node-to-segment contact algorithm. The contact interaction between the rotor and the magnets is modelled by a frictional and unilateral contact. A friction coefficient of 0.4 is set.

Three boundary conditions have to be considered for the rotor simulation: the centrifugal load due to its revving speed, the symmetry condition due to considering only 1/16 of the rotor, and the assembly between the rotor and the shaft.

First, the centrifugal load is applied to all the elements of the model considering the maximum revving speed of 15000 rpm, the mass of each element, and the distance of each element from the rotation axis. As a result of this, an equivalent field of forces is properly assigned to the whole mesh.

Then, the symmetry condition is applied to the nodes lying on γ and π planes, see Fig. 29(a). These boundary conditions have constrained the displacements normal to the symmetry planes, thus all the rigid body motions of the plane model are removed.

Lastly, the influence of the connection between the shaft and the rotor deserves a detailed discussion. Two assembly strategies are commonly used to transfer the torque from the rotor to the shaft and vice versa: by interference fit or by adopting a prismatic coupling, see Fig. 34.

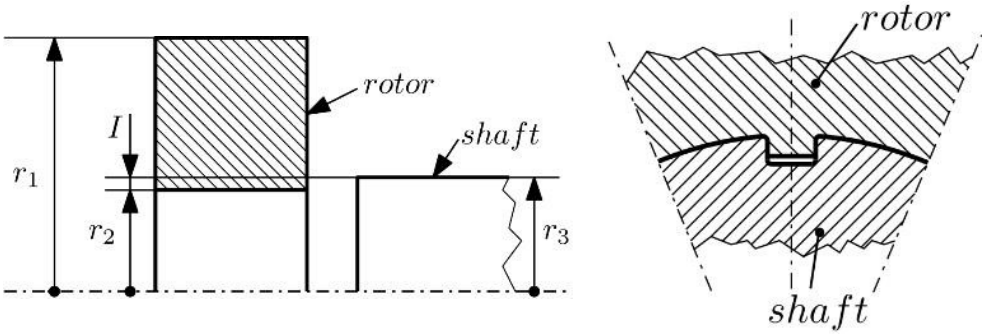

(a) (b)

Fig. 34. Shaft-rotor assembly: (a) interference fit, lateral view; (b) prismatic coupling, frontal view.

The first solution is the easiest from a design point of view. The range of tolerances on the fitted members needs to be evaluated so that a minimum interference allowance provides a sufficiently tight assembly, whereas the maximum interference will not induce excessive stress.

In particular, this coupling should withstand high torque, which could promote the relative motion of the rotor and shaft thus jeopardizing the motor working. Moreover, the centrifugal force hinders the interference fit, facilitating the detachment between the mating components. The interference fit is fully constraining the displacement of the nodes laying on the inner diameter of the rotor.

If the inference fit was adopted, a high radial interference (I) of at least 0.21 mm has to be used since the present motor transmits high torque ($\geq$ 435 Nm) at a high revving speed (15000 rpm). Fig. 35 shows the stress on the rotor due to the application of the sole interference, the maximum von Mises Stress is 580 MPa and exceeds the yield stress of the JNEX 10-900. A wide region at the rotor inner radius and many bridges achieves the plastic field, so this strategy is believed to be unsafe, and it will probably induce the rotor collapse.

Moving to the prismatic coupling assembly, it allows the radial displacement of the rotor, since a tight clearance between the rotor and the shaft is designed, see Fig. 34(a). Therefore, no stress in the rotor is induced during the motor assembly, thus no boundary conditions at the rotor inner radius are applied.

The model set-up presented here can be also used to investigate the high cycle fatigue strength of the rotor. The fatigue cycle is repeated, thus the yield strength coincides with the repeated fatigue limit.

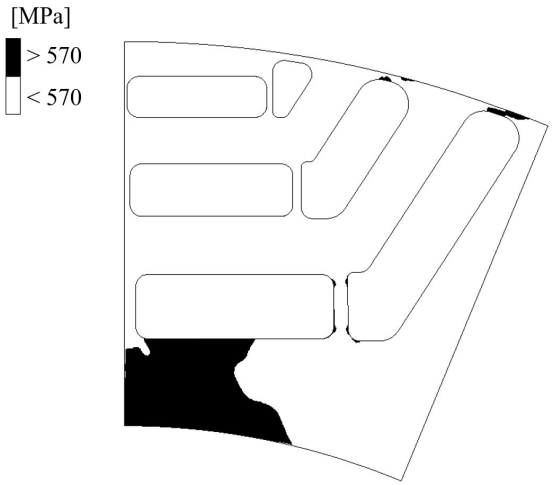

Fig. 35. Von Mises contour plot of the rotor under the effect of the sole interference.

4.2.6 Parametric Analysis of the Rotor Geometry

The geometry of the rotor is described by many geometric parameters, where the nomenclature is shown in Fig. 36. Note that the design parameters are referred to each magnet layer using the subscript *i*.

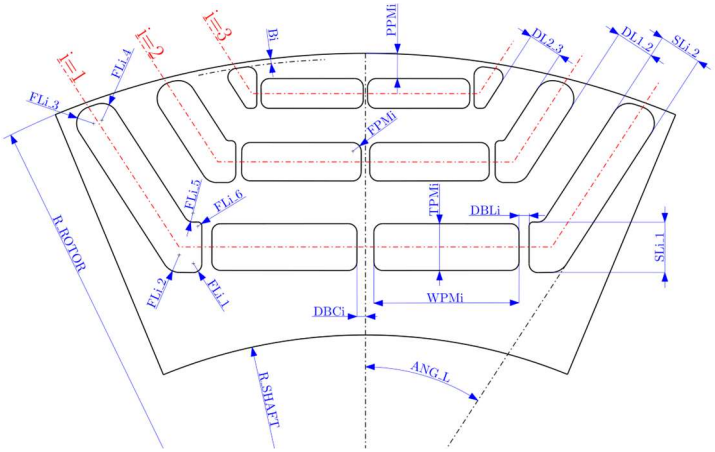

Fig. 36. Geometric variables of the rotor.

From a theoretical point of view, all these variables might be included in the optimization process to let the algorithm find the optimal design of the rotor. Nevertheless, the reduction of the number of variables is pursued to remove the irrelevant possible solutions and to limit the computational effort. Therefore, a parametric analysis is performed to identify the most impacting geometric features from both the electromagnetic and structural points of view. The monitored outputs are the mean torque, the torque ripple and the maximum equivalent von Mises stress.

Despite that, only the mean torque and ripple are chosen to drive this analysis, since they refer to the global performance of the motor. In fact, the variation of

every single parameter of the rotor geometry might influence the output torque and/or its ripple. On the contrary, from a structural point of view, the components of stress are local quantities, which vary within the FE domain. For this reason, the equivalent von Mises stress does not reveal itself to be a suitable quantity for this parametric analysis, but it is crucial to consider the stress state when it is appropriate to be prescribed.

The maximum volume of the rotor is imposed equal to the original configuration; so the outer radius of the rotor (*R_ROTOR*) and the angular opening of the flow barriers (*ANG_L*) are set to 95 mm and 33 degrees, respectively.

As a consequence, only the geometric parameters that define the magnet slots, the bridges, and the rotor inner radius are considered in the following preliminary analysis. Thus, the 44 design variables are considered each at 5 levels. For each model, only one geometric parameter is varied; so, 220 rotor configurations are computed.

For the sake of brevity and graphic clarity, Fig. 37 shows the impact of four design variables on the mean torque and the torque ripple. Each geometric variable is scaled with respect to its original value. A small variation of the shaft radius (*R_SHAFT*) ratio corresponds to a sudden change in mean torque and in torque ripple. These two considerations have led the authors to consider *R_SHAFT* as a design variable for the following multi-objective optimization process. In addition, if both the electromagnetic outputs have exhibited strong gradients, the choice of this design variable is not affected by structural considerations.

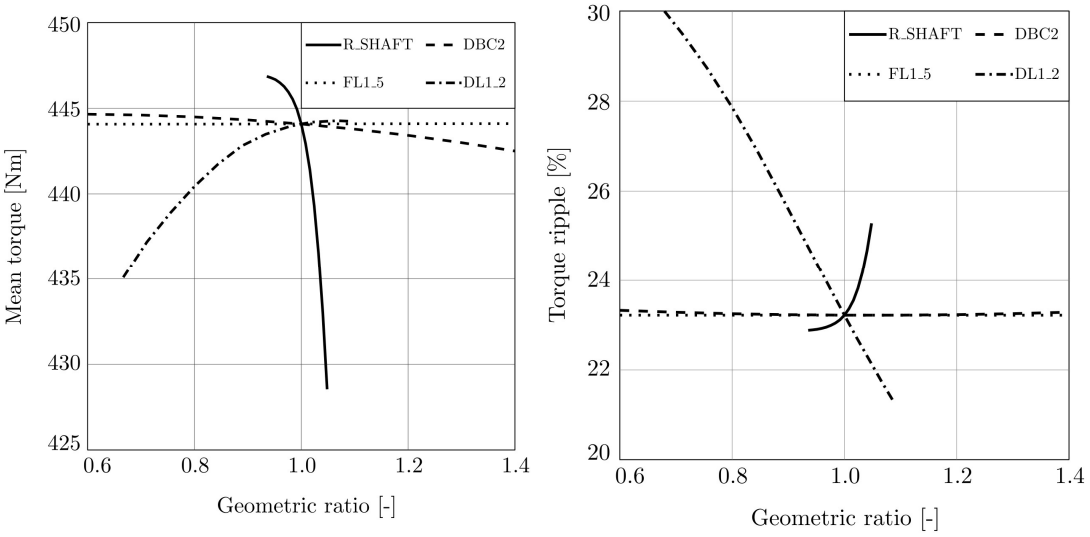

(a) (b)

Fig. 37. Influence of four rotor parameters on (a) mean torque and (b) torque ripple.

The fillet ratio of layer 1 (*FL1_5*) remains almost constant, meaning that it has a negligible effect on torque and torque ripple. As a consequence, this parameter is fixed to the reference value and it is excluded from the following optimization.

In layer 2, the semi-thickness of the central bridge (*DBC2*) has influenced the mean torque, whereas its contribution is negligible on the torque ripple. As a result of this, *DBC2* might be decreased to maximize the mean torque with no variation of the ripple. The optimal value of this parameter is reached by simply reducing it from the reference value of 0.5 mm to 0.35 mm. The new lower bound is determined by structural simulations where the von Mises contour plot is monitored and it does not exceed the yield stress.

In addition, when the air barrier distance between layers 1 and 2 (*DL1_2*) has increased, the mean torque has positively increased as well, whereas the torque ripple has decreased. Therefore, this parameter is moved to its upper bound, from 4.5 mm to 5.3 mm, for the next multi-objective optimization.

Table 2 summarizes the result of the parametric analysis. 23 of 44 design variables are excluded from the next optimization phase, thus reducing the computational effort. Two sub-categories are defined: *E-O* (Excluded – Original) and *E-M* (Excluded – Modified). The *E-O* (Excluded – Original) parameters are excluded by the following optimization algorithm, thus they are imposed as fixed. For instance, one of the fillet radii of the first air barrier (*FL1_5*) belongs to this category, see Fig. 37. The *E-M* (Excluded – Modified) quantities are modified to more suitable values than the reference one, and then they are excluded from the optimization. For instance, DBC2 refers to this category. In detail, 13 geometric features belong to the *E-O* group, while the remaining 10 are modified through practical considerations and are part of the *E-M* category. The rotor quantities labelled as *DV-O* (Design Variable – Original) are included in the optimization process starting from the original rotor configuration such as the *R_SHAFT* parameter. Finally, the acronym *DV-M* (Design Variable – Modified) has referred to geometric parameters that have increased the performance of the rotor with respect to its original configuration. Then, these parameters are included in the optimization process. For instance, *DL1_2* belongs to this group.

Table XI

DESIGN VARIABLES OF THE ORIGINAL CONFIGURATION AND THE RESULTS OF THE PARAMETRIC ANALYSIS

Variable label	Description	Original configuration [mm]	Parametric analysis results [mm]	Comment
B1	Thickness of the first layer external bridge	0.6	0.6	DV-O
B2	Thickness of the second layer external bridge	0.6	0.6	DV-O
B3	Thickness of the third layer external bridge	0.6	0.6	DV-O
DBC1	Half thickness of the first layer central bridge	1.0	1.0	DV-O
DBC2	Half thickness of the second layer central	0.5	0.35	E-M
DBC3	Half thickness of the third layer central bridge	0.25	0.25	E-O
DBL1	Thickness of the first layer lateral bridge	1.2	1.2	DV-O
DBL2	Thickness of the second layer lateral bridge	0.7	0.7	DV-O
DBL3	Thickness of the third layer lateral bridge	0.5	0.5	E-O
DL1_2	Distance between the first and second layer air barriers	4.5	5.3	DV-M
DL2_3	Distance between the second and third layer air barriers	4.0	4.2	DV-M
FL1_1	1st fillet of the first air barrier	1.0	1.5	E-M
FL1_2	2nd fillet of the first air barrier	2.0	1.2	E-M
FL1_3	3rd fillet of the first air barrier	2.0	2.8	E-M
FL1_4	4th fillet of the first air barrier	2.0	0.8	E-M
FL1_5	5th fillet of the first air barrier	1.0	1.0	E-O
FL1_6	6th fillet of the first air barrier	0.5	0.5	E-O
FL2_1	1st fillet of the second air barrier	1.0	1.5	E-M
FL2_2	2nd fillet of the second air barrier	2.0	1.5	E-M
FL2_3	3rd fillet of the second air barrier	2.0	2.5	DV-M
FL2_4	4th fillet of the second air barrier	2.0	0.8	E-M
FL2_5	5th fillet of the second air barrier	0.5	0.5	E-O
FL2_6	6th fillet of the second air barrier	0.5	0.5	E-O
FL3_1	1st fillet of the third air barrier	0.5	0.5	E-O
FL3_2	2nd fillet of the third air barrier	0.5	0.5	E-O
FL3_3	3rd fillet of the third air barrier	1.0	1.5	DV-M
FL3_4	4th fillet of the third air barrier	1.0	0.5	E-M
FPM1	Fillets of the first layer magnets	1.0	1.0	E-O
FPM2	Fillets of the second layer magnets	1.0	1.0	E-O
FPM3	Fillets of the third layer magnets	1.0	1.0	E-O
PPM1	Radial position of the first layer magnets	20.0	20.0	DV-O
PPM2	Radial position of the first layer magnets	10.5	10.5	DV-O
PPM3	Radial position of the first layer magnets	3.0	3.0	DV-O
R_SHAFT	Rotor radius at shaft	62.0	62.0	DV-O
SL1_1	Air barrier height (near to magnet) of the first	5.9	5.9	E-O
SL1_2	Air barrier height of the first layer	5.0	4.2	E-M
SL2_1	Air barrier height (near to magnet) of the	4.9	4.9	E-O
SL2_2	Air barrier height of the second layer	4.5	4.5	DV-O
TPM1	Thickness of the first layer magnets	5.5	5.5	DV-O
TPM2	Thickness of the second layer magnets	4.5	4.5	DV-O
TPM3	Thickness of the third layer magnets	3.5	3.5	DV-O
WPM1	Width of the first layer magnets	17.0	17.0	DV-O
WPM2	Width of the second layer magnets	14.0	14.0	DV-O
WPM3	Width of the third layer magnets	12.0	12.0	DV-O

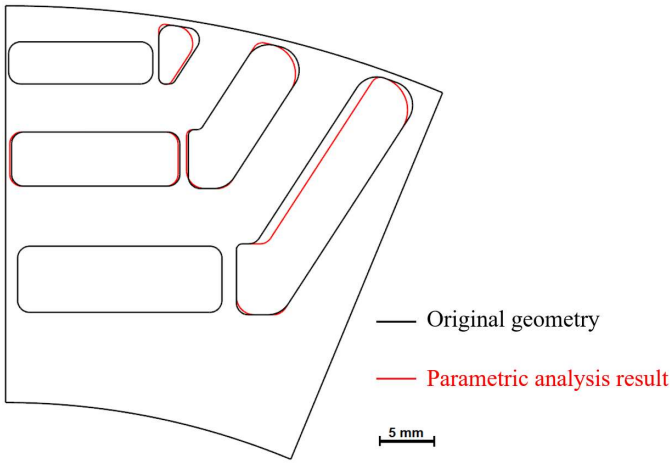

Fig. 38. Comparison between the original geometry of the rotor and the result of the parametric analysis, the visualization of the geometries has not been scaled.

Fig. 38 compares the original rotor geometry with the result obtained from the parametric study, which represents a sub-optimum; however, it becomes the starting configuration for the next multi-objective optimization. In detail, Table XII compares the three outputs, *i.e.* mean torque, ripple and equivalent von Mises stress, for both the aforementioned rotor configurations. A considerable reduction of the ripple is evaluated, while the mean torque and the maximum von Mises stress are unaltered. In particular, the variation of the torque ripple significantly impacts on the motor performance. In fact, a high ripple could produce undesired vibrations and annoying noise. For these reasons, the authors identified the torque ripple to be the most important output to be reduced, while the mean torque and the equivalent von Mises stress are kept substantially unchanged. To conclude, by adopting the proposed suboptimal solution as the starting point for the next multi-objective optimization, the optimal solution configuration can be reached more quickly.

Table XII
COMPARISON OF THE RESULTS OF REFERENCE GEOMETRY AND OF THE PARAMETRIC STUDY

	Reference	**Post parametric analysis**	**Δ%**
Mean torque [Nm]	444.09	442.45	-0.37
Ripple [%]	23.22	16.96	-6.26
Maximum von Mises stress [MPa]	573.47	573.88	+0.07

4.2.7 Multi-physics and Multi-objective Optimization

This sub-section describes the multi-objective optimization process. The resulting geometry of the parametric study is iteratively modified to reach the optimum. In

detail, three objective functions will be considered: the mean torque of the motor will be maximized, while the torque ripple and the stress of the rotor will be minimized. The design constraints are related to the volume of the magnets and to the electromagnetic and structural performance. The design domain is the rotor and the design variables are the 21 parameters reported in Table XI.

Since the optimization process involves both the electromagnetic and the structural fields, a multi-physics approach is applied. Since the multi-objective approach is adopted, multiple optimal rotor geometries are identified lying on a Pareto front.

Altair Hyperstudy 2021.2 is used to couple the magnetic and structural analyses. The electromagnetic simulation is solved by Altair Flux 2021.2, while MSC Marc is employed for the stress-based simulations. Fig. 39 shows the algorithm used to collect the Pareto front of the optimized solutions. The MOGA implemented in Hyperstudy is employed.

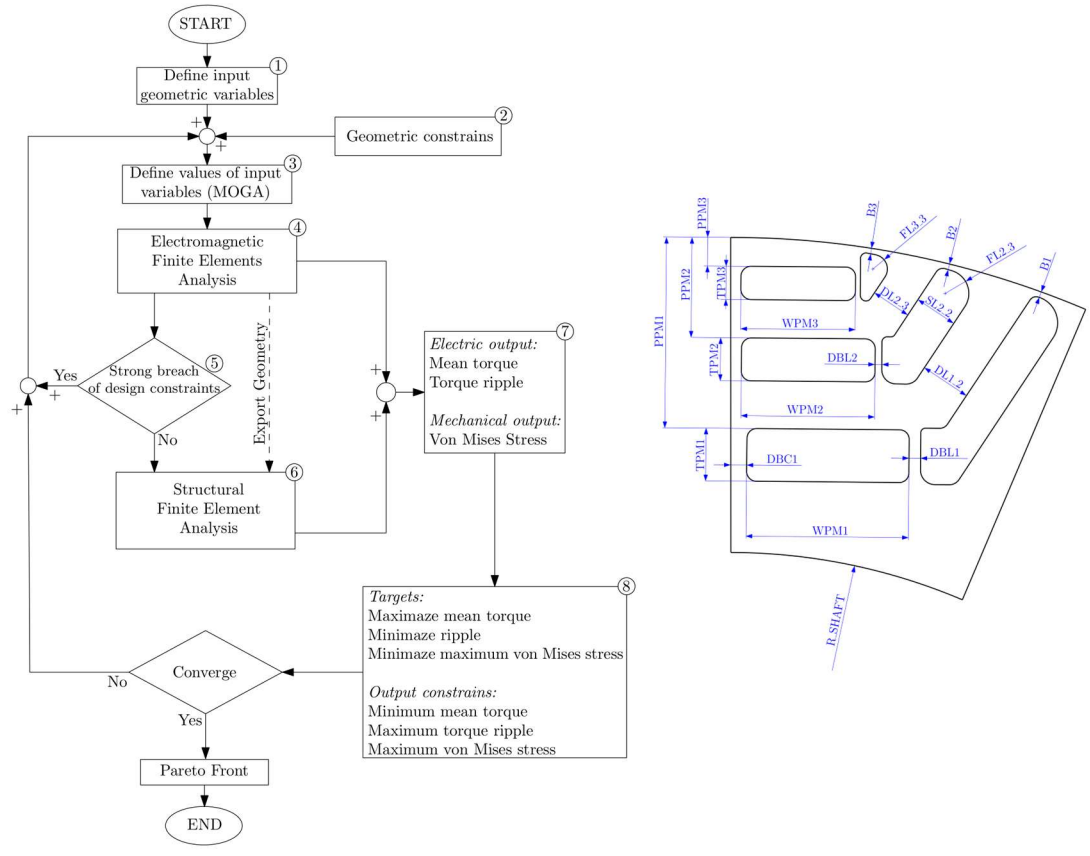

(a) (b)

Fig. 39. (a) Workflow of the multi-physics and multi-objective optimization; (b) input design variables of the rotor.

This stochastic algorithm is population-based, whereas deterministic algorithms are usually gradient-based. Thus, even if the latter usually converges faster, the

result could identify a local minimum and the global optimum configuration could not be reached. In detail, the population size is set equal to 100, more than twice the number of the design variable. Also, the elite population is set to 10% and, the minimum and the maximum number of iterations are set equal to 25 and 75, respectively.

The input design variables are defined at the beginning of the algorithm, see box 1 of Fig. 39 (a) and the labelling in Fig. 39(b). During the following iterative loops, these design variables are modified and tested to find the optimal solutions. Each design variable ranges within the intervals of Table XIII. In particular, these values are selected considering the results of the previous parametric study, of the manufacturing constraints, and of the geometric constraints.

The geometric constraints, box 2 of Fig. 39(a), are included to the MOGA algorithm, where the values of the input variables are a function of the initial and elite population, see box 3. Therefore, the defined rotor geometries are tested employing the electromagnetic FE solver, see box 4. Then, the electromagnetic outputs are collected, see box 5. If one of the electromagnetic outputs, mean torque and torque ripple, exceeds the design threshold of 10%, the iterative loop is interrupted and this geometry is rejected from the optimal solutions. Thus, a new rotor geometry is considered moving back to box 3. Conversely, if the electromagnetic output remains below 10%, its structural FE analysis is performed, box 6. The condition in box 5 increases the efficiency of the algorithm since the structural simulation of a geometric solution with poor electromagnetic properties is avoided.

Then, the outputs of both the electromagnetic and the structural simulations are collected, box 7, and compared with the targets of the optimization process, box 8. Finally, when the convergence of the results is reached, the Pareto front is built and the simulations are stopped.

Table XIII

RANGES AND STEP SIZES OF GEOMETRIC INPUT VARIABLES

Variable	Nominal value	Min [mm]	Max [mm]	Step
B1	0.6	0.5	1.5	0.10
B2	0.6	0.5	1.5	0.10
B3	0.6	0.5	1.5	0.10
DBC1	1.0	0.5	1.2	0.10
DBL1	1.2	0.6	1.8	0.10
DBL2	0.7	0.5	0.9	0.10
DL1_2	5.3	4.5	6.0	0.10

DL2_3	4.2	3.5	5.0	0.10
FL2_3	2.5	2.1	2.9	0.20
FL3_3	1.5	1.3	2.1	0.20
PPM1	20.0	19.0	21.0	0.20
PPM2	10.5	9.5	11.5	0.20
PPM3	3.0	2.0	3.6	0.20
R_SHAFT	62.0	57.0	63.0	0.50
SL2_2	4.5	4.0	5.5	0.10
TPM1	5.5	4.5	6.5	0.20
TPM2	4.5	3.5	5.5	0.20
TPM3	3.5	2.9	4.1	0.20
WPM1	17.0	16.0	18.0	0.20
WPM2	14.0	13.2	14.8	0.20
WPM3	12.0	11.0	13.0	0.20

4.2.8 Geometry Constraints

The design of the rotor is constrained by geometrical relationships, which prevent unfeasible geometries. In fact, the manufacturability is considered by adopting 0.5 mm as the minimum size of the bridges.

Referring to the first layer of magnets, which is the nearest to the inner radius, the dimensions of this slot are constrained by (9), where the subscript n stands for nominal, and it refers to the nominal referring quantities of the given parameter.

$$(WPM1+DBC1+DBL1)-(WPM1_n+DBC1_n+DBL1_n) \leq 1.4\ mm \quad (9)$$

Equation (10) imposes the same consideration for layer 2, which is the mid-layer of magnets:

$$(WPM2+DBL2)-(WPM2_n+DBL2_n)+\frac{(DL1\_2+SL2\_2)-(DL1\_2_n+SL2\_2_n)}{cos(ANG\_L)} \leq 0.3\ mm \quad (10)$$

Consistently, the minimum feasible size of the bridges for the third layer, which is the farthest from the shaft axis, is constrained by (11):

$$(WPM3-WPM3_n)+(FL3\_3-FL3\_3_n)+\frac{(DL1\_2+SL2\_2+DL2\_3)}{cos(ANG\_L)}-\frac{(DL1\_2_n+SL2\_2_n+DL2\_3_n)}{cos(ANG\_L)} \leq 0.8\ mm \quad (11)$$

Then, for the mid-magnets, the fillet of their slot is constrained to avoid sharped edges or collapsed geometries:

$$SL2\_2-FL2\_3 \geq 1.6\ mm \quad (12)$$

To conclude the enumeration of the geometric constraints, the maximum volume of the magnets is assumed to be lower or equal to the volume of the starting rotor configuration to limit the adoption of rare-earth metals. However, the slot of magnets is assumed to be rectangular, where their size is included in the optimization. The magnets' area is constrained according to (13).

$$TPM1*WPM1+TPM2*WPM2+TPM3*WPM3 \leq 198.5\ mm^2 \quad (13)$$

4.2.9 Electromagnetic Part: Objectives, Design Constraints and FE Model Details

The required electromagnetic outputs are referred to the mean torque and torque ripple, the latter being calculated as in (14), in which T_{max}, T_{min} and T_{mean} are the torque maximum, minimum and mean value, respectively. In particular, the electromagnetic objective functions aim at maximizing the first output and at minimizing the latter one. Even if the mean torque and the torque ripple are set as objective functions, they are constrained too, as shown in (15) and (16).

$$T_{ripple} = \frac{T_{max}-T_{min}}{T_{mean}} *100 \quad (14)$$

$$Minimum\ mean\ torque\ 5000\ rpm \geq 435\ Nm \quad (15)$$

$$Maximum\ torque\ ripple\ at\ 5000\ rpm \leq 10\ \% \quad (16)$$

To conclude, the FE electromagnetic model employed in the optimization algorithm is consistent with the discussion of sub-section 4.1.4.

4.2.10 Structural Part: Objectives, Design Constraints and FE Model Details

The structural FE analyses included within the optimization process start from the geometry previously solved by Altair Flux 2021.2. First, the rotor is discretized by adopting Altair Hypermesh 2021.2; then, the FE model is set up and computed by MSC Marc Mentat 2020.1.

The minimization of the stress field within the rotor is the objective function of the FE structural optimization. Despite that the equivalent von Mises stress represents the structural objective function, it is constrained as follows:

$$Equivalent\ von\ Mises\ stress \leq 571\ MPa \quad (17)$$

Even if the stress field should remain below the yielding stress (570 MPa), the authors have accepted the occurrence of localized plastic strains due to the first start-up of the motor when the magnets adapt to the slots. This is the well-known elastic shakedown effect. Hence, local plastic strains of 0.1% are allowed and it occurs at 571 MPa level of stress.

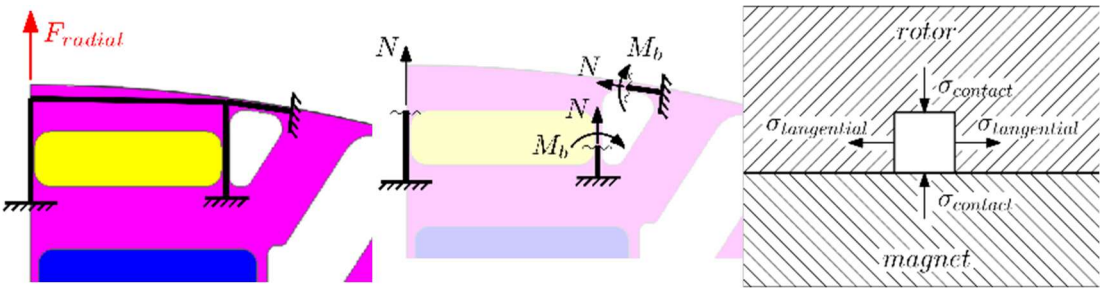

(a) (b) (c)

Fig. 40. (a), (b) Internal loadings on rotor's bridges with beam analogy; (c) tangential and contact stress at the interface between rotor and magnet.

The structure might be modelled as three beams connected one to each other and fixed at their extremities; it represents a redundant structure, see Fig. 40(a). The external load F_{radial} is generated by the centrifugal acceleration applied to the rotating mass of the rotor and of the magnets. Fig. 40(b) explains how the internal loading act on the bridges modelled as beams, *i.e.* bending moment (M_b) and normal force (N). In the present work, the influence of the bending moment is included in the FE model, whilst it was neglected by Barcaro et al. [56].

Furthermore, the reaction forces generated by the contact between the magnet and the rotor are considered, whereas, their normal contact stress $\sigma_{contact}$ acting on the beam is neglected, see Fig. 40(c). In fact, a theoretical issue is encountered during the structural FE simulation, since a contact problem acts simultaneously with the centrifugal load that pushes the magnets towards the periphery of their slots. The contact pressure between the slot and the magnet might become singular. This issue is partially solved by considering the elastoplastic material law of the rotor thus allowing the redistribution of stress induced by the plastic field. However, the contact problem disturbs the optimization algorithm. In fact, the local stress of the rotor depends also on the contact normal stress and on the mesh size. A small perturbation of the rotor geometry could significantly affect the contact stress thus impacting the equivalent von Mises stress. This type of issue is mathematically called ill-posed problem; *i.e.* a small variation of the inputs leads to a big variation of the outputs. To sum up, considering the stresses that occurred at the contact interaction, the optimization algorithm could lead to unphysical results after an almost endless computational time.

As a consequence, the strategy used to monitor the sole tangential stress $\sigma_{tangential}$ is presented in the following. Truss elements (two-dimensional, two-node, straight truss, two coordinates and two degrees of freedom) are added to all the borders of

the rotor, see Fig. 41. These truss elements have behaved as strain gauges since they can bore axial loads only. In particular, a negligible cross-section is applied to these elements without modifying the rotor stiffness. The same material of the rotor is assigned to these auxiliary elements. The stress state of these truss elements is monitored solely, since the maximum stress is registered always on the rotor borders. No sub-superficial maxima of stress are detected; this implies that no Hertzian-type contact arises. To sum up, this approach isolates $\sigma_{tangential}$ from the global stress tensor.

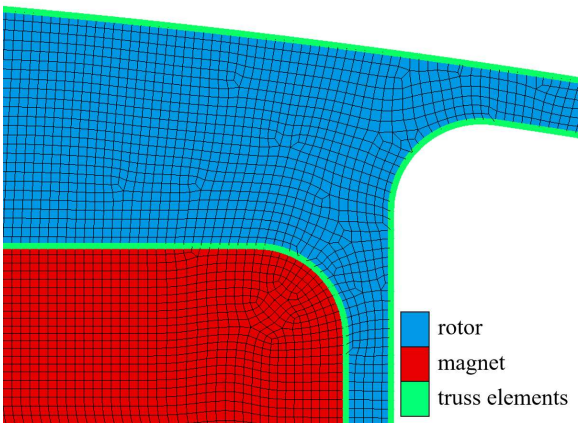

Fig. 41. The FE domain of the analysis: detail view.

4.2.11 Results and Discussions

This section shows the results of the optimization algorithm. The computations are performed by a workstation equipped with Intel(R) Xeon(R) E-2126G CPU and 64 Gb memory RAM. Three CPUs are employed in parallel, 4850 rotor geometries are tested and each loop of optimization (consisting of an electromagnetic and a structural simulation) has required 5 minutes.

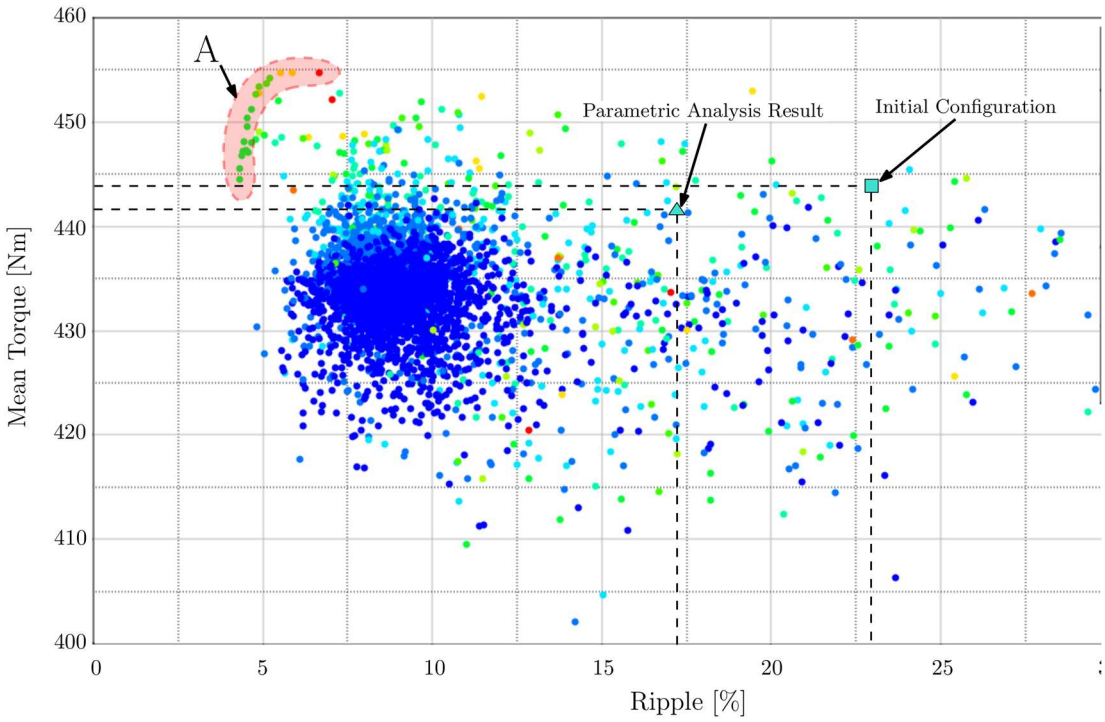

Fig. 42. Optimization results.

Fig. 42 retrieves all the simulations performed during the optimization process and placed them in a scatter plot based on the three monitored outputs: mean torque, torque ripple, and maximum equivalent von Mises stress. Each point identifies one rotor layout. The ordinate refers to the mean torque, while the torque ripple is evaluated along the abscissa. So that, the maximum stress is identified by the coloured scale. Two relevant rotor configurations are highlighted: 1) the original layout by the square, 2) the geometry resulting from the parametric analysis by the triangle. The mean torque exhibits an undesired slight drop, while a beneficial decrease in torque ripple is observed and, finally, the maximum stress is substantially unchanged.

During the optimization, several solutions are agglomerated at 440 Nm of mean torque and 7.5% of torque ripple, where the maximum stress equals 570.6 MPa. These solutions are closer to the configuration obtained by the parametric study than to the original rotor. This proves that the parametric analysis is useful to speed up the optimization algorithm. In addition, the scatter plot shows multiple optimal solutions characterized by a lower value of mean torque if compared with the original design, whereas the torque ripple is more than halved and the maximum stress is decreased by 3 MPa.

Fig. 43 displays the 16 configurations that satisfy the design constraints. These points are non-dominated and, therefore, represent the Pareto front. Their

maximum stress ranges between 570 MPa and 571 MPa, where the rotor material switches from the elastic field to the incipient plastic state.

Table XIV compares the geometry resulting from the parametric analysis with the optimal solutions obtained by the multi-objective optimization. The first configuration labelled as 1 is selected as the optimal design.

Fig. 44 compares the solution of the parametric analysis with the optimized layout. The main geometrical discrepancies deal with: 1) the decrease of the inner radius of the rotor (*R_SHAFT*), 2) the increase of the radial position of the first and the third layers of magnets (*PPM1*, *PPM3*), 3) the decrease of the central bridge of the first layer (*DBC1*), 4) a shift of the lateral bridge of the second layer (*DBL2*), 5) the variation of the length-to-height ratio of all the magnets, and, finally, 6) a general increase of the air barriers of all the layers.

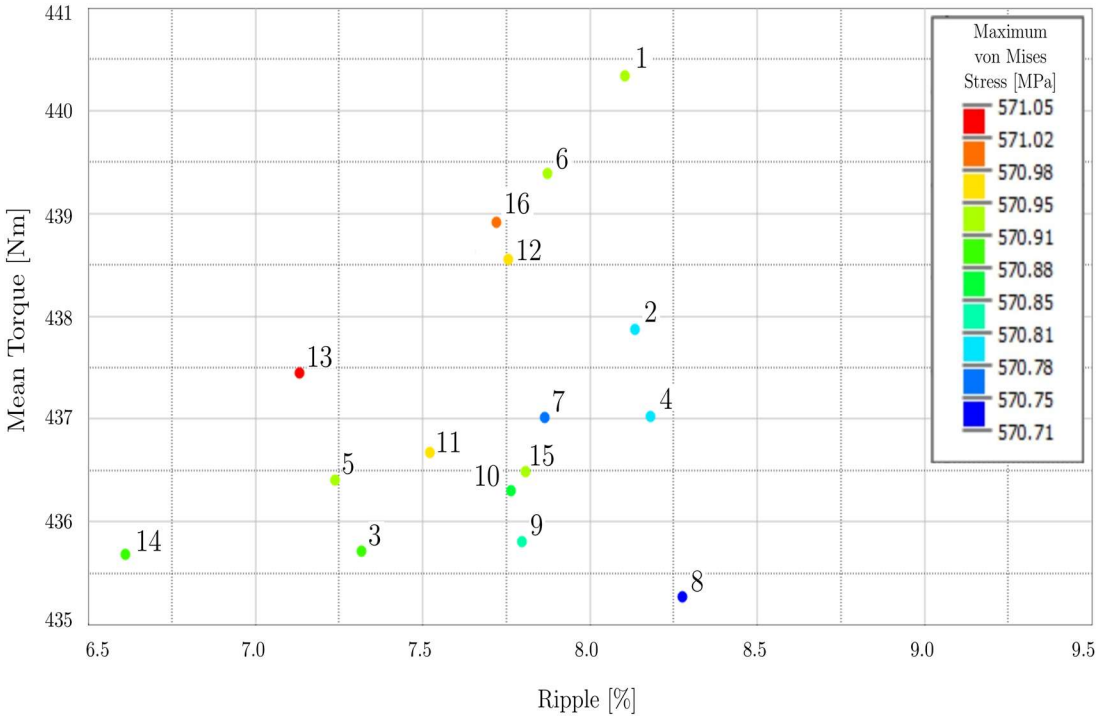

Fig. 43. The solutions of the optimization representing the Pareto front.

Table XIV

LIST OF OPTIMAL SOLUTIONS AND COMPARISON OF THE FINAL RESULTS WITH THE STARTING ROTOR CONFIGURATION OF THE OPTIMIZATION

Identification	Mean torque	Δ%	Ripple	Δ%	von Mises stress	Δ%
Parametric	442.50		16.96		573.88	
1	**440.34**	-	**8.11**	**-8.85**	**570.93**	-
2	437.88	-	8.14	-8.82	570.80	-
3	435.71	-	7.32	-9.64	570.90	-
4	437.03	-	8.18	-8.78	570.78	-
5	436.40	-	7.24	-9.72	570.93	-
6	439.39	-	7.87	-9.09	570.92	-

7	437.01	-	7.87	-9.09	570.77	-
8	435.27	-	8.28	-8.68	570.71	-
9	435.80	-	7.80	-9.16	570.82	-
10	436.30	-	7.76	-9.20	570.87	-
11	436.67	-	7.52	-9.44	570.98	-
12	438.55	-	7.76	-9.20	570.98	-
13	437.45	-	7.13	-9.83	571.03	-
14	435.68	-	6.61	-	570.91	-
15	436.48	-	7.81	-9.15	570.94	-
16	438.91	-	7.72	-9.24	571.00	-

In particular, a reduction of the *R_SHAFT* has led to a lower saturation below the magnets of the first layer, see Fig. 45(a), and to a higher stiffness of the rotor which better supports these magnets thus reducing the stress field.

The reduction of *PPM1* positively impacts the maximum tensile stress in the first layer's lateral bridge between the magnet and the air barrier, decoupling the influence of the stress concentration factor of the rotor's slot to the nominal stress due to axial force and bending moment. Conversely, when *PPM3* decreases the electromagnetic performance increases thanks also to the decrease of the length-to-height ratio. Furthermore, the values of *DBC1* and *DBL2* are reduced, forcing the rotor material of the respective bridges to achieve the yielding stress.

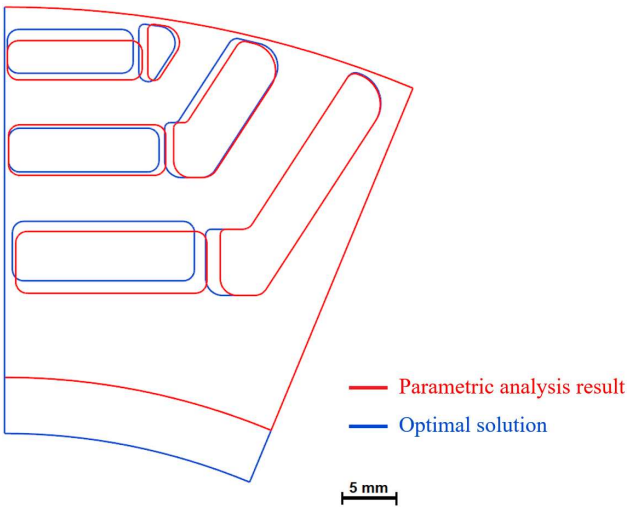

Fig. 44. Comparison between the result of the parametric analysis and chosen optimal geometries, the visualization of the geometries has not been scaled.

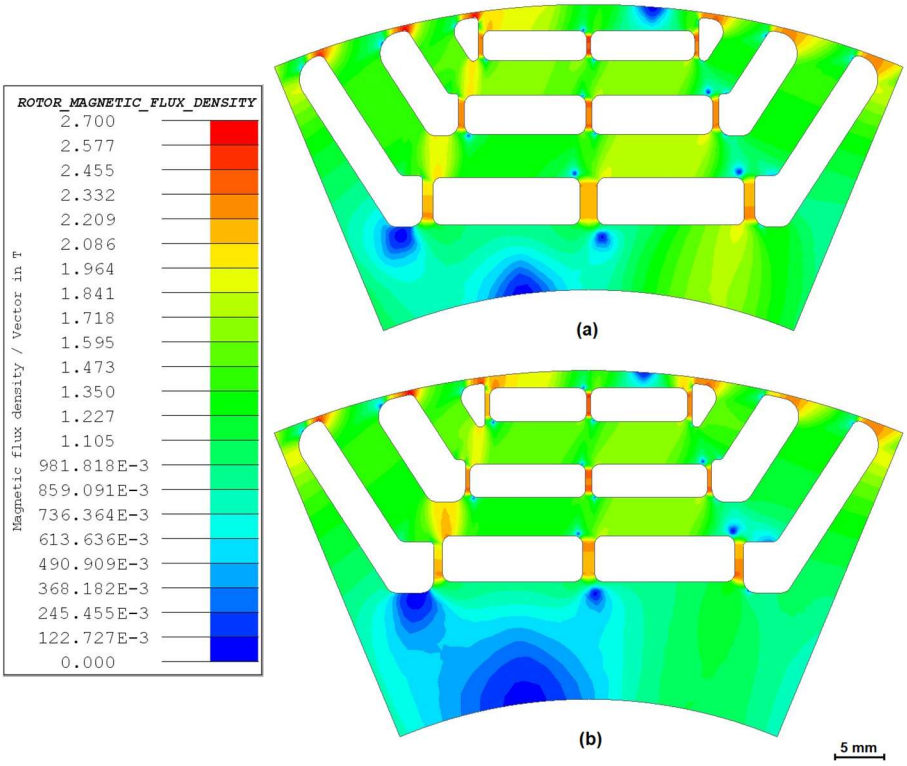

Fig. 45. Field map distribution of magnetic flux density in (a) post parametric analysis and (b) optimal solution.

A reduction of the length-to-height ratio of the magnets leads to a positive reduction of the arm and, therefore, of the bending moment acting on the respective lateral bridges.

Considering that the axial length of the electric machine is unchanged, the volume of the magnets is reduced by 8.4%, whereas the rotor mass is increased of about 10%. As a future development, a design constraint on the mass of the rotor could be added to the optimization process.

Lastly, an electromagnetic-only optimization is performed for comparison, considering the same electromagnetic objectives and constraints of the multi-physics one. The obtained solutions are located in the highlighted area A of Fig. 42. Even if very high values of mean torque and low values of torque ripple are achieved, the maximum equivalent von Mises stress of these solutions overly exceeds the yielding stress, confirming that the structural analysis is a useful tool to obtain a feasible and optimal solution.

4.2.12 Post-optimization Thermal Analysis

To validate the optimal solution, thermal analysis has been performed on this geometry after the optimization. Starting from the electromagnetic model and still

using Altair Flux 2021.2, a steady state 2D FE thermal model has been set up to determine the response of the motor. Briefly, different heat thermal sources have been imposed on the regions of the domain and calculated considering the iron losses and the Joule losses obtained from the electromagnetic transient analysis. Two different convective heat transfer boundary conditions have been imposed at the outer edge of the stator and at the inner edge of the rotor (at the interface with the shaft).

As can be observed in Fig. 46, a thermal comparison has been performed between the original geometry (Fig. 46.a) and the optimal solution chosen (Fig. 46.b). The temperature of the magnets close to the airgap is ≈122 °C in both cases. At this temperature value, the B-H characteristic of the N38UH magnets is still in the third quadrant, thus meaning that the demagnetization is avoided.

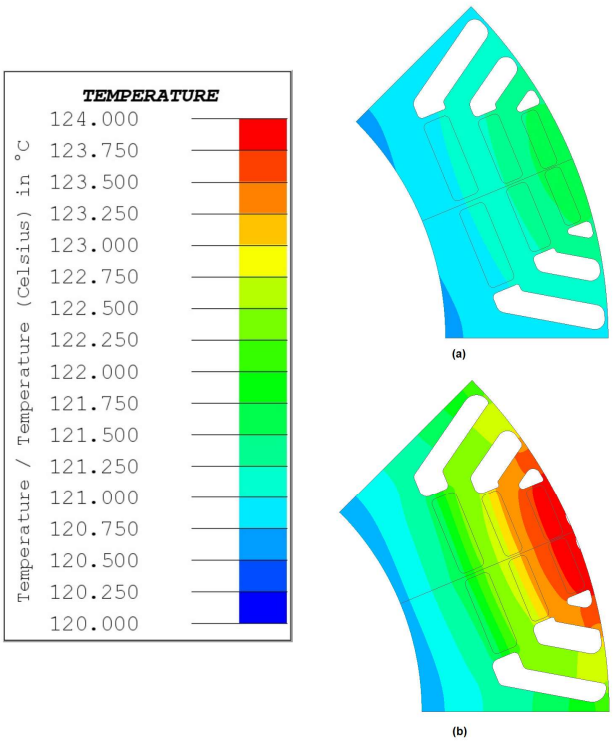

Fig. 46. Temperature contour plot of the original geometry (a), and optimal solution (b).

4.2.13 Conclusions

The present work has described a methodology for the optimization of the rotor of a PMaSynRMs for traction applications. A multi-physics and multi-objective algorithm was set up to consider both electromagnetic and structural aspects. As a

result of this, the original geometry of the rotor was improved obtaining an overall reduction in torque ripple of 15.1% and maintaining approximately the same values of mean torque and maximum von Mises stress.

The literature is rich in papers that deal with the optimization of electric machines with robust electromagnetic analysis. These facilitate mechanical engineers in the electromagnetic field. However, methodologies with robust structural analyses are almost absent or oversimplified. Therefore, this work aims at providing structural guidelines relative to the rotor design of PM motors which might facilitate electrical engineers in the structural field.

Moreover, the presented optimization algorithm considers details of the structural modelling (as the contact interaction between the magnets and their slots, stress concentration factors, and rotor-shaft coupling) that need specific and accurate set-ups. In addition, the post-processing of the structural output influences the modelling strategy. For example, in the presented methodology, the adoption of truss elements applied to each border of the rotor is mandatory.

4.2.14. Chapter's Closing Remarks

As this thesis demonstrates, the ongoing development and optimization of electric motors in the automotive industry hold significant potential for advancing both performance and sustainability. From innovative motor topologies to material selection, the research presented lays the groundwork for a new generation of vehicles that meets the demand for efficiency while addressing critical environmental concerns. The implications for the automotive sector are clear: to stay competitive and sustainable, manufacturers must prioritize reducing the use of RE materials and exploring alternative motor designs. This shift presents both a challenge and an opportunity, which the case studies in the following chapter will explore in detail.

Chapters 5, 6 and 7 present a detailed series of case studies that explore different approaches to reducing or eliminating the use of RE elements in high-performance motors across different sectors. These case studies highlight practical applications in automotive (Chapter 5), heavy-duty machinery (Chapter 6) and aerospace (Chapter 7), demonstrating how cutting-edge design strategies can meet both performance and sustainability goals.

From racing cars to aerospace applications, these case studies illustrate the challenges and solutions associated with RE reduction, focusing on key performance indicators such as torque density, efficiency, and cost-effectiveness. Each case study reflects advancements made through electromagnetic analysis and structural considerations, achieving significant reductions in RE usage without compromising performance.

5. CASE STUDIES: RARE EARTH REDUCTION IN AUTOMOTIVE SECTOR

The works here reported are:

1. Combined Magnet Shaping and Asymmetries in Surface-Mounted Permanent Magnet Machines for Improved Torque Performance [1].
2. RE Materials Reduction in a Hypercar Propulsion System [2].

These projects focus on RE material reduction strategies in an FSAE motor and a hypercar propulsion system, respectively.

5.1 Combined Magnet Shaping and Asymmetries in Surface-Mounted Permanent Magnet Machines for Improved Torque Performance

5.1.1 Introduction

This sub-chapter focuses on a more advanced version of the motor presented in Chapter 4, scaled in performance to suit a hybrid propulsion system. It introduces an in-depth study of the effects of combining magnet shaping techniques with asymmetric magnet placement to reduce torque ripple in SPM machines. The research explores how unconventional magnet shaping and strategic asymmetry can enhance the performance of a motor designed specifically for a FSAE racing car. By utilizing a reverse-engineering approach, a detailed FE model was developed to thoroughly analyse the existing motor design.

The study primarily aims to optimize torque ripple reduction while maintaining high average torque levels, which is crucial in high-performance applications like racing. This innovative approach shows how substantial improvements in torque ripple can be achieved without compromising overall motor performance. The combination of these techniques, often addressed separately in existing literature, proves to deliver enhanced results when applied together.

5.1.2 Case Study Overview

The investigation on the torque ripple starts from the analysis of an existing PM machine with customized magnets' shape, properly tested (Fig. 47). A picture showing the rotor of such electrical machine is reported below in Fig. 48. In the next subsections, the main features of this case study and its 2D FE model are

described, also detailing the geometrical parametrization for the reverse engineering analysis of the machine.

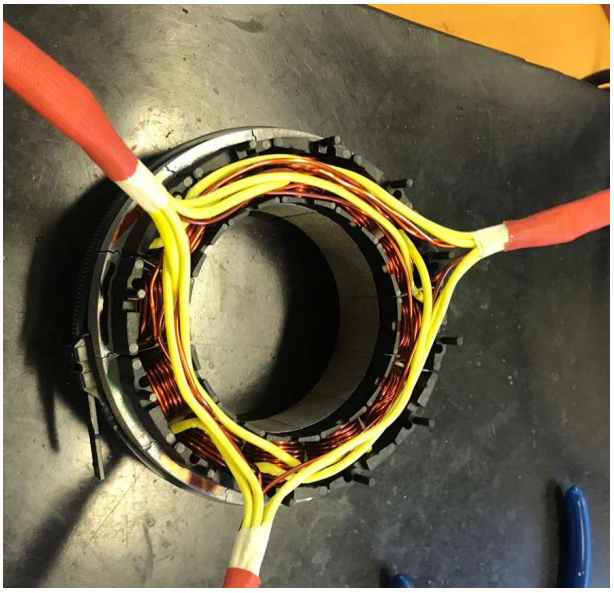

Fig. 47. Stator windings arrangement of the existing machine during test activity.

Fig. 48. Existing machine rotor.

A. Machine Description

The main parameters of the PM motor under study are reported in Table XV.

Table XV
MOTOR DETAILS

Winding Type	Tooth-wound	**Air gap thickness [mm]**	0.8
Pole number (p)	8	**Outer diameter [mm]**	135
Slot number	12	**Base speed [rpm]**	9600
Phase number	3	**Max magnet height [mm]**	4.2

Turns per coil/pole/phase	24	**PM material name**	C 8
		Core material name	M 470

By zooming on one of the PMs of Fig. 48, as done in Fig. 49, it can be observed that the magnet shape is not purely sinusoidal, and its external profile can be approximatively divided into 5 segments, as better shown in the subsection 5.1.2.C. The flaps highlighted in Fig. 49 have the function of sealing the PMs in their position. The holes in the rotor core (see Fig. 48) have the primary function of reducing weight and the rotational inertia, as well as to create axial venting gaps for improved thermal management. Concerning the stator structure, 12 slots hosting a three-phase tooth-wound winding are used as shown in Fig. 50.

The 2D FE model of the machine is then built considering the characteristics highlighted above and disregarding the effects due to the rotor flaps and holes, due the almost purely mechanical functions. However, their effects have been investigated through a FE analysis for the sake of completeness, showing a negligible impact on the main electromagnetic performance figures. The FE model details are provided in the next subsection.

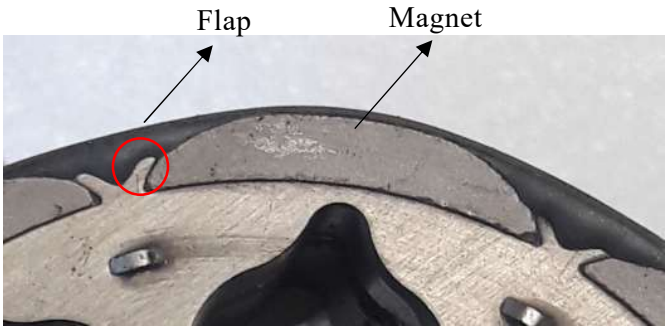

Fig. 49. Zoom on one of the PM.

B. FE-Model

The previously presented machine is modelled using the FE-based software Altair Flux. Given the machine symmetries, a pair pole is deemed to be sufficient for the analysis, and this is shown in Fig. 50.

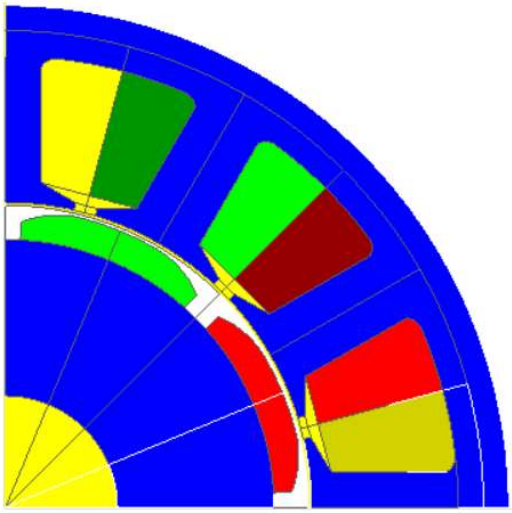

Fig. 50. 2D-FE model of the existing machine.

Concerning the electric circuit, a star-connection of the phases is assumed and a three-phase sinusoidal current supply is used to feed them. The electric circuit coupled with the FE model is shown in Fig. 51.

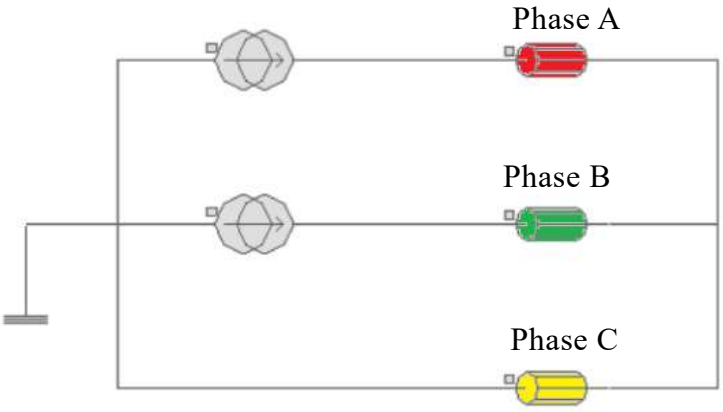

Fig. 51. Electric circuit coupled to the FE model.

C. Magnet Shape Parametrization

Given the shape of the PMs shown in Fig. 49, the magnets are modelled in Altair Flux considering their external profile as a result of 5 connected segments, as illustrated in Fig. 52 reproduces with a good approximation the real PM shape of the existing machine. Since the results which have led to this solution are not known or available, the machine FE model is parametrized using the variables P1, P2 and P3 seen in Fig. 52 and described in Table XVI. A multi-parametric analysis is then run aiming to compare the existing solution against a number of possible

alternatives and verify the effectiveness of the chosen PM shape on average torque and torque ripple. The results of this study are presented in Section 5.1.3.

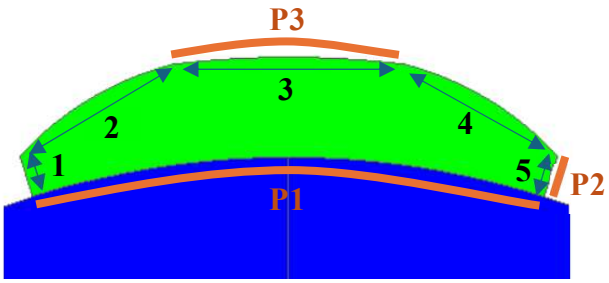

Fig. 52. PM geometrical parametrization.

Table XVI
MAGNET'S GEOMETRICAL PARAMETERS

Parameter	**Description**
P1	Magnet span [°]
P2	Height of the PMs' lateral part [mm]
P3	Span of the PMs' circular upper part [°]

5.1.3 FE Analysis Settings and results

A. Reference Geometry and Parametrization Data

As mentioned above, the scope of the multi-parametric analysis is to compare the existing PM machine against other designs. The easiest and most common SPM topology surely consists of arc-shaped magnets having a constant thickness along the circumferential direction. This standard layout can be observed in Fig. 48, and it is considered as reference machine for the multi-parametric study.

Using the developed FE model presented in Section 5.1.2, both the reference and the existing machines are analyzed in detail.

The most relevant quantities for the sake of this project are average torque (T_{avg}) and torque ripple (T_r). These can be observed in Fig. 54 and a comparative summary is provided in Table XVII, together with the parameters Px of both the reference and existing solutions. This preliminary analysis shows that the existing machine features a much-reduced T_r compared to the reference one, while T_{avg} is not significantly compromised.

In order to investigate a higher number of possible geometries, while maintaining the computational time acceptable (1-2 days) using the same software, the variation range and the step value of the parameters Px are selected as reported in

Table XVIII. Computational time reduction can be achieved by using optimization algorithms which should require a specific software. The multi-parametric simulation results are shown and compared in the next subsection.

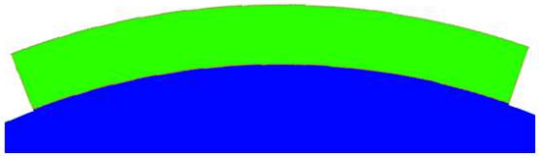

Fig. 53. Reference machine PM layout.

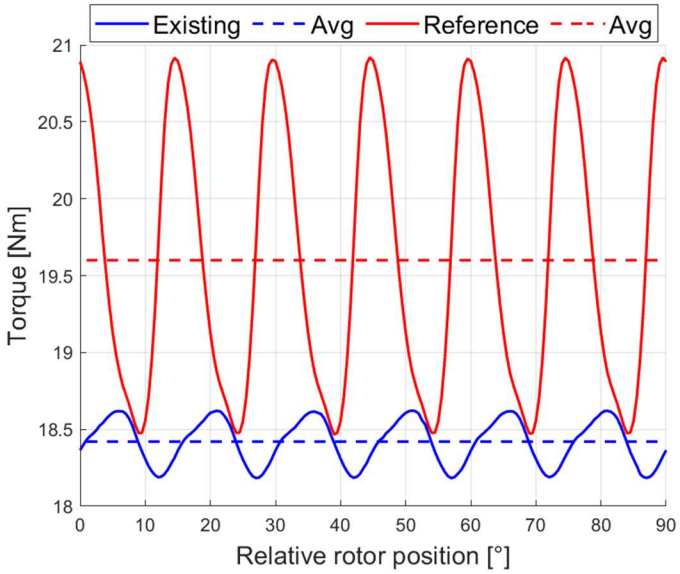

Fig. 54. Torque trend comparison among the existing and the reference machines with their respective mean values.

Table XVII

DETAILS AND RESULTS FOR THE REFERENCE AND EXISTING MACHINES

	P1 [°]	**P2 [mm]**	**P3 [°]**	**Tavg [Nm]**	**Tr [%]**
Reference	38.75	4.20	38.75	19.63	12.43
Existing	38.75	2.40	18.00	18.42	2.33

Table XVIII

PARAMETERS' VARIATION RANGE AND STEP VALUE FOR THE MULTI-PARAMETRIC ANALYSIS.

Parameter	**Range**	**Step value**
P1 [°]	33.75 ÷ 42.5	1.25
P2 [mm]	0.9 ÷ 3	0.3
P3 [°]	8 ÷ 32	2

B. Multi-parametric scenario results

The results of the 832 tested configurations are presented through a 4-D plot, in which the fourth dimension is reported with a colour scale. Therefore, in Fig. 55 and Fig. 56 the torque ripple and average torque are shown as functions of P1, P2 and P3, respectively. Each design corresponds to a dot. The best solutions in Fig. 55 are those shown in blue, as this colour corresponds to the minimum torque ripple. On the other hand, the best designs in Fig. 56 coincide with the orange/yellow dots, as these colours corresponds to the maximum average torque. In both figures, the dots referring to the existing machine (see Fig. 49 and Fig. 50) are highlighted.

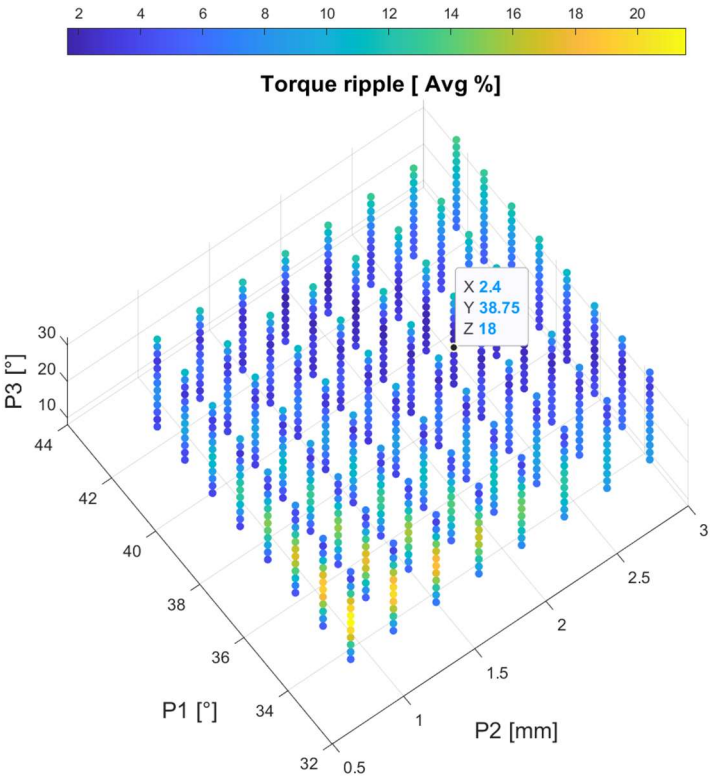

Fig. 55. Torque ripple as function of Px.

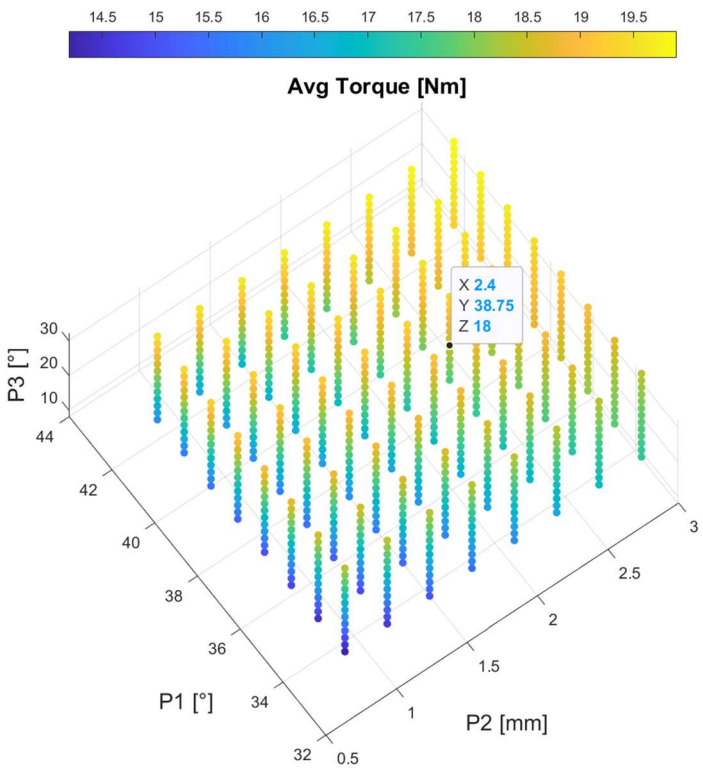

Fig. 56. Average torque as function of Px.

In Table XIX, a comparison among the existing machine, the reference one, the best design in terms of torque ripple (T_r best), and the best design in terms of average torque (T_{avg} best) is reported. The design "T_r best" achieves 86.88% and 30.04% ripple reduction compared to the reference and existing machine, respectively. Whereas the design "T_{avg} best" achieves an improvement by 1.37 % and by 8.03 % compared to the reference and existing machines, respectively, in terms of average torque. The results are summarized in Fig. 57. The design "T_r best" represents an optimal solution due to the minimum torque ripple achieved, but also due to its average torque being slightly higher than the existing machine. However, this solution is discarded in this particular case, because of the greater possibility of lateral demagnetization due to the lower value of the height (P2). This discarded design and the "T_{avg} best" configuration are shown in Fig. 58. The latter is also discarded due to the too high value of the torque ripple (21.57%). In conclusion, the existing machine is deemed to be the best trade-off design choice.

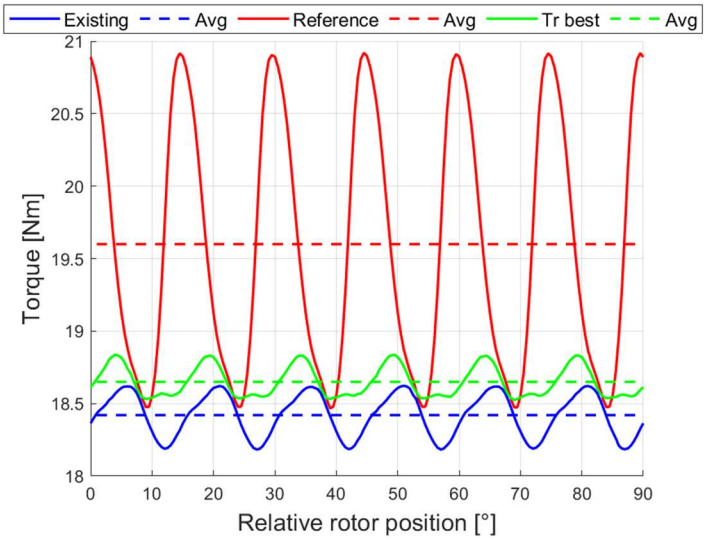

Fig. 57. Torque trend comparison among the optimal, existing and reference machines with their respective mean values.

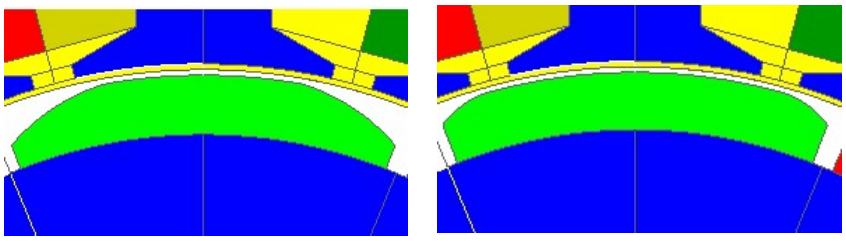

a) b)

Fig. 58. a) "T_r best" design. b) "T_{avg}" design.

Table XIX

BEST, WORST, EXISTING AND REFERENCE SOLUTION COMPARISON

	P1 [°]	**P2 [mm]**	**P3 [°]**	**T_{avg} [Nm]**	**T_r [%]**
Existing	38.75	2.4	18	18.42	2.33
Reference	38.75	4.2	38.75	19.63	12.43
T_{avg} best	42.50	3.0	32	19.90	13.55
T_r best	42.50	1.8	20	18.64	1.63

The above multi-parametric investigation has proven that the existing design performs rather similarly to the optimal design, at least in terms of average value and ripple of the output torque. However, so far, only the PMs shape is investigated, while one of the main objectives of this work is to investigate the effects of using asymmetric poles in combination with pole shaping techniques. Eventually, this will lead to a further improvement of the motor performance, while maintaining the same structural simplicity.

5.1.4 Asymmetric Poles

The effect of implementing asymmetric pole structures on average torque and torque ripple is analysed using again the 2D FE model developed in Altair Flux. An initial analysis is carried out on the existing machine, by introducing two additional geometrical parameters, and then repeated onto the reference design.

A. Asymmetric Pole Parametrization

The FE-model is modified by adding two more parameters, named D1 and D2, which indicate the variation of the position of the magnets within each pole pitch of a pole pair, with respect to the central location (see Fig. 59). D1 and D2 are changed separately, thus no longer meeting the odd symmetric scenarios considered so far. The variation range and the step for D1 and D2 are reported in Table XX.

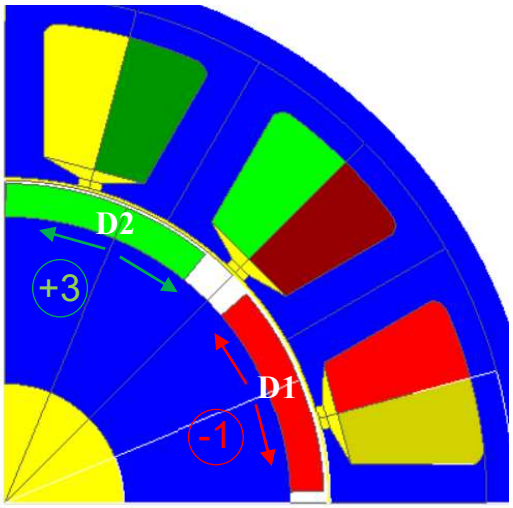

Fig. 59. Asymmetry's parameters – D1 and D2.

Table XX
PARAMETERS' VARIATION RANGE AND STEP VALUE

Parameter	**Range**	**Step value**
D1 [°]	-3 ÷ 3	0.5
D2 [°]	-3 ÷ 3	0.5

B. Results

Considering the parametrization presented in the previous subsection, the relevant FE results are shown in the 4-D plots of Fig. 60 and Fig. 61. In both figure, the torque ripple is on the z-axis, the colour scale indicates the average torque, while D1 and D2 are on the x- and y-axis respectively.

Referring to the investigation on the existing design (see Fig. 60), the point with minimum torque ripple (1.19%) is highlighted and shows a reduction of 4.89% compared to the existing design with symmetric poles.

Referring to the reference machine (see Fig. 61), compared to the reference shape, the maximum possible improvement in torque ripple is 7.56% with a worsening in average torque by 3.48 %. The results are summarized in Table XXI.

Table XXI

PERCENTAGE VARIATION OF T_{AVG} AND T_R DUE TO THE ASYMMETRY

	T_{avg} [Nm]	**T_{avg} Variation [%]**	**T_r [%]**	**T_r Variation [%]**
Existing	18.42		2.33	
Existing + pole shift	18.06	- 1.95	1.19	-4.89
Reference	19.63		12.43	
Reference +pole shift	18.95	- 3.48	11.49	-7.56

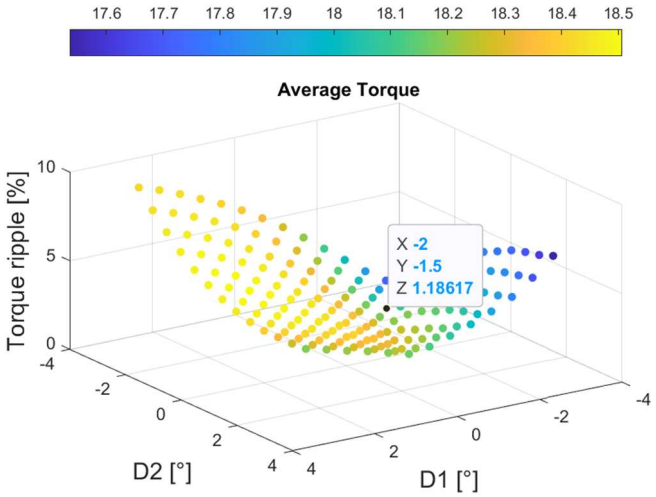

Fig. 60. Torque ripple and average torque as function of D1 and D2 in the existing machine design.

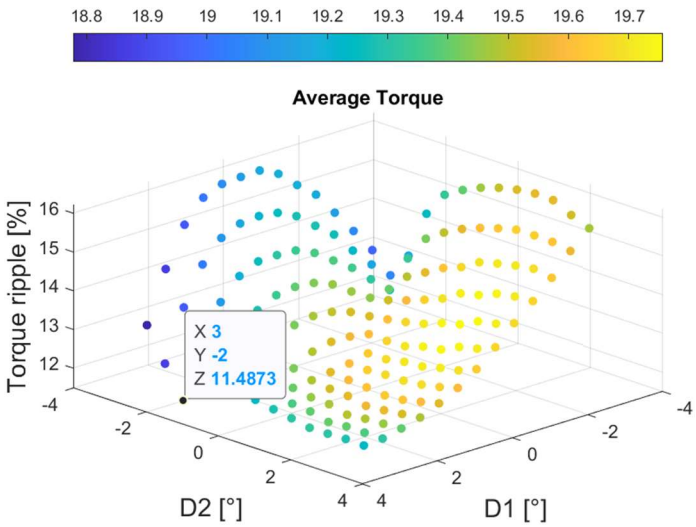

Fig. 61. Torque ripple and average torque as function of D1 and D2 in the reference machine design.

5.1.5 Final Analyses and Considerations

The previous section has proven that the combination of specific magnets' shapes and the asymmetries, generated by their decentralization respect to their standard central location, can lead to a substantial reduction of the torque ripple. However, by critically analyzing the results, other important considerations can be derived as follow:

1. By looking at Fig. 62, where the results seen in Fig. 60 and Fig. 61 are superimposed, it can be observed that the points' distributions are different. In particular, the interesting areas in terms of torque ripple and average torque fall in different positions on the D1-D2 plane, and so with different asymmetry degrees. This means that the best position for the torque ripple reduction depends on the magnet shape.
2. Another observation can be inferred by reading the data reported in Table XXI. The comparison has been done considering their respective best positions (D1 and D2) in terms of torque ripple reduction. Thus, the magnitude of the maximum possible improvement depends on the magnet shape, again.
3. By considering the first two considerations, it is possible to affirm that particular PMs' shapes can be interesting in other positions than the original ones.
4. The direct consequence of all the above is that an optimal combination of PMs' shape and asymmetry can be found.

With the aim to further confirm this, a multi-parametric 2D FE simulation is run using the parameters' settings summarized in Table XXII. To reduce the computational time, D2 is not modified and kept equal to 0.

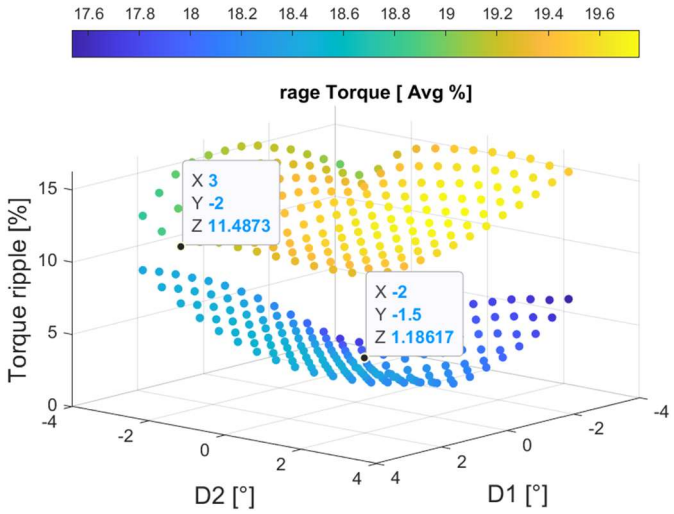

Fig. 62. Reference shape vs existing shape. Comparison of torque ripple and average torque as function of D1 and D2. Focus on the points with minimum torque ripple.

The results of four of the top configurations (namely 1-Asym, 2-Asym, 3-Asym and 4-Asym) are compared with the corresponding cases without asymmetry (namely 1, 2, 3 and 4) in Table XXIII. By analyzing the results, it is clear that the advantages in torque ripple reduction can be considerable: the highest improvement is registered for the case 3-Asym, which achieves 85,75% ripple reduction compared to its symmetric counterpart.

Table XXII
PARAMETER RANGE AND STEP VALUE

Parameter	**Range**	**Step value**
P1 [°]	33.75 ÷ 38.75	1.25
P2 [mm]	0.9 ÷ 3	0.3
P3 [°]	8 ÷ 32	2
D1[°]	-3÷3	0.5

Table XXIII
TORQUE RIPPLE VARIATION COMPARISON OF FOUR CONFIGURATIONS WITH AND WITHOUT ASYMMETRY.

	P1 [°]	P2 [mm]	P3 [°]	D1 [°]	Tr [%]
1	38.75	1.2	12	0	**7.29**
1-Asym	38.75	1.2	12	-2	**1.20**
2	38.75	0.9	12	0	**8.24**
2-Asym	38.75	0.9	12	-2	**1.31**
3	36.25	1.2	12	0	**9.97**
3-Asym	36.25	1.2	12	-2.5	**1.42**
4	33.75	1.8	10	0	**9.48**
4-Asym	33.75	1.8	10	-2.5	**1.69**

5.1.6 Conclusions

This first part of Chapter 5 proposes an investigation on the effects of combining PM shaping and asymmetries on the torque ripple reduction and average torque in a SPM machine designed for a racing car application.

The first part of this work dealt with the analysis of the machine, characterized by a customized shape of the PMs. 2D-FE models were developed and properly parametrized to reproduce the existing machine and compare it against other alternatives. The comparative results showed that the existing machine was one of the optimal solutions, with a low torque ripple being achieved.

In the second part of the work, the effects of placing PMs asymmetrically with respect to their natural central location within the pole pitch were investigated. The existing design showed a maximum possible benefit on torque ripple reduction of 4.89%, with a negligible reduction of the average torque.

Finally, the combination of both these techniques, which are typically exploited separately in SPM machines, showed indeed further performance improvements, with an overall torque ripple reduction greater than 90%.

5.2 RE Materials Reduction in a Hypercar Propulsion System

5.2.1 Introduction

This sub-chapter addresses the adaptation of an IPM propulsion motor, originally designed for the rear axle of a hypercar, for use in the front axle. By optimizing

the motor's design, specifically by reducing its reliance on RE PMs, the goal is to align performance improvements with environmental sustainability, as per thesis' objectives.

The approach focuses on investigating motor configurations that remove two or more RE PMs, replacing them with ferrite PMs, a more environmentally benign and abundant material. This adaptation maintains the high-performance demands expected in hypercars, while significantly minimizing environmental impact.

Key objectives of this research include:

- Reducing or eliminating RE materials in the motor design without compromising performance.
- Replacing removed magnets with ferrite PMs to evaluate their impact on motor torque, efficiency, and thermal behavior.
- Minimizing torque ripple and ensuring the motor meets the required performance characteristics in terms of voltage control and operational efficiency.
- Conducting structural and vibrational analyses to ensure the motor's mechanical integrity, especially under high-performance conditions.

By reconfiguring the length and arrangement of magnets and implementing design optimizations, the study ensures that the motor meets the necessary performance standards while contributing to the broader goal of reducing the automotive industry's reliance on RE materials. Finally, rigorous tests are performed to validate the motor's robustness and operational reliability, ensuring that the design remains competitive with traditional RE-based solutions.

5.2.2 Benchmark machine and FE model Description

In this section, the geometrical, electrical and performance information of the benchmark machine are presented (see Table XXIV). Then, its electromagnetic model set-up is described. At the end, the front axle performance requirements are tabulated and compared with the rear axle data (see Table XXV).

A. Rear Axle Motor

A six-poles high-performance IPM motor, designed for the rear axle of a hypercar, is the benchmark machine of this work. Its main geometrical and electrical parameters are summarised in Table XXIV, whereas its performance are reported in Table XXV. One pole-pitch of the 2D FE model of the machine is reported in

Fig. 63. A three-phase hairpin winding system is hosted by a 54 slots stator, whereas six brick-type PMs are arranged to realise a two-barriers rotor. Stator and rotor laminations are made of silicon steel named NO20_1200, while N48H NdFeB magnets are housed in the rotor. This configuration provides an output rated torque of 340 Nm from 0 to 8200 rpm, while the maximum speed is 20000 rpm. A brief overview of the FE model details is given in the next subsection.

B. FE Model Overview

The 2D FE model is built in Altair Flux exploiting all symmetries to reduce the computational time. Given the hairpin winding arrangement, one pole pair is the base unit, due to the necessary layer shift for balancing impedances of the two parallel paths (i.e. P1 and P2, see Fig. 64). For the sake of simplicity, only one pole pitch is reported in Fig. 63. In Fig. 64 the FE-coupled electric circuit is schematised. A star-connected three-phase hairpin winding is supplied by a three-phase set of sinusoidal currents. Only two current generators (Gen.) are used in the circuit to avoid over-determining the system. As depicted in Fig. 64, every single pin in the pole pair is modelled as "solid conductor" to take skin and proximity effects into account, while the white elements belong to the adjacent pole, which is not shown in Fig. 63. For the sake of clarity colour match is adopted between Fig. 63 and Fig. 64. To accurately estimate the machine performance, the end-winding are considered and modelled through additional resistances and inductances ("End W." in Fig. 64).

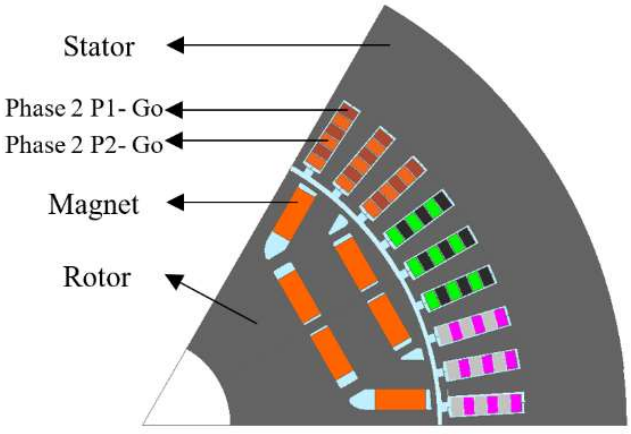

Fig. 63. 2D FE Model of a pole pitch of the starting machine.

C. Rear Axle Performance Requirements

The previously presented FE model is used and properly modified to create and compare different configurations in order to match the front axle requirements. Stator and rotor geometries are kept fixed as well as the winding structure to minimise time and production costs. The degrees of freedom involve the stack length, number, type and magnets arrangement. A 180 Nm output torque is required, with the maximum possible reduction in RE materials usage, as well as minimum amount of modifications compared to the rear axle motors. Torque ripple, base speed, efficiency, maximum speed and RE PMs weight requirements are reported in Table XXV.

Table XXIV
MOTOR PARAMETERS

Parameter	**Value**	**Parameter**	**Value**
Inner rotor diameter	35 mm	Number of magnets	36
Outer rotor diameter	120 mm	Conductor type	Hairpin
Outer stator diameter	195 mm	Slot number	54
Pole pairs	3	Phase number	3
Air gap thickness	1 mm	Parallel paths	2
N. magnet layers	2	Pins per slot	6
Stack length	125 mm	DC voltage	820 V

Table XXV
MOTORS PERFORMANCE: COMPARISON BETWEEN REAR AND FRONT AXLE MOTORS

Metric	**Rear**	**Front (Requirements)**
Torque	340 Nm	180 Nm
Torque Ripple	10 %	≤ 10 %
Base Speed	8200 rpm	≈ 8200 rpm
Efficiency @ 8200 rpm	90 %	Maximize
NdFeB Weight	2,36 kg	≤ 1,23 kg
Maximum Speed	20000 rpm	20000 rpm

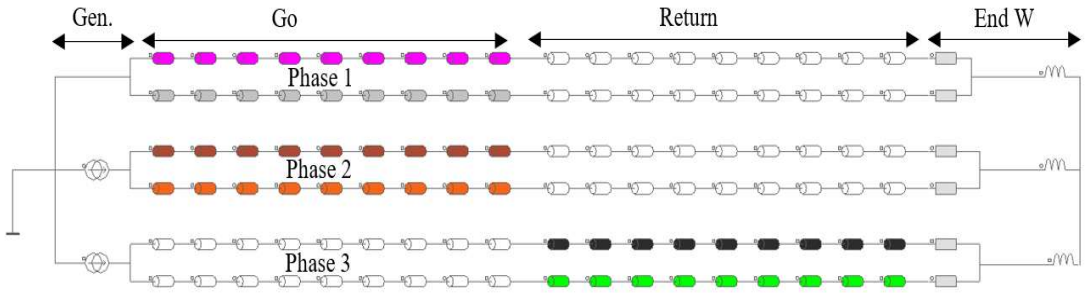

Fig. 64. 2D FE-coupled electric circuit. “Gen” are the two generators, “Go” and “Return” are the active side with outgoing and ingoing currents and “End W” are the end-windings resistances and inductances.

5.2.3 Configurations comparison

To obtain new configurations with fixed laminations design, changes in the axial length, number of magnets and PMs arrangement are made. Two, three and four PMs are removed from different rotor slots in each pole pair. Initially, the resulting empty slots are left vacant and the relative solutions are analysed and compared in subsection 5.2.3.A. Then, the empty slots are filled with C8 Ferrite PMs and the performance of this new set of machines are compared in subsection 5.2.3.B. The best configurations of both the sets are compared and commented in subsection 5.2.3.C.

A. Set A – Non-Ferrite Arrangments

Both the sets of configurations are compared at 180 Nm, that is the front axle requirement. Basically, once defined the magnets arrangement, the axial length of each configuration is properly modified to achieve the rated torque. Then, the other electromagnetic outputs and the weight of the NdFeB PMs are displayed and compared for all the different proposals with respect to the requirements. The reference weight of NdFeB PMs is that needed to reach 180 Nm with the starting arrangement, i.e. the one with six NdFeB magnets per pole (Config. 1A, see Fig. 65). Fig. 65 shows the adopted nomenclature for the PMs under the pole-pair under study. Fig. 66 reports the remaining 12 arrangements (2A-13A). The FE results are reported in Fig. 67 and expressed in p.u. The base quantities are 10% for the torque ripple (Tr_base), 8200 rpm for the base speed (Ωb_base), and 90% for the efficiency (Eff_base). On the other hand, for the RE PMs weight, the reference values are the weights of each configuration (namely REMW_XXA), in order to highlight the eventual reductions against Config. 1A. The remarkable solutions for this set are the 9A, 10A and 12A. Solution 9A is considered because of its low

torque ripple and higher reduction of RE PMs weight compared to the 1A-8A configurations.

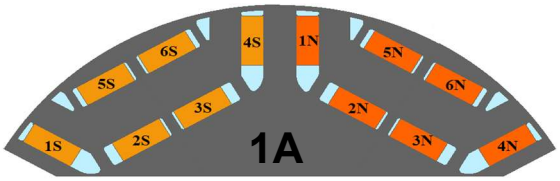

Fig. 65. Rotor slots and relative magnets names. Example of Config. 1A.

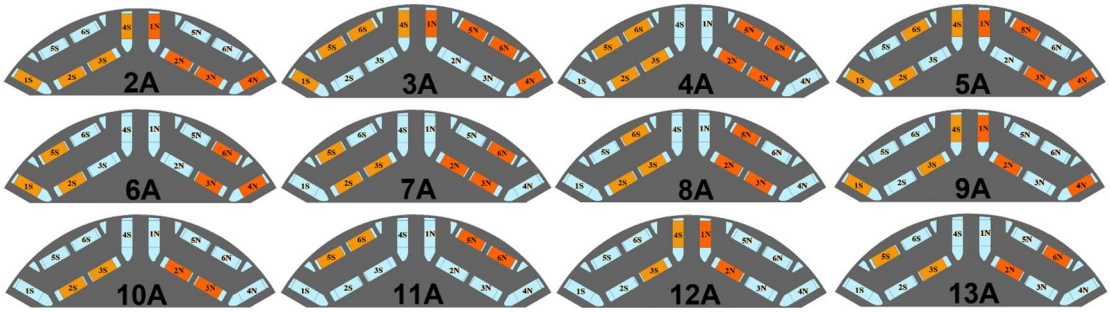

Fig. 66. Results comparison in p.u. of the 1st set of machines. Base speed in blue, torque ripple in grey, weight of RE magnets in black, and efficiency in green.

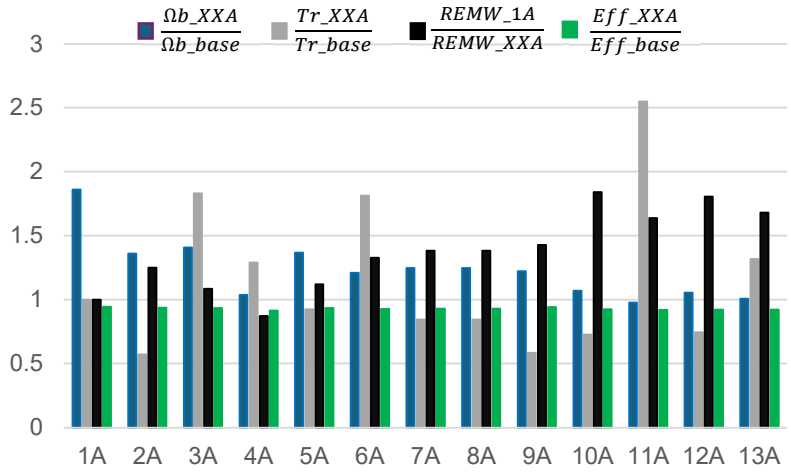

Fig. 67. Results comparison in p.u. of the 1st set of machines. Base speed in blue, torque ripple in grey, weight of RE magnets in black, and efficiency in green.

B. Set B – Hybrid Arrangments

The second set of machines (2B-13B) is realized by filling the empty slots of the first set (2A-13A) with C8 Ferrite. Configuration 1B is instead the counterpart of 1A in which all the NdFeB PMs are replaced by C8 Ferrite. The results comparison among the "B" configurations are reported in Fig. 68. The reference NdFeB PMs weight remains the same as Config. 1A. The remarkable solutions are 9B, 10B and 12B, which are commented in the next subsection. Despite the total absence of RE PMs in configuration 1B, this is not considered as a good solution as the voltage

limit is overcome, as highlighted in Fig. 68 (see the grey bar in correspondence of configuration 1B which is higher than 1 p.u.).

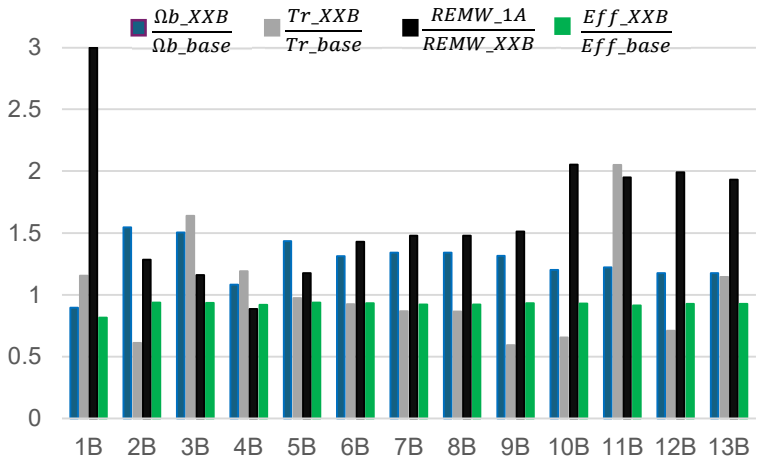

Fig. 68. Results comparison in p.u. of the 2nd set of machines. Base speed in blue, torque ripple in grey, weight of RE magnets in black, and efficiency in green.

C. Comparison among the selected remarkable configurations

The performance metrics of the most interesting configurations are summarized in Table XXVI. As expected, all these show lower efficiency levels against the benchmark one. The worsening is due to the lower ratio between the active and end-windings lengths. In fact, this latter has been kept constant in all the tested configurations, resulting in higher weight on the total joule losses for the shortest machines. However, the reduction in efficiency is significantly lower during highway (≃ 2%) or city routes (≃ 4%) operations. Although solutions 9A and 9B could be already abandoned at this stage because of their higher base speed and RE PMs weight than the corresponding requirements, the final decision goes through the results of the structural, vibrational and demagnetization analyses, which are the focus of the next section.

Table XXVI
REMARKABLE SOLUTIONS

Outputs comparison: remarkable solutions						
Output	***9A***	***9B***	***10A***	***10B***	***12A***	***12B***
Torque (Nm)	180	180	180	180	180	180
Torque Ripple (%)	5.8	5.9	6.6	7.3	7.4	7.7
Base Speed (rpm)	10440	10775	8766	9844	8653	9633
Eff. @8.2 krpm(%)	84.1	83.9	83.1	83.6	83.0	83.5

Outputs comparison: remarkable solutions						
Output	***9A***	***9B***	***10A***	***10B***	***12A***	***12B***
NdFeB weight (kg)	0.86	0.81	0.67	0.59	0.68	0.62

5.2.4 Structural, Vibrational and Demagnetization Analyses

A. Structural Analysis

The six remarkable configurations (9A, 9B, 10A, 10B, 12A, 12B) are subjected to structural analyses in order to verify the structural integrity at the maximum speed (20000 rpm). Their von Mises stress is evaluated and compared with the reference machine to highlight eventual advantages. The tensional state evaluations on the rotor laminations are carried out employing the commercial FE software MSC Marc Mentat 2020.1. The non-linearities of the analysis are exclusively due to the contact between the magnets and their respective slots. A plane strain modelling is adopted [75], imposing a domain thickness coincident with that of the single rotor lamination (i.e. 0.20 mm). All possible planes of symmetry are used for the rotor modelling. Thus, in case of pole symmetry (e.g. configuration 10A) the domain extent could be limited to only 1/12 of the whole rotor. Despite this, the extended domain (i.e. 1/6) is adopted for all configurations in order to simplify the comparison. The mesh employed for the only rotor lamination consists of about 485000 elements, 4 linear QUAD4 nodes, while the single magnet is discretized with about 17000 elements. The average size for both components is 0.05 mm. The material properties associated with the rotor laminations and magnets are given in Table XXVII.

The contacts between magnets and their relative slots are modelled by a frictional and unilateral contact, employing a friction equal to 0.4 [76]. The tangential forces exchanged at the contact edge are thus higher eliminating the lability of the central magnets and allowing the calculation to converge. Without a suitable value of the friction coefficient, in fact, the absence of the sealing teeth of the central magnets would cause the magnet slippage along the axis of their respective slots. Such teeth are present in the real motor, but they are neglected in the FE model because they are not interesting from a tensional and electromagnetic point of view.

The imposed boundary conditions are symmetry at the α and β planes of Fig. 69 and maximum angular speed (20000 rpm). The coupling of the rotor laminations

and shaft is not realized by interference, so no boundary condition is implemented on their coupling edge. Fig. 69 highlights the stress state of the starting configuration. The most stressed bridges are those belonging to the layer radially closest to the shaft. The is related to the greater inertial force experienced by the lower bridges with respect to the upper ones. The main stress characteristics acting on these bridges are the normal stress in A and a combination of normal stress and bending moment in B and C, see Fig. 69. The stress peaks occur at the radii of the slots in which the magnets are housed. The maximum calculated stress is 410 MPa, the static safety coefficient of the design configuration is about 1.08, obtained as the ratio of the yield stress of the material to the maximum calculated one.

Fig. 70 and Fig. 71 show the von Mises equivalent stress distribution of the three remarkable configurations of set A and set B, respectively. A reduction of ≈17% of the maximum stress and a consequent increase in the static safety coefficient up to 1.30 is observed in configuration 9A. The lower density of the Ferrite C8 PMs than the N48H PMs causes a lower overall inertial action, resulting in a reduction of peak tension of ≈7%. Fig. 70 also highlights how the removal of a magnet does not always lead to a natural reduction in peak tension, with configurations 9 and 12 being an example. Despite the reduced eccentric mass and, thus, overall inertial force acting on the rotor, the maximum von Mises stress of configuration 12A is ≈3.6% higher than that of configuration 9A. This is because the adding of magnet 4N partially compensates the bending moment produced by magnets 1N and 2N, thus decreasing the resultant force arm.

Table XXVII
MATERIALS STRUCTURAL PROPERTIES

Parameter	**NO_20_1200**	**N48H**	**C8 Ferrite**
Density [kg/m^3]	7600	7650	4800
Young's Modulus [MPa]	185000	154000	180000
Poisson's Ratio	0.3	0.24	0.28
Yield tensile strength [MPa]	445	-	-
Ultimate tensile st. [MPa]	535	-	-
Elongation at break [%]	17	-	-

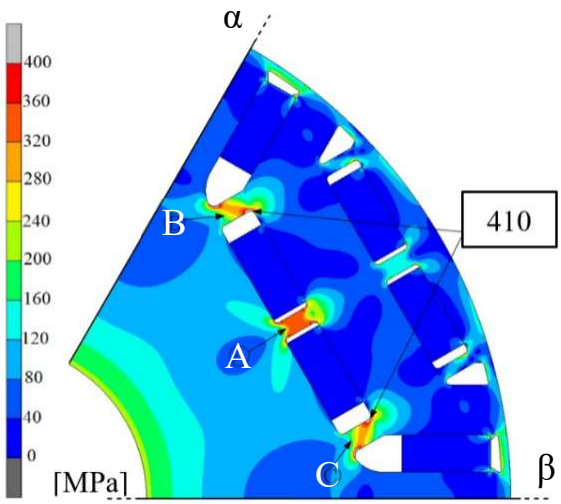

Fig. 69. Contour plot of von Mises equivalent stress for the starting configuration and identification of symmetry planes (α, β).

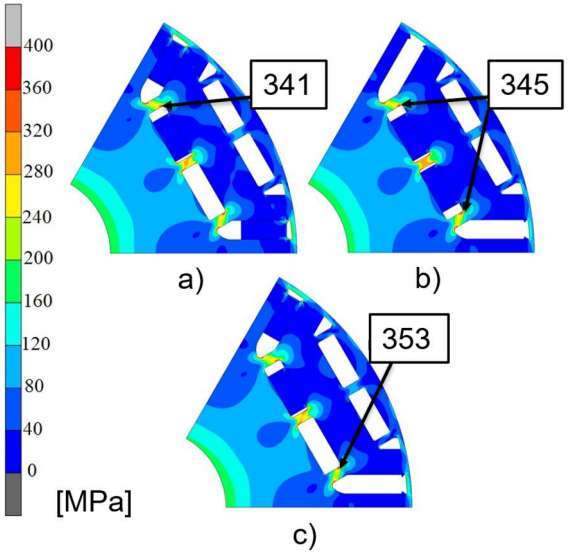

Fig. 70. Contour plot of von Mises equivalent stress for configurations a) 9A, b) 10A and c) 12A.

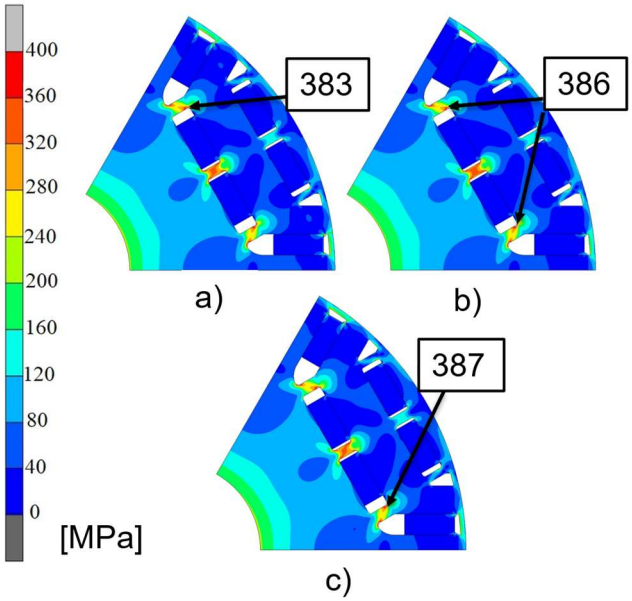

Fig. 71. Contour plot of von Mises equivalent stress for configurations 9B (a), 10B (b) and 12B (c).

B. Vibrational Considerations

In this study, only the centrifugal forces acting on the magnets during the rotation are considered and applied to their center of mass, i.e. the geometrical central points, see Fig. 72. Arrangements in which the vector sum of the centrifugal forces are null and so, equation (18) is satisfied, are expected.

$$\sum_{i=1}^{n} m_i \, \omega^2 r_i \, sin\,(\omega\, t + \varphi_i) = 0 \qquad (18)$$

In (18), m_i is the mass, ω is the angular speed, t is the time, r_i and φ_i are the radial and angular position, respectively, of the i-th magnet (Fig. 72). All the considered configurations (9A, 9B, 10A, 10B, 12A and 12B), are perfectly balanced because the magnets groups realise mass centers shifted by 120 mechanical degrees among themselves. Thus, no further vibrations are led to the system by the magnets arrangements.

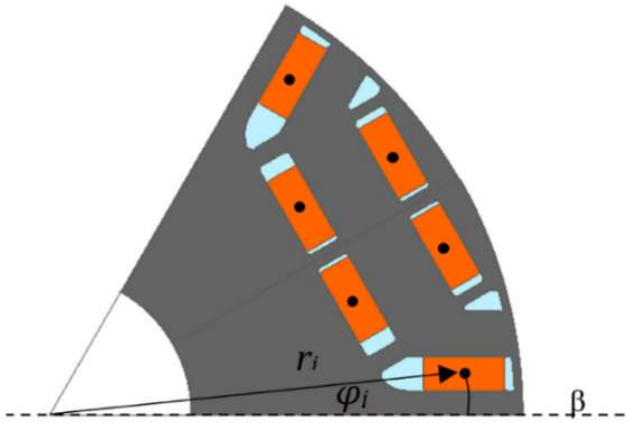

Fig. 72. Example of center of mass, radial position r_i and angular position φ_i of the i-th magnet.

C. Demagnetization test

Ferrite C8 PMs exhibit the knee point of the B-H curve in the 2nd quadrant for values of temperature lower than 100°C, showing performance improvements with increasing temperature, unlike NdFeB PMs [77], [78]. This feature makes them sensitive to demagnetization at the lowest temperatures, e.g. at cold starting of the machine. Demagnetization checks are therefore necessary. To this purpose, FE simulations at 0° Celsius and maximum torque are run. Relevant demagnetized areas are detected for all the promising configurations at cold start. In Fig. 73 the flux density field map is reported for the configuration 10B at that operating point. Demagnetization issues disappear when the motor is warmed-up, i.e. at temperatures higher than 60°C, thus the relevant flux density maps are not reported.

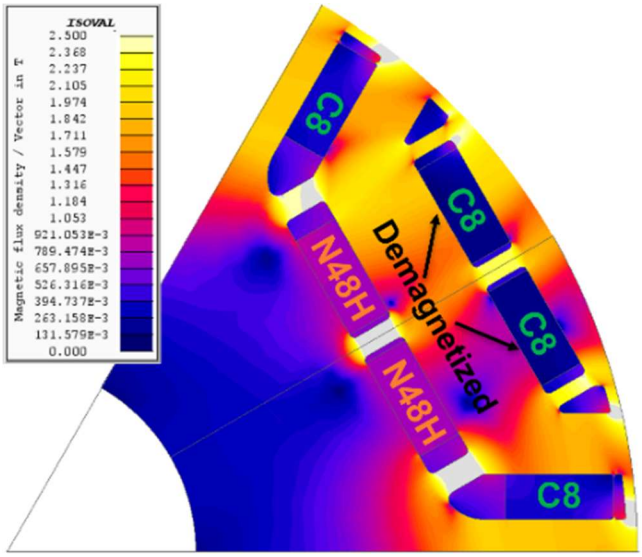

Fig. 73. Flux density map at 0°C of configuration 10B. Demagnetization areas detection.

5.2.5 Final Considerations and Machine Selection

The previous sections discussed the electromagnetic, structural and vibrational behaviour of different possible configurations for the IPM motor taken as case study. Considering the overall results, it is possible to draw a number of considerations:

- The arrangements with the minimum number of RE PMs are those with the best magnet weight exploitation.
- The magnets removal averagely leads to an improvement of the rotor tensile stress state, thanks to a reduction of the centrifugal forces.
- The tensile stress state is also a function of the PMs relative positions, as highlighted in configurations 9A and 12A.
- Magnet arrangements presenting symmetry with respect to a pole pair do not introduce further vibrational challenges.
- Hybrid magnet arrangements, i.e. 2B-13B, can lead to a further RE PMs reduction, but demagnetization can arise if the motor is not properly warmed-up.
- The decreases in torque density and efficiency are fully compensated by high reduction in production times and costs of the propulsion system.

Hence, in light of all these results, the configurations 10A and 12A (see Fig. 66) are appointed as best design solutions.

In fact, despite the additional RE PMs reduction achieved by solutions 10B and 12B against 10A and 12A, the latter perform better in terms of torque ripple and base speed, but most importantly there is no risk of demagnetization.

Furthermore, it should be kept in mind that all materials are subjected to the costs market fluctuations. In this sense, non-Ferrite arrangements are preferred to hybrid solutions, where more than one PM type are used.

5.2.6 Conclusions

This second part of Chapter 5 dealt with the reduction of RE PMs total weight in a propulsion system of a hypercar, which involves IPM hairpin motors. With the rear axle motors already selected and analysed, it was deemed effective considering their design as a starting point to select the front axle motors. A design constraint was to keep the same lamination design as the rear axle motor, but stack length and PMs arrangements could be modified to meet the requirements. The

main design objective was to reduce the RE amount, thus matching the ever-more stringent sustainability requirements demanded nowadays by automotive applications.

Two sets of configurations are investigated. The first set (namely set A), was obtained by removing 2, 3 and 4 magnets from their locations in the rotor slots. In set B the resultant empty slots of set A were filled with Ferrite PMs. The metrics under analysis were torque, torque ripple, base speed, efficiency and weight of RE PMs. The most promising arrangements were analysed via FE structural investigations, as well as via basic analytical vibrational considerations. Finally, demagnetization tests were also performed.

The selected best solutions (10A and 12A) achieved very good performance with all the requirements being met. Significant reductions by 45.5% and 44.7% in RE PMs weight respectively for 10A and 12A were obtained, as well as 15.8% and 13.9 % decreases of the von Mises stress against the benchmark rear axle layout were detected.

5.2.7 Chapter's Closing Remarks

This chapter has demonstrated that reducing RE materials in propulsion systems is not only feasible but also beneficial in high-performance automotive applications.

The results underline the potential for further innovation in sustainable propulsion technologies, with broader applications beyond the hypercar sector. As the automotive industry moves toward greener solutions, these findings offer a foundation for future developments in RE-free motor designs.

In the next chapter, case studies from the off-highway sector will demonstrate how these innovations can be practically applied also in demanding environments, further showcasing their versatility and potential impact across various industries.

6. Case Study: Rare Earth Reduction in Off-Highway vehicles

6.1. Wound Rotor Synchronous Motor Design for a Mining Application [4]

6.1.1 Introduction

This section presents the electromagnetic design process for a WRSM intended for a mining truck (Fig. 74), aiming to replace the current IPM motor. The primary objectives are minimizing disruption to the system, reducing costs, and maintaining simplicity. The new WRSM design must replicate the torque-speed characteristics of the existing IPM motor using the same housing and cooling systems. Key design requirements include torque output, efficiency, size, temperature control, excitation system power, and structural durability at maximum speed.

A comprehensive design process is followed, starting with an analysis of the IPM motor's performance. The WRSM design is then parameterized and optimized to meet the required specifications. Both electromagnetic and structural factors are considered from the outset to ensure thermal and structural integrity. An iterative optimization process yields three candidate configurations, each validated through static and dynamic thermal tests to ensure compatibility with insulation class and overload capacity.

Finally, the WRSM is confirmed as a potential replacement for the IPM motor. Although the excitation system design is not included at this stage, the structural analysis demonstrates that the WRSM meets the necessary performance and durability standards.

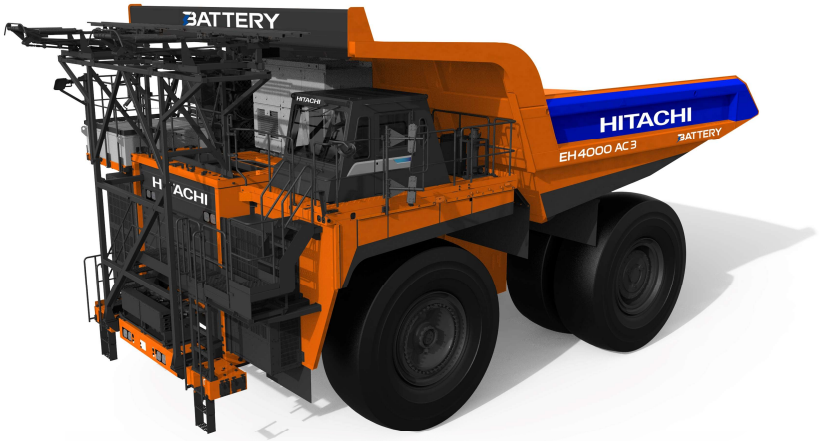

Fig. 74. Example of a mining truck.

6.1.2 Reference Performance For the WRSM

This section delineates the performance metrics of the existing IPM machine, outlining the dimensional and thermal restrictions dictated by the current housing and cooling system. These constraints are set to be unaltered in the forthcoming design iteration. Additionally, the narrative encompasses the strategic design decisions made for the WRSM, aligning with both the aforementioned constraints and considerations of economic viability and construction simplicity.

A. Performance of the IPM Existing Motor

The IPM motor exhibits a nominal torque output of 1500 Nm, with a peak torque reaching 3330 Nm during transient operations. In particular, the motor attains a maximum speed of 3240 rpm, and a base one of 1250 rpm. Housed within a casing featuring an internal diameter of D mm and a length of L mm, the motor relies on a liquid cooling system with an inlet fluid temperature set at 65°C. The machine insulation class is H, ensuring a maximum allowable temperature of 180 °C. These recorded parameters serve as foundational design data for the ensuing WRSM design. (Some numerical values are missing due to confidential agreements with the industrial partner).

B. Further Requirements and Choices for the WRSM

Cost reduction and construction simplicity, coupled with factors such as the cooling system, overall size, and the required thermal overload (elaborated upon

in 6.1.5), guide specific decisions concerning conductor type, stator, and rotor current densities.

To address AC effects and enhance the fill factor, the stator windings incorporate strands having a cross-section of 1.06 mm. Under nominal conditions, current density limits of 10 A_{RMS}/mm^2 and 4 A_{RMS}/mm^2 are imposed on the stator and rotor conductors, respectively. In order to ensure the use of low-cost laminations for the stator and rotor cores, the maximum electrical frequency is limited at 350 Hz. The adopted lamination for both the stator and rotor is then M350 50A, with a thickness of 0.5 mm. The air-gap size is restricted to a minimum of 1 mm. An upper limit is set on the excitation system power and torque ripple, not to exceed 5 kW and 10%, respectively.

Table XXVIII succinctly summarises the outlined requirements and constraints for the WRSM. The next section delves into the geometry and performance of the initial WRSM, subsequently subjected to modifications.

Table XXVIII
WRSM REQUIREMENTS AND CONSTRAINTS

Parameter	**Value**	**Parameter**	**Value**
Rated Torque [Nm]	1500	Stator External Diameter [mm]	D
Rated Base Speed [rpm]	≥ 1250	Active Length [mm]	≤ A_L
Maximum Speed [rpm]	3240	Maximum Line Voltage [V_{rms}]	500
Overload Torque [Nm]	3330	Rated Current [A_{RMS}]	315
Overload Base Speed [Nm]	≥ 1250	Maximum Current [A_{RMS}]	681
Housing Length [mm]	L	Rated Rotor Current Density [A_{RMS}/mm2]	≤ 4
Nominal Stator Current Density [A_{RMS}/mm^2]	≤ 10	Lamination Thickness [mm]	0.5
Lamination Type	M350 50A	Maximum Excitation Power [kW]	≤ 5

Parameter	Value	Parameter	Value
Admissible Electrical Frequency [Hz]	≤ 350	Efficiency @ Base Speed [%] Nominal	≥ 95
Minimum Air-gap Thickness [mm]	1	Efficiency @ Base Speed [%] Maximum	≥ 91
Torque ripple @ 1500 Nm, 1250 rpm [%]	≤ 10	Torque ripple @ 3330 Nm, 1250 rpm [%]	≤ 10
Time in overload (from 1500Nm-1250rpm to 3330Nm-1250rpm) [s]	> 120	Active Weight [Kg]	≤ A_W

6.1.3 Starting WRSM and FE Model Details

In light of the extensive constraints and requirements detailed in the preceding section, a series of configurations is explored, characterized by varying geometries, winding distributions, polar pairs number, and rotor turns number. The configuration that aligns most closely with the design requirements is selected as the initial motor for subsequent adjustments, parameterization, and optimization. For simplicity, this chosen model is denoted as Configuration 0.

Configuration 0 features 4 pole pairs, 72 stator slots, a double-layer winding with 3 slots per pole per phase, short-pitched by 1 slot for torque ripple containment, and 150 turns per rotor pole. Fig. 75, a pole pitch of the FE model of the machine is depicted. Both stator and rotor coils are represented as coil conductors, considering fill factors of 50 % and 65 %, respectively. AC losses are disregarded due to the reduced operating frequencies and conductor diameter (1.06 mm). The three-phase system is powered by purely sinusoidal current sources. Table XXIX presents some key outputs of configuration 0, highlighting critical aspects such as efficiency, stator current density, and torque ripple. Identified deficiencies prompt adjustments and appropriate parameterization as part of the optimization process. The overarching goal is to derive solutions that seamlessly align with the specified requirements.

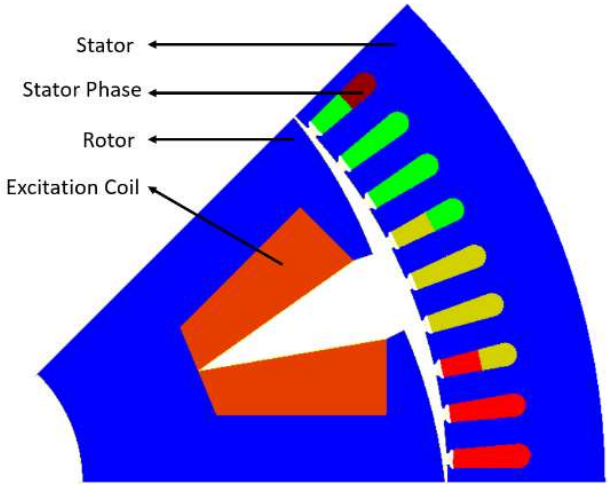

Fig. 75. 2D FE model of a pole pitch of Configuration 0.

Table XXIX
OUTPUTS OF CONFIGURATION 0

Parameter	**Value**	**Parameter**	**Value**
Rated Torque [Nm]	1500	Active Length [mm]	$0.74A_L$
Rated Base Speed [rpm]	1285	Efficiency @ Base Speed [%] Rated	89
Overalod Torque [Nm]	3330	Torque ripple [%]	12
Rated Stator Current Density [A_{RMS}/mm^2]	12.6	Rated Rotor Current Density [A_{RMS}/mm^2]	3.3

6.1.4 Parametrization and Optimization Results

In this section, the optimisation parameters are outlined, along with the presentation of the designs deemed superior from an electromagnetic performance perspective and their corresponding outputs. In accordance with the industrial partner's directives, the optimisation process is primarily focused on the nominal operating condition (1500 Nm at 1250 rpm) and the overload scenario (3330 Nm a 1250 rpm). Although a more comprehensive design approach would ideally include the full duty cycle of the machine, focusing on these critical points was deemed sufficient for this stage of the analysis.

A. Optimization Parameters

In response to the critical issues identified in Configuration 0, particularly those relevant to the efficiency values, a modified model is built for optimisation through parameterization. Fig. 76 illustrates the 2D geometric parameters crucial for the optimization process, while a comprehensive list with descriptions is provided in Table XXX. To guarantee robust structural integrity, the range of variation of the optimization parameters (named as Ox, with $1 \leq x \leq 14$) is opportunely chosen mostly according to structural considerations, which will be validated in a dedicated environment and elaborated in Section 6.1.6.

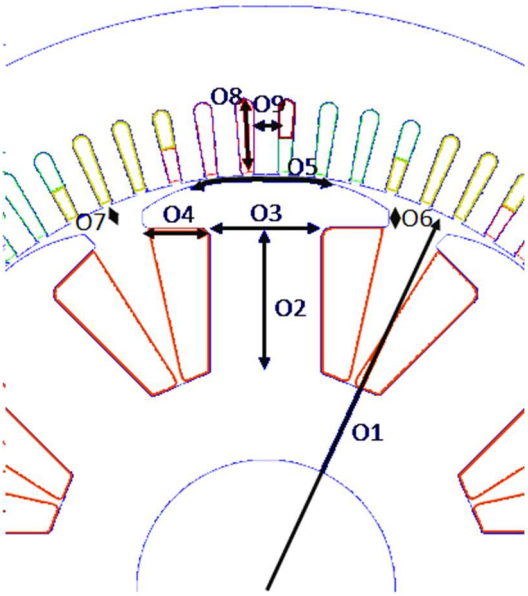

Fig. 76. 2D geometrical optimisation parameters.

Table XXX
PARAMETERS INVOLVED IN THE OPTIMIZATION

Name	**Description**	**Name**	**Description**
O1	Rotor external radius	O8	Stator slot height
O2	Rotor pole body height	O9	Stator tooth width
O3	Rotor pole width	O10	Stack length
O4	Pole tip length	O11	Rated excitation current
O5	Pole upper part angular span	O12	Number of turns of excitation coil
O6	Pole tip height	O13	Number of turns of stator windings

Name	Description	Name	Description
O7	Maximum air-gap thickness	O14	Maximum excitation current

B. Electromagnetic Optimization Results

The primary objective of the optimization process is to identify solutions which meet the established design requirements. Given the complex nature of the problem, the optimization takes place within a dedicated environment, specifically Altair Hyperstudy, a MOGA. Of several potentially viable solutions, three configurations are short-listed as most promising, and subsequently subjected to comprehensive thermal and structural analyses.

An important observation is that, while these configurations meet most design requirements, the only criterion not entirely fulfilled pertains to the basic speed of the overload characteristic (Table XXXI). Fig. 77 presents the designs of the three configurations, denoted as 1, 2, and 3, respectively. While the qualitative geometrical differences can be appreciated from the figure, a quantitative comparison cannot be made available due to confidential agreements with the industrial partner. However, Table XXXI reports their main performance metrics in relation to the specified requirements. The torque trends under nominal conditions are compared in Fig. 78, with a similar ripple being registered. Fig. 79 finally highlight Configurations 1, 2, and 3 in the Torque-Efficiency plane, emphasizing their goodness compared to the cloud of solutions analysed in the optimization process. Machines with an apparently better behaviour in the aforementioned plane do not satisfy the other constraints. It is crucial to emphasize that, while all solutions fully satisfy the design criteria except for the basic speed of the overload characteristic, Configuration 2 emerges as the most promising when focusing solely on electromagnetic performance. However, the definitive selection of the optimal candidate is deferred pending the evaluation of thermal aspects (Section 6.1.5) and structural considerations (Section 6.1.6).

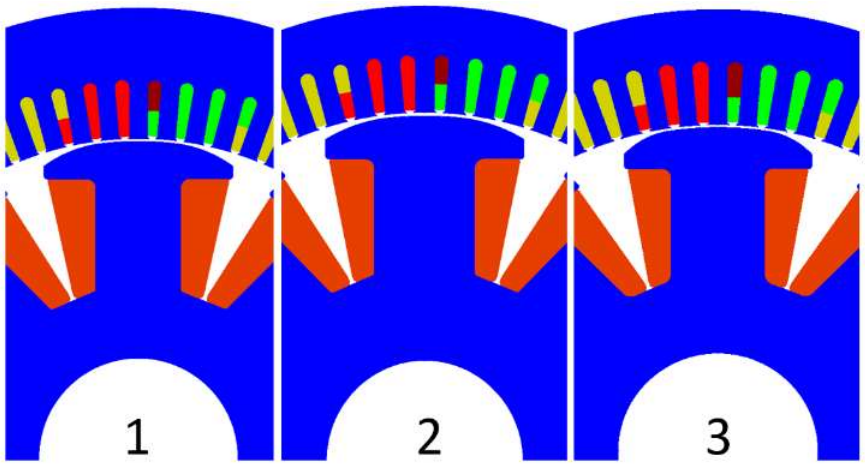

Fig. 77. 2D FE models of a pole pitch of Configurations 1,2 and 3.

Table XXXI
COMPARISON AMONG CONFIGURATIONS 1, 2 AND 3.

Outputs	**Requirements**	**C. 1**	**C. 2**	**C. 3**
Rated Torque [Nm]	**1500**	1500	1500	1500
Rated Base Speed [rpm]	≥ **1250**	1280	1422	1271
Overload Torque [Nm]	**3330**	3330	3330	3330
Overload Base Speed [Nm]	≥ **1250**	1037	1225	1050
Maximum Excitation System Power [kW]	< **5**	4.2	4.5	3.8
Effieciency @ 1250 rpm 1500 Nm [%]	≥ **95**	95.3	96.0	95.7
Efficiency @ 1250 rpm 3300 Nm [%]	≥ **91**	91.4	93.2	91.7
Torque Ripple @ 1500 Nm,1250 rpm [%]	≤ **10**	6.2	4.6	6.8
Torque Ripple @ 3330 Nm,1250 rpm [%]	≤ **10**	8.2	6.8	8.0
Rated Stator Current Density [A_{RMS}/mm^2]	≤ **10**	9.9	8.8	8.9
Rated Rotor Current Density [A_{RMS}/mm^2]	≤ **4**	3.3	3.4	3.0

Outputs	Requirements	C. 1	C. 2	C. 3
Active Weight [Kg]	≤ A_W	0.87A_W	0.96A_W	0.88A_W
Active Length [mm]	≤ A_L	0.80A_L	0.89A_L	0.81A_L

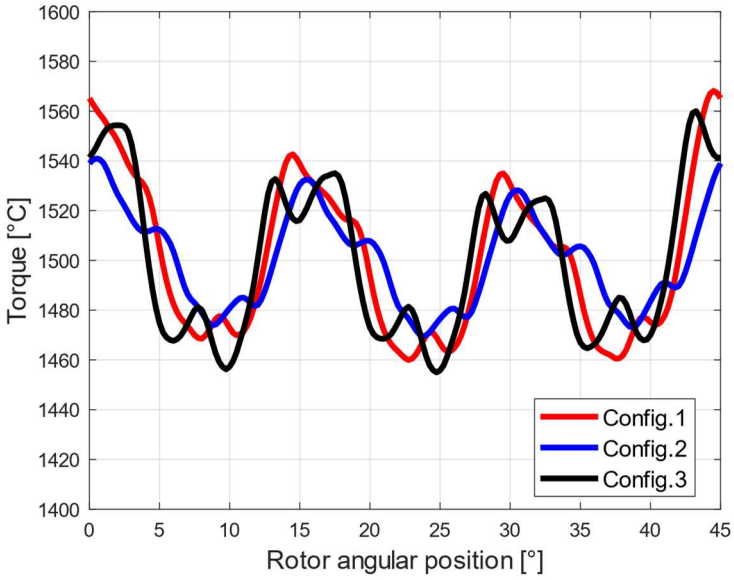

Fig. 78. Electromagnetic torque: comparison of Configurations 1,2 and 3.

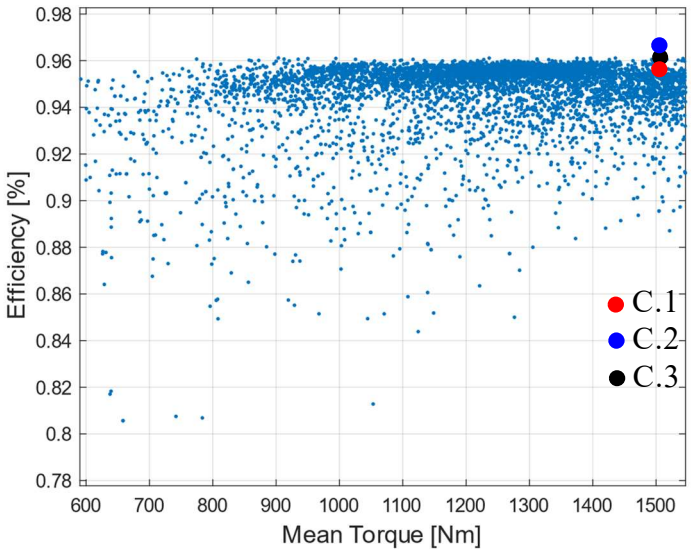

Fig. 79. Optimization process solution distribution in Mean Torque-Efficiency plan. Highlighting of Configuration 1, 2 and 3.

6.1.5 FE Thermal Model Results

In this section, the steady-state and dynamic thermal behaviour under both nominal and overload conditions of Configurations 1, 2, and 3 is scrutinized. The analysis aims to determine whether the temperature constraints imposed by the insulation system are met and to assess the dynamics of temperature variations.

The overarching goal is to pinpoint the solution that exhibits the most favourable thermal performance.

A. FE Thermal Model Description

The thermal analysis is conducted using the same FE software employed for the electromagnetic analysis, Altair Flux, through which the losses within the various active components of the motor are evaluated. To account for harmonics introduced by the electric drive, an additional 10% is incorporated imagining the worst-case scenario. The modelling of conductors within the slots is simplified by utilizing a single centrally located conductor surrounded by an equivalent layer of insulation [79]. This approach encapsulates the behaviour of both enamel and impregnation, while the slot liner is considered as standalone. These concepts are illustrated in Fig. 80 for the stator, but the same approach is envisioned for the rotor. The materials' thermal conductivities and boundary conditions draw partially from data obtained from the IPM motor and their implementation is supplemented by literature, such as [80]. Table XXXII provides a summary of some of these coefficients and conditions.

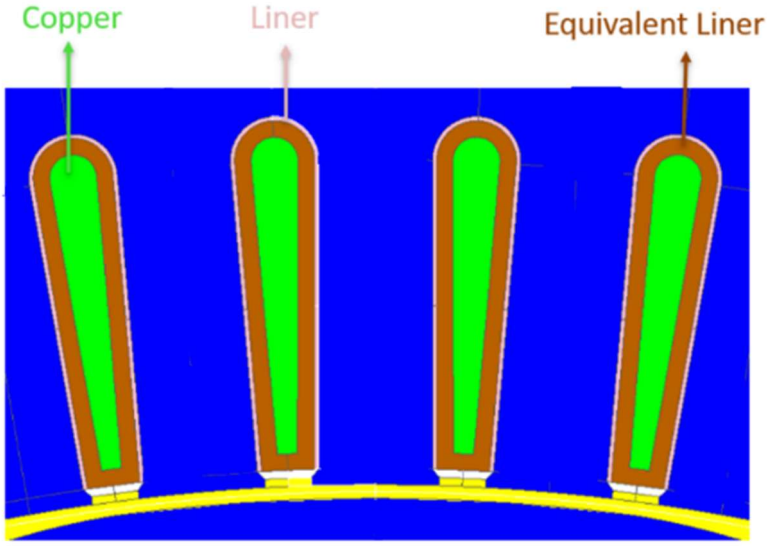

Fig. 80. 2D FE thermal model of the stator slots.

Table XXXII
THERMAL PARAMETERS

Region	Material	Thermal Coefficients
Rotor	M 350 50A	25 [W/mK]
Stator	M 350 50A	25 [W/mK]

Region	Material	Thermal Coefficients
Stator and rotor wires	Copper	384 [W/mK]
Liner	Nomex 130	0.21 [W/mK]
Equivalent Liner	Epoxy	0.35 [W/mK]
Airgap (1250 rpm - 105 °C)	Air	58 [W/m^{2}K]
Coolant	Water	400 [W/m^{2}K]

B. FE Thermal Model Results

The results of the thermal analyses for Configurations 1, 2, and 3 are here presented. Fig. 81 provides the thermal maps under steady-state conditions, specifically at 1250 rpm and 1500 Nm. Meanwhile, Fig. 82 illustrates the thermal transients of both the stator and rotor windings, transitioning from nominal condition to the peak torque of 3330 Nm at the base speed. The primary objective of the transient analysis is to highlight the time required for each configuration to reach the thermal limit of 165 °C. This latter is safely lowered compared to the actual thermal limit of 180 °C. All three configurations comply with the specified thermal constraints, with Configuration 3 exhibiting the most favourable performance. In particular, it achieves a lower maximum temperature (i.e. 134°C) on the rotor at steady-state operation than Configurations 1 (143°C) and 2 (141°C). In addition, it takes 245 seconds for Configuration 3 to reach the specified temperature of 165 °C, surpassing the respective times of 140 seconds and 125 seconds for Configurations 1 and 2.

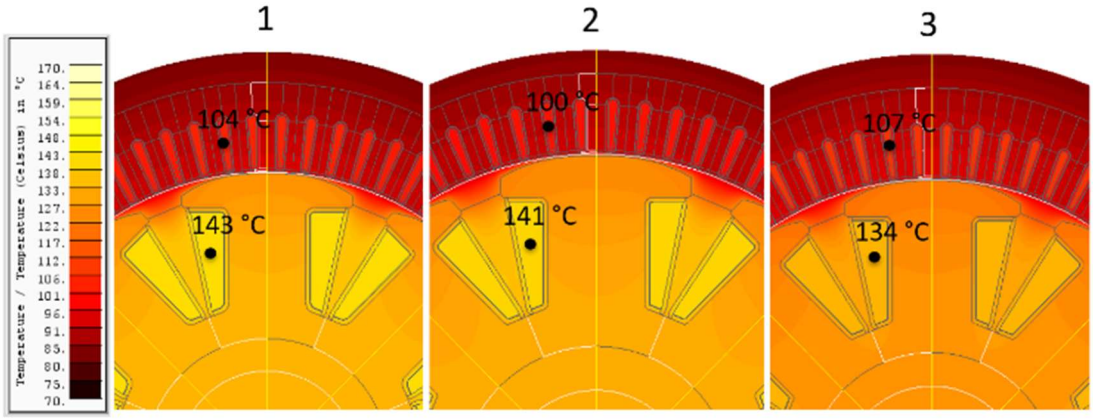

Fig. 81. 2D FE Steady state thermal map comparison of configuration 1,2 and 3 at nominal conditions (1500 Nm @ 1250 rpm)

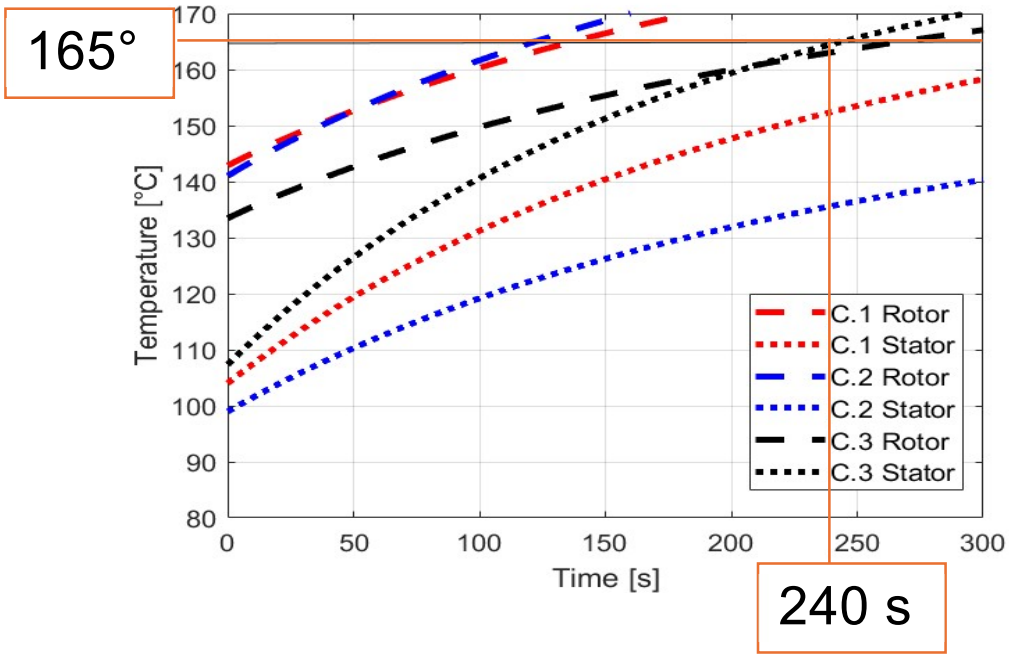

Fig. 82. Transient thermal trends of stator and rotor winding temperatures from nominal to overload conditions @ 1250 rpm. ("C.1, C.2 and C.3" are for Configurations 1, 2 and 3, respectively).

6.1.6 FE Structural Analysis Model and Results

Configurations 1, 2, and 3 undergo FE structural analysis to ensure their mechanical integrity at the maximum speed of 3240 rpm. The FE model description and results are presented in this section. The resistance of the rotor at the maximum speed of 3240 rpm is assessed through FE simulations, employing MSC Marc 2020.1 software.

A plain strain assumption is made, with a chosen domain thickness of 0.5 mm, equivalent to a single rotor lamination. Due to symmetries within the rotor, only one half of the rotor pole and winding is modeled, representing 1/16 of the complete rotor [2]. The rotor mesh comprises approximately 10000 first-order, quadrilateral elements (QUAD4), while the winding mesh consists of about 4000 QUAD4 elements, with an average mesh size of around 0.5 mm. Material properties for the simulations are detailed in Table XXXIII. The mechanical properties of the winding are derived from those of copper and resin using the rule of mixtures for density (19) and the inverse rule of mixtures for Young's modulus (20), where F_f, ρ_c, ρ_r, E_c, and E_r denote the rotor fill factor, copper density, epoxy density, copper Young's modulus, and epoxy Young's modulus, respectively.

$$\rho_{winding} = F_f \rho_c + \left(1 - F_f\right)\rho_r \tag{19}$$

$$E_{winding} = \frac{1}{\frac{F_f}{E_c} + \frac{\left(1 - F_f\right)}{E_r}} \tag{20}$$

A unilateral sliding contact is established between the winding and the rotor core, with a friction coefficient of 0.35. The winding is secured in place with a linear spring, ensuring contact with the rotor. This spring, with a stiffness equal to that of the end winding, has one end fixed at one symmetry plane, while the other end is connected to the winding nodes using an RBE3 link (Fig. 83). The model is constrained by two symmetry planes at the iron core boundaries. A centrifugal force is added to the model nodes, considering the speed of 3240 rpm. The maximum radial displacement at the peripheral points of the rotor is between $5 \cdot 10^{-3}$mm and $8 \cdot 10^{-3}$ mm in all configurations, indicating that the rotor is not expected to impact the stator at the maximum speed. Von Mises stress within the rotor at the critical speed is depicted in Fig. 84. The major stress concentrations are found at the fillets at the base of the pole, with maximum stress values of 35.7 MPa, 37.8 MPa, and 36.8 MPa for Configurations 1, 2, and 3, respectively, i.e. ≈8.5 times lower than the yield strength of the ferrous material. To assess the effect of the end windings, the resistance of the rotor in Configuration 3 is evaluated with an additional 3D FE simulation. This model represents 1/16 of the rotor cross-section and extends for the entire rotor length. The rotor is discretized with approximately 571000 first-order, tetrahedral elements (TETRA4), while the winding is made up of about 259000 TETRA4 elements. The mesh, with a maximum size of 3 mm, is refined in zones with increasing curvature to balance computational cost and accuracy. The equivalent von Mises stress in the rotor for Configuration 3 is shown in Fig. 85b. The critical zone within the rotor is at the fillet at the top of the pole, corresponding to the end winding. Here, the maximum stress is 87.3 MPa, 92.4 MPa, and 90 MPa for Configurations 1, 2, and 3, respectively. In all cases, the maximum stress is well below the yield strength for all machines, allowing adaptation for higher-speed applications.

Table XXXIII
MATERIALS' STRUCTURAL PROPERTIES

Parameter	**M350 50A**	**Copper**	**Insulation**
Density [kg/m^3]	7650	8900	900
Young's Modulus [MPa]	186000	110000	750
Poisson's Ratio	0.3	0.3	0.3
Yield tensile strength [MPa]	320	-	-

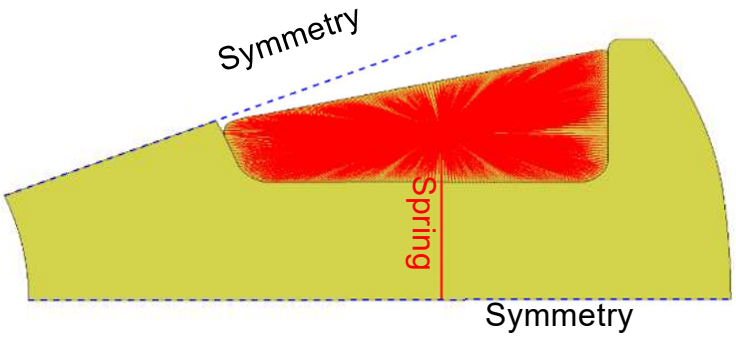

Fig. 83. 2D FE structural model setup showing symmetry plans, spring and RBE3 link.

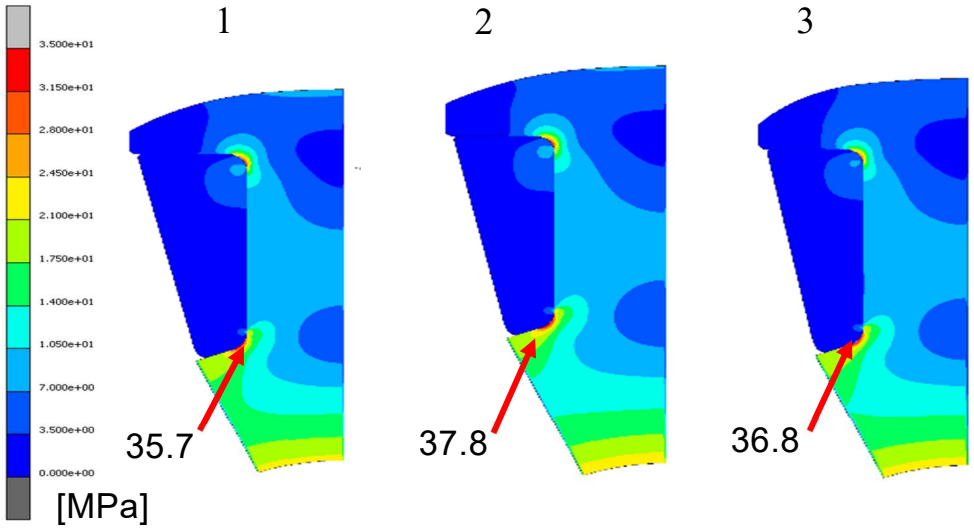

Fig. 84. Contour plot of von Mises equivalent stress for Configurations 1, 2 and 3.

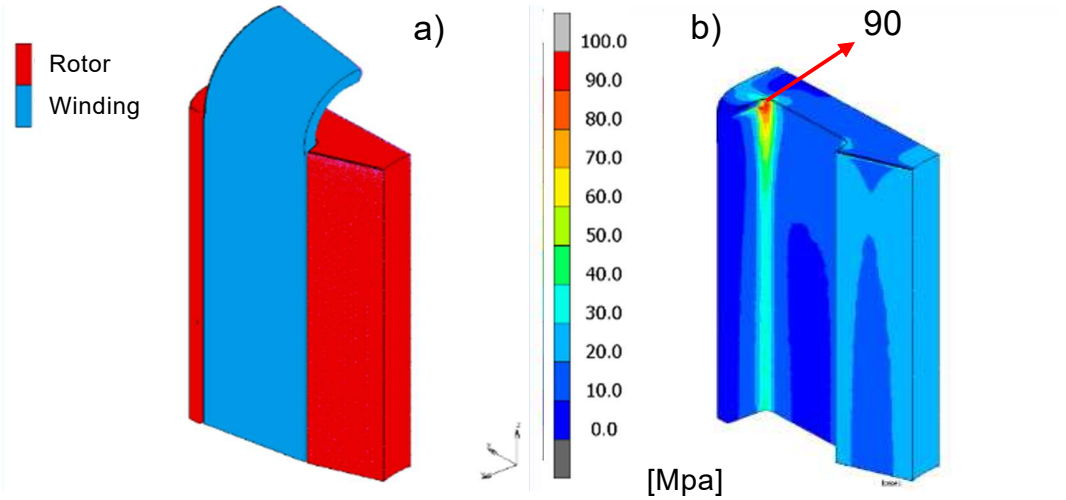

Fig. 85. 3D FE model. a) Isometric view, b) Von Mises equivalent stress map for Configuration 3.

6.1.7 Final Considerations and Best Choice Designation

In this section, a summary is provided for the strengths and weaknesses of the three configurations in thermal, structural, and electromagnetic aspects, aiming to identify the optimal solution.

In terms of purely electromagnetic performance, Configuration 2 demonstrates superior behaviour compared to 1 and 3 in efficiency, torque ripple, and base speed, both in nominal and overload conditions. Conversely, Configuration 3 exhibits significantly better thermal performance, surpassing the required overload index. All three machines display adequate structural robustness, with a safety coefficient exceeding 3. Configuration 1 excels in this aspect, surpassing the others.

Table XXXIV consolidates the multi-physics comparison among Configurations 1, 2, and 3 into six essential categories, each rated from 1 to 3 against the requirements, where 1 signifies the worst and 3 the best of the three. All the performance metrics are equally weighted. Based on this analysis, Configuration 3 emerges as the ideal candidate to replace the existing IPM machine currently implemented on board of the mining truck.

Table XXXIV
MULTI-PHYSISCS PERFORMANCE COMPARISON

Performance metric	**C. 1**	**C. 2**	**C. 3**
T-Ω Capability	1	3	2
Efficiency	1	3	2
Active Weight	3	1	2
Thermal Overload Capability	2	1	3
Maximum Speed Allowed	3	1	2
Excitation System Maximum Power	2	1	3
Final Score	**12**	**10**	**14**

6.1.8 Conclusions

This chapter addressed one of the current major challenges in the design of electric vehicle propulsion systems, i.e. to eliminate rare-earth PMs from the relative traction motors. To this purpose, considering a mining application, the multi-physics design of a WRSM is assessed with the intention of replacing the IPM motor currently implemented on-board of a mining truck. The design principles prioritized simplicity of construction and cost effectiveness. In this context, there was a specific requirement to have minimal impact on the overall system, with due importance given to the existing housing and cooling systems.

The design process started with a thorough analysis of the key performance requirements of the current IPM motor and the associated constraints. Key performance metrics under investigation included torque, torque ripple, efficiency, size, power of the excitation system, temperatures and relative overload capacity, and structural robustness up to 3240 rpm. After achieving an initial configuration that closely aligned with expectations, the design underwent a meticulous optimization process. Three electromagnetically superior machine configurations were identified as potential candidates and subjected to detailed thermal and structural analyses.

Each configuration demonstrated excellent performance in both thermal and structural domains, exhibiting satisfactory thermal overload capacity and a structural safety coefficient exceeding 3 at the maximum speed. However, based on the results obtained, Configuration 3 emerged as the most suitable choice for the specific requirements at hand, with 95.7% and 91.7 % efficiency values being

achieved at 1500 Nm and 3330 Nm respectively, 0.88A_W kg, an overload capacity of 240 s, a structural safety coefficient of 3.5 and a required maximum power for the excitation system supply of 3.8 kW.

6.1.9 Chapter's Closing Remarks

This chapter demonstrated the effective elimination of RE materials in high-demand off-highway sectors, focusing on the mining industry. The transition from IPM motors to WRSM offers a promising alternative, balancing performance and cost efficiency. Through detailed design optimization and multi-physics analyses, we confirmed that the WRSM configuration provides a viable replacement for IPM motors, achieving the necessary torque-speed characteristics without compromising structural integrity or thermal performance.

These findings reinforce the potential for RE-free solutions across industries requiring robust and reliable propulsion systems. The next chapter will explore the application of these methodologies in the aerospace sector, further highlighting the versatility and broader impact of RE reduction strategies.

7. Case Study: Rare Earth Reduction in Aerospace Sector

7.1 Design Optimization of a Starter Generator for More Sustainable High Power Density Aerospace Applications

7.1.1 Introduction

The electrification of aerospace propulsion systems is at the forefront of efforts to enhance both performance and environmental sustainability. This chapter focuses on the design and optimization of a SPM motor specifically developed for aerospace applications, aiming to reduce reliance on RE materials while maintaining high power density and operational efficiency.

The research presented in this chapter builds on previous work that explored alternative motor designs for various sectors. Here, the SPM motor is optimized through a series of electromagnetic simulations, material evaluations, and thermal analyses to meet the stringent performance requirements of aerospace propulsion. Special attention is given to weight reduction and compactness, two critical factors in aviation, while ensuring that the motor can still deliver the required torque and efficiency.

The design process uses techniques for optimizing the magnet arrangement and stator configuration to minimize losses and improve heat dissipation. The motor's performance is evaluated under various operating conditions to ensure it can handle the dynamic and thermal stresses encountered in flight.

This work, drawing from methodologies discussed in previous chapters and referenced articles, highlights the feasibility of reducing RE material usage without compromising the critical performance metrics required in aerospace propulsion. It also opens up new possibilities for sustainable and efficient electric flight.

7.1.2 Requirements and Starting Machine

In this section, the performance and environmental constraints adopted for the specific application, along with the design of the starting machine, are outlined. The starting machine is obtained through iterative adjustments within an FE-based

environment, i.e. Altair Flux, aimed at closely approximating desired performance levels and adhering to predefined constraints before the optimisation process.

A. Requirements and Constraints

For the specified application, a fixed-speed 5 kW-10000 rpm/30 kW-10000 rpm starter/generator is required, together with an efficiency value exceeding 96% and a power density of at least 1.5 kW/kg. Further constraints are delineated as follows.

- Torque ripple should ideally remain below 10% during generating mode and below 15% in motoring mode. The total harmonic distortion (THD) of the airgap flux density (B_airgap) should be limited to 5%. The THD reduction leads to benefits even on the loss reduction both in the core and magnets.
- The cooling system must utilize water with a minimum fluid inlet temperature of 65 °C and a maximum flow rate of 0.12 L/min, aimed at minimizing component weights and costs.
- The combined weight of copper and magnets should not exceed 4 kg and 1 kg, respectively, to address environmental concerns.
- The average temperatures of magnets and windings must remain below 130 °C to maintain adequate safety margins for UH magnet utilization (preventing demagnetization) and to accommodate Class H insulators. These measures are essential for both economic viability and environmental sustainability. To streamline the design and optimization process for simplicity and efficiency, temperature control is managed by limiting the current density during this stage. Subsequent thermal analyses are then carried out for evaluating temperatures.

All the aforementioned specifications are presented alongside the selected materials for both lamination and magnets in Table XXXV. NO20 and N38UH materials are chosen for the project's high standards, ensuring the required performance.

B. Starting Machines Design and Performance

Based on the constraints and specific requirements, the SPM topology is selected for its suitability to the given demands. After numerous iterations, a preliminary configuration, shown in Fig. 86, is established. This configuration comprises 4

pole pairs, 72 stator slots, and a double-layer winding with 3 slots per pole per phase, with a short-pitched arrangement by 1 slot to mitigate torque ripple. This configuration is iteratively achieved to meet the power density and efficiency requirements while accommodating as many environmental sustainability constraints as possible. For the cooling system, an external aluminium casing with a thickness of 8 mm and a solenoidal channel with 12 turns is considered. This choice aligns with the intention of weight minimization and environmental impact reduction, as ensured by the complete recyclability of aluminium.

The decision to limit the number of pole pairs to 4 (resulting in 667 Hz @ 10000 rpm) serves as a compromise between minimizing AC losses and maximizing power density. To ensure minimum AC loss generation in windings, conductors with a diameter of 0.8 mm are adopted for the application. The performance metrics of the resultant machine is detailed in Table XXXVI together with the specified requisites. It is apparent that while the initial machine performs well in terms of efficiency and temperature, there are significant areas for improvement across other aspects. Due to the complexity of the problem arising from the numerous variables and conflicting requirements, a decision is made to optimize the starting machine using the MOGA. The goal is to generate a range of optimal configurations as potential candidates whose performance metrics will be compared based on the requirements. The following section presents the parameters involved in the optimization process and the resulting best configurations.

Table XXXV
SPM REQUIREMENTS AND CONSTRAINTS

Parameter	**Value**	**Parameter**	**Value**
Essential Performance Requirements			
Generating Power [kW]	**30**	Motoring Power [kW]	**5**
Nominal Speed [rpm]	**10000**	Efficiency Gen. [%]	**≥ 96**
Secondary Requirements			
THD B_airgap [%]	**≤ 5**	Torque ripple @ Gen. [%]	**≤ 10**

Parameter	Value	Parameter	Value
Essential Performance Requirements			
Active Power Density [kW/kg]	**≥ 1.5**	Torque ripple @ Mot. [%]	**≤ 10**
Designed Lamination Type	**NO_20**	Designed Magnet Type	**N38UH**
Inlet Water Temperature [°C]	**≥ 65**	Water Flow Rate [L/min]	**≤ 0.12**
Average Magnet Temperature [°C]	**130**	Average Winding Temperature [°C]	**130**
Copper Weight [kg]	**≤ 4**	Magnets Weight [kg]	**≤ 1**

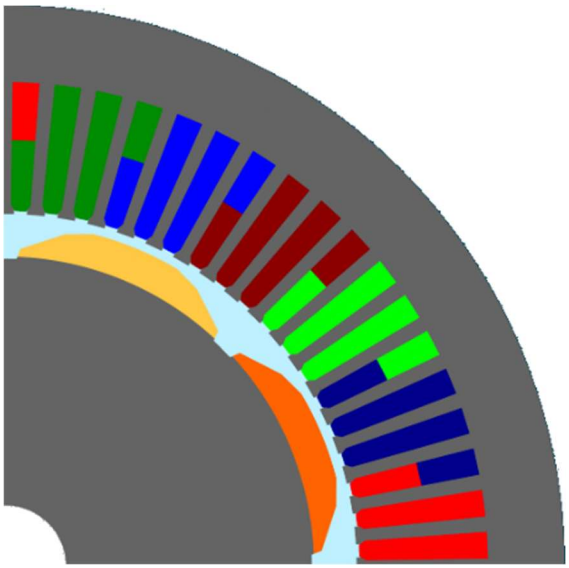

Fig. 86. A pole pair of the starting machine.

Table XXXVI
PERFORMANCE OF STARTING CONFIGURATION

Outputs		Requirements	Starting Machine
Generating Power [kW]		**30**	**30**
Efficiency Generating [%]	(A)	**≥ 96**	**97.8**
Active Power Density [kW/kg]	(B)	**≥1.5**	**1.4**
Torque ripple @ Generating [%]	(C)	**≤ 10**	**9.9**
Torque ripple @ Motoring [%]	(D)	**≤ 15**	**20.2**
THD B_airgap [%]	(E)	**≤ 5**	**6.2**

Outputs		Requirements	Starting Machine
Average Magnet Temperature [°C]	(F)	**≤ 130**	**123**
Average Winding Temperature [°C]	(G)	**≤ 130**	**119**
Copper Weight [kg]	(H)	**≤ 4**	**4.9**
Magnets Weight [kg]	(I)	**≤ 1**	**1.1**

7.1.3 Parametrization and Optimisation Results

A. Optimization Settings and Parameters

Based on the results obtained with the initial configuration and in line with the design requirements, the variables and confidence intervals of the optimization process are selected. Constraints are then imposed on the quantities listed in Table XXXVI. Fig. 87 illustrates the geometric parameters characterizing the slots and magnets, while Table XXXVII lists all the parameters involved in the design. In the following subsection, the performance of 10 machine candidates are reported and compared. These machines are selected from the numerous possible solutions resulting from the optimization, among which the final machine will be chosen.

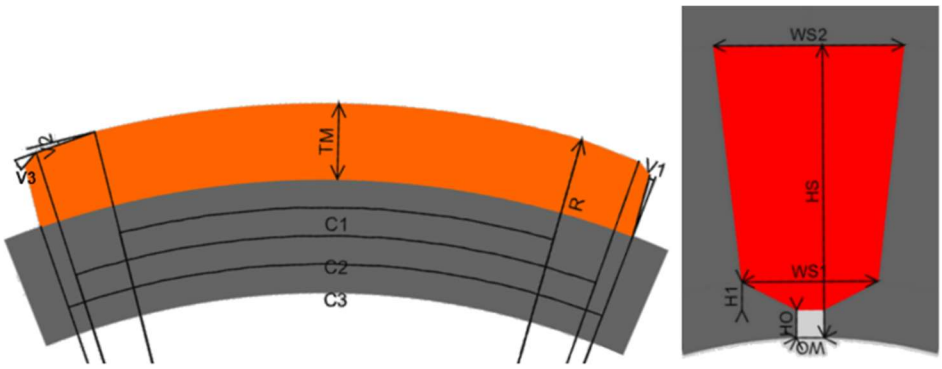

Fig. 87. 2D geometrical optimization parameters for magnets (left) and slots (right).

Table XXXVII

PARAMETERS INVOLVED IN THE OPTIMIZATION

Name	Description	Name	Description
L	Stack length	Id	Inner Diameter
Od	Outer Diameter	HS	Slot Height
TM	Magnet Thickness	WS2	Slot Width Upper Part
R	Magnet Outer Radius	H1	Slot Height Lower Part
C1	Magnet Outer Arc	WS1	Slot Width Bottom

Name	Description	Name	Description
C2	Magnet Middle Arc	HO	Slot Opening Height
C3	Magnet Inner Arc	WO	Slot Opening Width
V1	Magnet Edge Side Angle	N	Turns per coil
V2	Magnet Edge Top Angle	Nh	Parallel wires in a conductor
V3	Magnet Edge Top-Side Angle		

B. Optimization Results

Firstly, the optimization results are meticulously filtered based on the required design power. All configurations within the power range of approximately 30 kW at 10000 rpm are retained. This margin ensures that errors in temperatures, set at 130°C during the optimization process and errors in the MTPA angle do not inadvertently exclude optimal configurations. Among the remaining possibilities, a selection of 10 solutions meeting both the efficiency and power density requirements is made in the following way: the 5 with the highest efficiency and the 5 with the minimum weight. This strategic approach aims to prioritize the optimization of key requisites, such as efficiency and power density, which determine the electability of the proposed machines as solutions while providing the defined power. Violations of these three requirements are not allowed. Table XXXVIII presents a comparative analysis of these configurations against each other and in alignment with the design requests. Fig. 88 illustrates the distribution of configurations from the optimization process, filtered by power, in the Active Weight-Efficiency plane. Additionally, it highlights the regions where the 10 selected configurations are concentrated.

The subsequent section comprehensively analyses the obtained results to ascertain the best configuration. Initially, emphasis is placed on the fundamental requisites of power density and efficiency. Then, the scope broadens to encompass all electromagnetic requirements (power density, efficiency, toque ripple and THD) before further expanding to include environmental sustainability constraints.

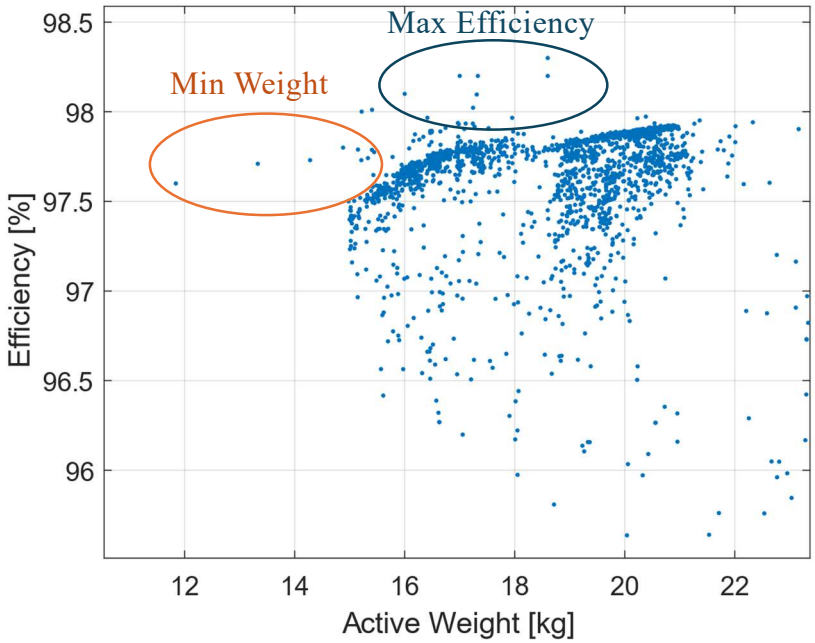

Fig. 88. Optimization results in Active Weight-Efficiency plane, highlighting the position of the 10 selected configurations. Minimum weight and maximum efficiency in orange and blue, respectively.

Table XXXVIII
PERFORMANCE COMPARISON OF THE SELECTED CONFIGURATIONS

Config.	***Outputs (Table II)***								
	A ≥ **96**	***B*** ≥ **1.5**	***C*** ≤ **10**	***D*** ≤ **15**	***E*** ≤ **5**	***F*** ≤ **130**	***G*** ≤ **130**	***H*** ≤ **4**	***I*** ≤ **1**
Starting	97.8	1.4	9.9	20.2	6.2	123	119	4.9	1.1
Maximum Power Density Configurations									
1	97.7	2.2	13.0	28.5	15.5	139	137	3.0	0.7
2	97.8	2.0	7.4	18.9	8.1	130	134	3.9	0.7
3	97.7	2.0	3.0	7.1	9.0	130	129	3.5	0.7
4	97.8	1.9	3.3	6.9	8.2	127	127	4.9	0.5
5	97.5	2.4	5.6	19.5	11.0	143	144	3.6	0.7
Maximum Efficiency Configurations									
6	98.1	1.9	5.5	27.9	5.4	123	125	2.9	0.7
7	98.2	1.7	7.0	15.6	5.4	118	118	3.3	0.9
8	98.3	1.6	3.4	15.6	11.1	117	119	3.8	0.8
9	98.2	1.9	2.8	11.5	8.4	119	120	3.8	0.6
10	98.1	1.6	5.6	28.4	4.8	117	116	3.4	0.7

7.1.4 Best Machine Selection

In this section, a critical comparison of the 10 chosen configurations is performed, drawing upon their performance metrics delineated in the preceding section (Table XXXVIII). Also, this section illustrates how integrating environmental considerations can culminate in divergent choices, potentially sacrificing marginally electromagnetic performance yet markedly mitigating environmental footprint.

A. Performance Analysis Metric

The performances of the top 10 identified machines are meticulously compared by assigning a value from -10 to 10 to each output listed in Table XXXVIII. This evaluation is grounded in the project's specifications and the extreme values observed among the 10 machines. For example, the project stipulates a target value of ≤ 10% in Category C, representing torque ripple during generator operation. The most favourable achieved value stands at 3.0%, while the least desirable is 13%. Consequently, the machine achieving 3.0% earns a perfect score of 10, whereas the one with a torque ripple of 13% incurs a deduction of -10 points. Following this rationale, the optimal solution is discerned based on primary requirements (A-B), electromagnetic and durability and comfort specifications (A-E), and comprehensive optimization criteria (A-I). This approach illustrates how integrating environmental considerations can yield alternative selections compared to solely prioritizing fundamental performance metrics (weight and efficiency), even at the conclusive stage of the design.

B. Optimal Configurations Detection

Based on the preceding analysis, numerical results for the top 10 configurations are provided, evaluated across categories A and B, categories A through E, and across all categories examined (Fig. 89). In each case, the values are normalized relative to the best-performing configuration, which is assigned a score of 10 (1 unit). Upon review of the plotted graphs, configuration 5, then 3 and 4, and finally 9, emerge as optimal choices. The following section will discuss these results in greater detail and draw broader conclusions.

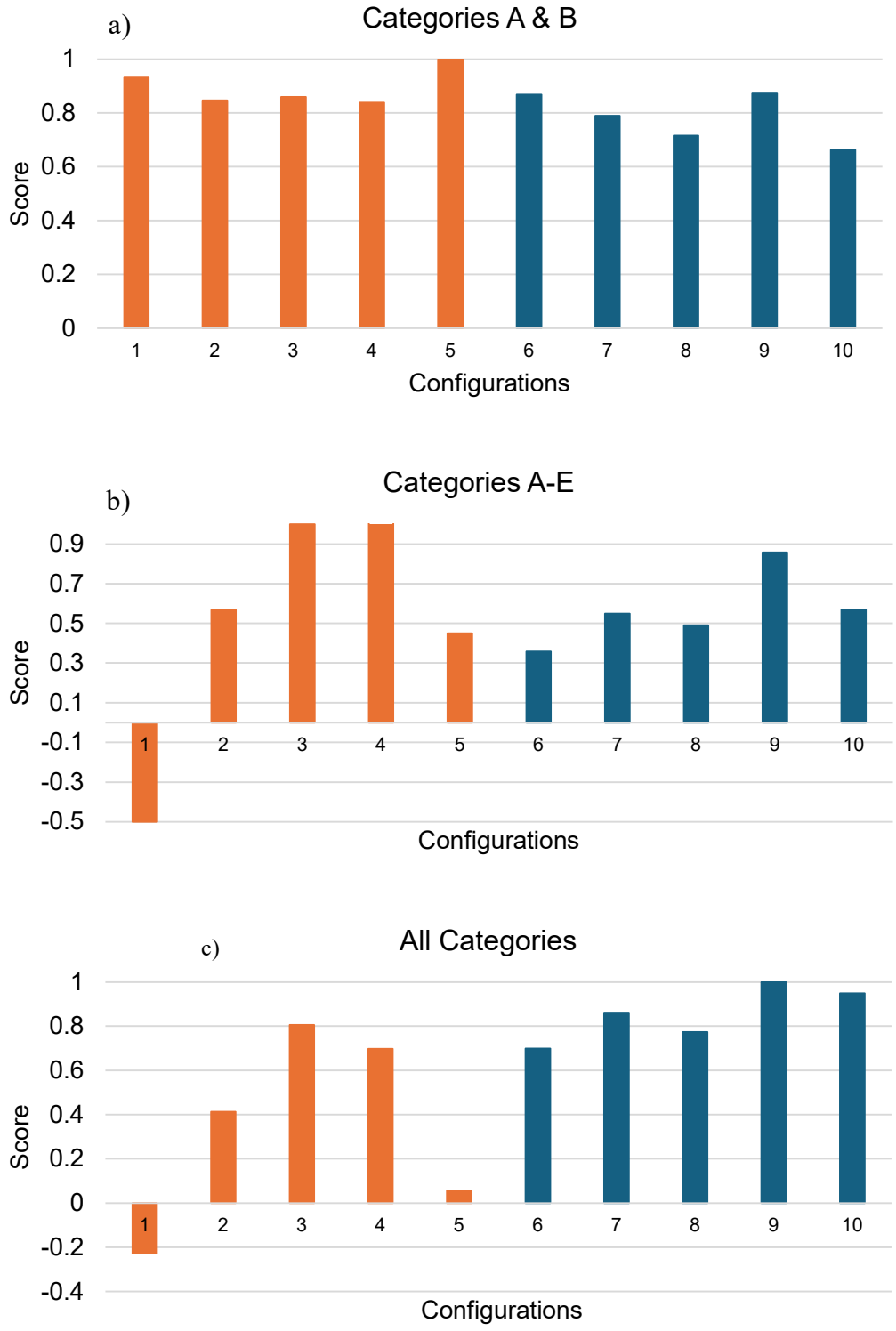

Fig. 89. Final score comparison of the 10 selected configurations evaluated on: a) Categories A & B, b) Categories A through E, c) All categories.

7.1.5 Results Discussion and Final Choice Improvements

In this section, the optimization results presented in Table XXXVIII and the evaluation depicted in Fig. 89 are analysed and commented on with the aim of

deriving a series of general considerations and naming the final configuration. Subsequently, the latter is subject to geometric refinement with the main purpose of further reducing the weights.

A. Results Discussion and Observations

Observing the results depicted in Fig. 89, it becomes apparent that there is a fluctuation in the attractiveness of the configurations under examination as durability and comfort requirements (minimization of vibrations and noise by minimizing torque ripple), thus other environmental impact parameters (reduction in the quantity and quality of materials used) are introduced. Particularly noteworthy are the following observations:

- the obtained configurations solely evaluated on power density and efficiency exhibit almost uniformly excellent performance concerning project requirements, with the exception of configurations 8 and 10, which display slightly lower scores compared to the others. Configuration 5 emerges as the top candidate due to its notably high-power density value of 2.4 kW/kg;
- with the inclusion of torque ripple and THD requirements, configurations 1 and 5 undergo a reversal in trend, becoming less suitable alongside configuration 6. This behaviour can be attributed to the fact that the general increase in power density tends to result in an average increase in torque ripple and THD due to higher saturated core regions. Configurations 3 and 4 emerge as superior solutions. Fig. 90 shows the magnetic flux trend in the airgap of configurations 1, 3, 4, and 5;
- environmental considerations lead to an average reversal in trend, with all high-efficiency machines surpassing those with lower weight, as indicated in Table XXXVIII. This is due to the fact that maximizing efficiency, while resulting in slightly lower average power density values, allows for the mitigation of all other parameters, including copper quantity and temperatures, ensuring a generous safety margin for selected insulation and magnet quality. Such temperatures would also align with the use of even less additive (Cobalt and Dysprosium) magnets of "AH" quality compared to the "UH" chosen for the project;
- furthermore, it can be stated that maximizing power density allows for a greater average decrease in magnet quantity compared to the other

configurations presented here. However, this necessitates a greater exploitation of conductors by increasing current densities. The direct consequence is a tendency to saturate the ferromagnetic core, resulting in increased torque ripple and temperature. All of these factors contribute to increased losses and reduced efficiency.

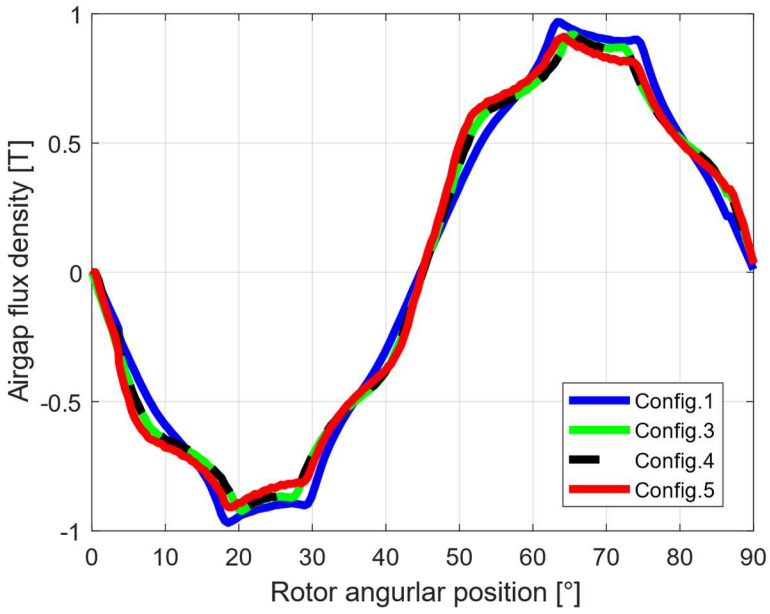

Fig. 90. Flux density trend in the airgap versus rotor position for configurations 1, 3,4 and 5.

B. Final Choice and Structural Improvements

Based on a comprehensive assessment across all criteria, configuration 9 emerges as the optimal choice, meeting all project requirements exceptionally well. It achieves an efficiency exceeding 98%, as well as it reduces copper and NdFeB quantities by 5% and 40%, respectively, compared to the initial requirements. The selected SPM topology allows for additional geometric modifications aimed at reducing rotor weight and inertia, such as integrating holes into the rotor structure (refer to Fig. 91), which can also act as cooling ducts. This adjustment results in a further weight reduction of approximately 3 kg, boosting the power density to around 2.3 kW/kg without compromising electromagnetic performance, as evidenced by the unchanged main (blue and yellow) magnetic field lines depicted in Fig. 92. Moreover, the dimensions of the rotor structure are designed to ensure that Von Mises stress values remain below 200 MPa in the most critical region, specifically the central bridge. For enhanced safety, lateral tabs combined with additional parts at the magnet ends are introduced to securely retain the magnets

in position, complemented by adhesive bonding. The lateral additions to the PMs are also optimized for size to minimize tabs and associated leakage fluxes.

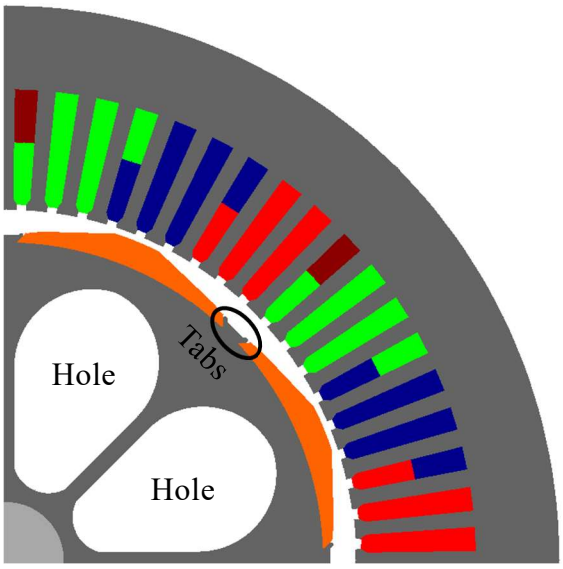

Fig. 91. One pole-pair of the selected machine (n.9), highlighting holes and tabs.

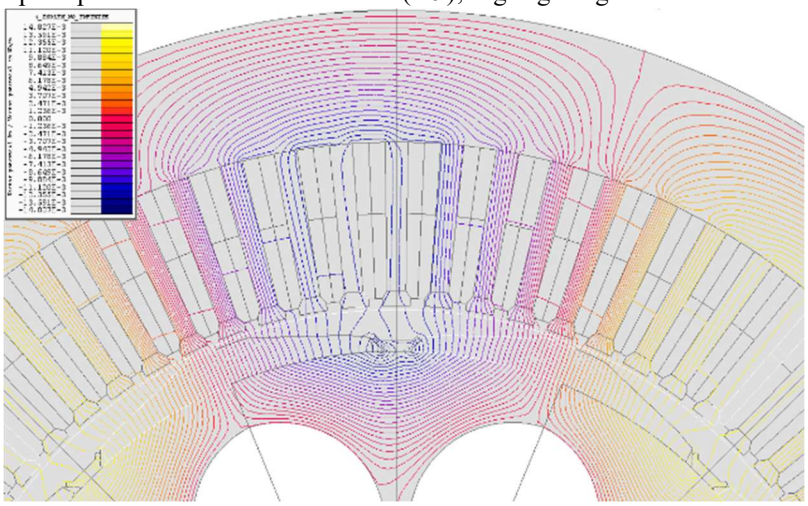

Fig. 92. Magnetic flux lines trend of the modified selected configuration 9. The blue and yellow line paths are highlighted.

7.1.6 Conclusions

This chapter detailed the design process of an SPM motor for a fixed-speed starter-generator application in the aeronautical sector. The motor design prioritizes performance metrics such as power density and efficiency while considering sustainability and environmental impact. Through a FE optimization process, ten optimal configurations were identified and evaluated based on various criteria, including electromagnetic performance, comfort and durability, and environmental impact. The results show that while maximizing power density tends to reduce material usage, it also leads to increased torque ripple and

temperature, potentially compromising efficiency. Conversely, prioritizing efficiency enables improved exploitation of copper and temperature reduction. After thorough analysis, configuration 9 emerged as the optimal choice, meeting or exceeding all project requirements with an efficiency higher than 98% and with a significant copper and magnet reduction. Geometric refinements further improved the motor's performance, achieving a power density of around 2.3 kW/kg. This study highlighted the importance of integrating environmental and sustainability considerations into motor design processes, as it can lead to more environmentally friendly choices without significant sacrifices in performance. By balancing performance metrics with environmental impact, the aerospace industry can move towards more sustainable and efficient electrified solutions.

7.1.7 Chapter's Closing Remarks

In this chapter, we have focused on optimizing an SPM starter/generator for aerospace applications, aiming to reduce RE dependency while maintaining high performance. The studies here concentrated on motor design and efficiency, without delving into the excitation system, a crucial aspect for stable motor operation. However, this omission was intentional, as the focus was strictly on optimizing the motor structure and material use.

The next chapter, while not directly related to the cases discussed earlier, addresses the excitation system in a completely different context. It explores a mathematical model for predicting voltage reduction due to uncontrolled commutation in hybrid exciters, of synchronous machines intended for power generation in a small-medium power range applications, including aerospace and. This represents a separate line of investigation aimed at addressing challenges specific to excitation systems, which were not the focus of the previous chapters.

Although this topic might seem a deviation from the thesis main path, it is actually a complementary study that broadens the scope of this doctoral research. By including this analysis, the thesis provides a more complete picture of the different aspects of electric machine design and operation, ensuring that even auxiliary systems like excitation are considered in the broader context of sustainable propulsion and energy solutions.

8. CASE STUDY: EXCITATION SYSTEM

8.1 A Simplified Analytical Approach for Hybrid Exciters of Wound-Field Generators

8.1.1 Introduction

Mid-power generating sets are widely used for grid code applications, marine naval ships, aerospace, shopping malls and industrial buildings, and critical standby power applications [81]. Their basic architecture consists of a WFSG, a brushless excitation system comprising an automatic voltage regulator [82]. While the WFSG and its ES are well-known and consolidated, the ever-stringent power density, efficiency, reliability and power quality requirements have led to a growing interest in renewing these technologies [83]-[87] in all applications where they are used, including marine [88] and aerospace [89]. Consequently, a lot of effort has been also spent on the development of analytical, numerical and hybrid analytical-numerical models for the accurate prediction of the performance of WFSGs and exciters [90]-[98]. Some examples are reported in [90]-[94], where typically the investigations are based on the permeance/permeability function concept. However, the estimation of such a function is a complex task and is then often performed using FE analyses. In addition, the majority of these examples are also accompanied by numerical solutions, due to presence of damper windings in WFSGs and of the rotating diode rectifier in the exciters. These hybrid analytical-numerical methods are still advantageous compared to fully numerical (e.g., FE) solutions, as the simulation time is reduced while achieving a reasonable level of detail and accuracy. In fact, the main challenge of a numerical methodology is the computation burden, especially when design optimizations are involved [95].

A full analytical model, on the contrary, could drastically reduce the required computational resources and times, but too many assumptions are often considered which can lead to inaccurate results. This is especially true for brushless exciters of mid-power generating sets for the following reasons:

1) The design guideline for such electrical machine is the simplicity, which often results in non-optimal designs. For example, the armature winding is often equipped with a low number of slots-per-pole-per-phase

and this means that the sinusoidal approximation of the electromagnetic quantities (e.g., the magneto-motive force) should be avoided.

2) The salient structure of the stator may lead to a complex evaluation of the permeance/permeability function or to large inaccuracies when an isotropic profile was hypothesized.

3) The connection between the rotating armature of the exciter and the field winding of the main alternator is made through a rotating, uncontrolled diode rectifier. This means that the armature current waveforms cannot be considered sinusoidal, as they feature a squared shape when the diode commutation process is neglected.

4) In addition, the diode commutation process, while it is often ignored or neglected, can play an important role in defining the real shape of the armature current waveforms, as well as in the accurate evaluation of the available output voltage at the main generator rotor terminals.

In this chapter, a fully analytical model which does not rely upon any numerical simulation is proposed, and the following measures are taken to overcome the above challenges:

1) The use of equivalent winding functions (EWFs) to take into account the simple layout of the armature winding.

2) The implementation of simplified rotor and stator profiles that, while neglecting some secondary phenomena (such as the rotor slotting), permits to remove the need for FE simulations for the permeance/permeability function evaluation and to keep the accuracy of results acceptable.

3) The inclusion of the diode rectifier and the relevant commutation processes through the analytical calculation of the diodes' commutation angle, allowing to define the armature current waveforms imposing a trapezoidal trend and, in turn, eliminating the need for a numerical resolution of the currents themselves.

4) The inclusion of the machine mutual inductances in the commutation angle estimation model, as it can play a role in the correct estimation of the armature current shape.

The primary assumptions that significantly influence the adopted approach include:

- Treating the electromagnetic phenomena in the windings' active sections separately from those occurring in the end windings.
- Considering the leakage flux paths as having a negligible impact on the main flux paths, thereby disregarding cross saturation.
- Employing a two-dimensional approximation for the magnetic field.
- Assuming linear magnetic behaviour in both the stator and rotor cores, thus ignoring any current-dependent variations in permeability.
- Presuming a uniform magnetic field intensity along the air gap in the radial direction.

As a vehicle to investigate the above concepts, an existing hybrid-excited exciter of a WFSG intended for marine applications is considered, as this is deemed an interesting platform for proving the analytical model flexibility (besides its resolution speed and accuracy) due to the presence on the stator of both field windings and PMs, arranged in a consequent-pole (CP) layout [85]. FE and experimental results are used to prove the model validity.

8.1.2 Analytical Model

The traditional layout of a mid-power generating set consists of a main 3-phase WFSG, whose field winding is fed through a 3-phase diode rectifier by a 3-phase, inverted-layout exciter. The equivalent circuit of the rotating elements of such a generating set can be represented as in Fig. 93. This is used for the development of the commutation angle estimation model, which is described in the next sub-section.

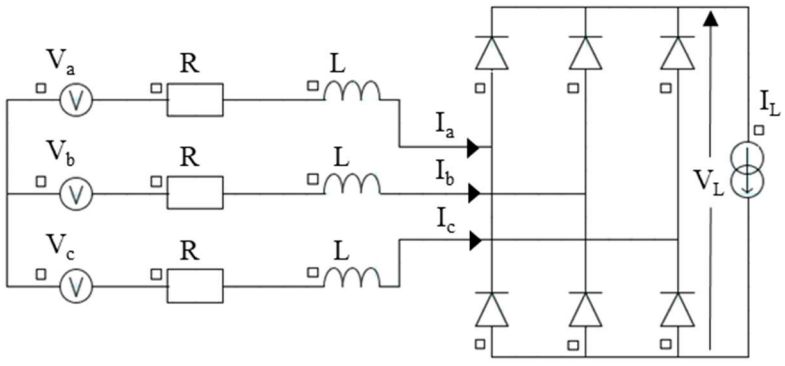

Fig. 93. Equivalent circuit of the rotating parts of a 3-phase generating set.

A. Commutation angle and ensuing current waveforms

In Fig. 93, V_a, V_b and V_c represent the exciter armature voltages, whereas the phase resistances, self- and mutual-inductances are indicated with R, L and M, respectively. The phase currents are I_a, I_b and I_c, while V_L and I_L are the rectified voltage and current, i.e. the main WFSG rotor winding voltage and current. The main WFSG rotor winding is modelled as a DC current source since its self-inductance is relatively large.

When ideal diodes were considered and null values of L and M were assumed, then the exciter phase currents would be alternative waveforms featuring a squared shape as shown by the dashed trend of Fig. 94 with the amplitude equal to I_L.

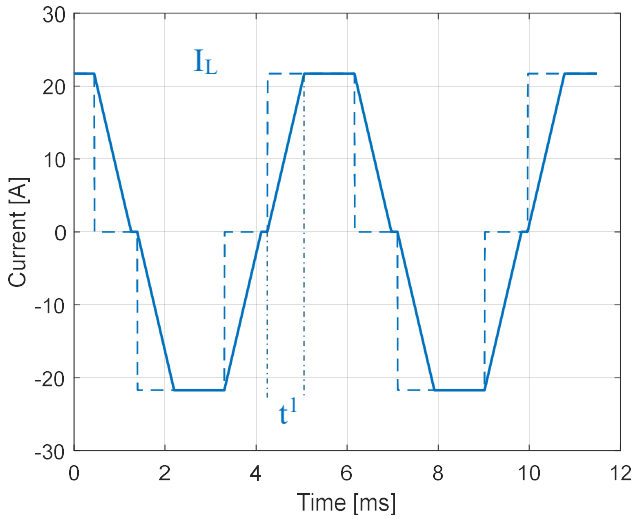

Fig. 94. Comparison between exciter's armature currents under ideal (dashed line) and non-ideal (continuous line) conditions.

This means that the diode commutations are assumed to be ideal, i.e. the current instantaneously steps from 0A up to I_L or down to $-I_L$, and vice versa. However, in small-to-medium size generating sets, the circuital parameters of the exciter cannot be neglected and can play an important role on the available rectified voltage. In fact, when L and M are not null or negligible, the phase current cannot instantaneously change and this results in a current waveform which can be assumed with a good approximation as a trapezoidal one, as shown in Fig. 94. In Fig. 94 the current rise time t^1, namely the commutation time, is also highlighted. Considering this scenario, during t^1 the phase current can be written as in (21).

$$I_D(t) = \frac{I_L \cdot t}{t^1} \tag{21}$$

During commutation, two phases are short-circuited, as long as the commutation angle is lower than 60° electrical (simple commutation). Considering the circuit of Fig. 93 and that a and b are the short-circuited phases, then (22) and (23) can be written. Using (22) for replacing I_b in (23), then (24) is obtained where $V_{ab}(t)=V_a(t)-V_b(t)$. In (24), it can be noticed that, besides the phase self-inductance L, also the mutual-inductance M has an effect.

$$I_a(t) + I_b(t) = I_L \tag{22}$$

$$V_a - RI_a - L\frac{dI_a}{dt} - M\frac{dI_b}{dt} = V_b - RI_b - L\frac{dI_b}{dt} - M\frac{dI_a}{dt} \tag{23}$$

$$\frac{V_{ab}(t) + R \cdot I_L}{2} = R \cdot I_a(t) + (L - M) \cdot \frac{dI_a(t)}{dt} \tag{24}$$

By integrating (24) between 0 and t_1, and indicating with ω and V_{LL} the angular frequency and the RMS value of the line-to-line supply voltage respectively, the commutation angle θ can be found as given in (25).

$$\theta = \arccos\left(1 - \frac{2 \cdot I_L \cdot \omega \cdot (L - M)}{V_{LL} \cdot \sqrt{2}}\right) \tag{25}$$

From (25), it can be noticed that the commutation angle depends on the main rotor current I_L, the supply frequency ω, the self- and mutual-inductances L and M, and the supply voltage V_{LL}. Therefore, a correct and possibly fast estimation of the machine inductance matrix and of the phase voltages is of paramount importance. Moreover, the commutation angle has an impact on the available rectified voltage, i.e. the higher the commutation angle θ, the lower the rectified voltage V_L.

The proposed analytical model starts from the calculation of θ through (25). This allows to estimate for any operating condition the phase current shape as in Fig. 94, thus removing the need for a numerical solution which would be computationally expensive. This inherently means that only steady-state operating conditions are considered, as any transient scenario would need a suitable dynamic model having the phase currents as state variables, thus requiring a numerical resolution [100]. The analytical model used to determine the machine inductances derives from [90], but some updates and variations are proposed to take the PMs and the relevant CP arrangement into account.

B. Machine analysis

A compact and accurate expression for the inductance matrix L(γ) of any rotating electrical machine has been presented in [90] and is reported in (26). In (26), γ is the position of rotor vs. stator which represents the mechanical state variable of the model; β is the rotor angular reference frame through which the position along the tangential direction is indicated; l is the machine axial length; μ_E is the equivalent permeability function, whereas $\overline{N_E}$ is the vector whose elements are the EWFs of the machine phases.

$$L(\gamma) = l \int_0^{2\pi} \mu_E(\beta,\gamma) \cdot \overline{N_E}\,(\beta,\gamma) \cdot \overline{N_E^T}(\beta,\gamma) d\beta \tag{26}$$

The equivalent permeability function μ_E is defined in (27), where μ_G is the magnetic permeability of any eventual material inside the air-gap (including air); τ_G is the mean equipotential line of the air-gap layer, i.e. a line perpendicular to the field lines in the air-gap, which can be then approximated as equal to $2\cdot\pi\cdot r_G(\beta,\gamma)$, where r_G is a function describing the distance of such a line from the machine axis; ε_E is the equivalent air-gap thickness function, which basically represents the length of the field lines in the air-gap, meaning that it would be simply the air-gap thickness function when no PMs are present.

$$\mu_E(\beta,\gamma) = \mu_G(\beta,\gamma)\,\frac{\tau_G(\beta,\gamma)}{\varepsilon_E(\beta,\gamma)} \tag{27}$$

In (28), where the EWF vector is defined, it can be seen that this is obtained as the difference between the vector $\overline{N}$ containing the WFs of the machine and its mean weighted value calculated over the whole tangential spam assuming μ_E as weight. The WF vector contains the information on the number, position and direction of the windings' active sides.

$$\overline{N_E}(\beta,\gamma) = \overline{N}(\beta,\gamma) - \int_0^{2\pi} \frac{\mu_E(\beta,\gamma)}{\int_0^{2\pi} \mu_E(\beta,\gamma)\,d\beta} \cdot \overline{N}(\beta,\gamma)\,d\beta \tag{28}$$

Differently from the salient-pole WFSG analysed in [90], the case study in this project equips PMs mounted on the inner profile of half (i.e. the CP layout) of the stator teeth. Therefore, the equivalent air-gap thickness function ε_E should take into account the information related to the PMs, besides that of the main air-gap.

In other words, besides the mean equipotential line of the air-gap layer τ_G, an extra mean equipotential line τ_M can be defined in the PMs layer which, similarly to τ_G, can be approximated as equal to $2\cdot\pi\cdot r_M(\beta,\gamma)$, where r_M is a function describing the distance of such a line from the machine axis. This line and the relevant functions are defined only where the PMs are present, thus taking into account the CP arrangement characterizing the exciter. Applying the Gauss' law to the surfaces delimited by τ_G and τ_M, ε_E is obtained as in (29), where ε_G and ε_M are the air-gap and PM thickness functions, and μ_M is the relative magnetic permeability function of the PM layer.

$$\varepsilon_E(\beta,\gamma) = \varepsilon_G(\beta,\gamma) + \varepsilon_M(\beta,\gamma)\frac{r_G(\beta,\gamma)\cdot\mu_G(\beta,\gamma)}{r_M(\beta,\gamma)\cdot\mu_M(\beta,\gamma)} \tag{29}$$

It is worth noticing that the model presented above is based on the assumption of linear behaviour of the ferromagnetic materials, as inferred by the dependence of the inductance matrix on the variable γ only (see (26)). However, it is also worth mentioning that exciters of WFSGs are typically designed to work in linear conditions even when the main machine operates at full load [85]. This allows to simplify the analytical approach and reasonably removes the need of including the magnetic saturation into account. On the other hand, when over-load operation was required, the exciter could operate in non-linear conditions and the model would require the inclusion of suitable measures (e.g. a saturation factor [101]) not to compromise the accuracy. Although this is easy to implement within the proposed analytical model, these measures require FE analyses for the calibration. Therefore, this is not done in this work, leveraging on the fact that exciters of WFSGs usually work under "normal" operating conditions.

8.1.3 Investigation on the Case Study

A. Background

As mentioned above, the analysed exciter includes PMs mounted on the inner profile of half of the stator teeth, used as additional magneto-motive force source with respect to that provided by the field windings. The hybrid-excitation applied to brushless exciters of small-to-medium power WFSGs, recently proposed in [85], achieves a significant ohmic loss reduction in the field winding and ensures a fully reliable voltage build-up. In [85], these two objectives are met with minimal structural modifications compared to its counterpart equipping field windings only. In addition, no system-level complications are required due to the choice of

targeting the no-load operation of the main generator for the PMs sizing. In other words, the rotating diode rectifier and the automatic voltage regulator are kept the same as in the classical configuration, thus complying with the simplicity and low cost requirements typical of such type of applications. The hybrid exciter under investigation is described in detail in the next sub-section.

B. Machine description

The main parameters of the hybrid exciter are summarized in Table XXXIX.

Table XXXIX
MAIN PARAMETERS OF THE HYBRID EXCITER

Parameter	**Value**	**Parameter**	**Value**
Outer diameter [mm]	500	Rated power [kVA]	5.35
Axial length [mm]	50	Rated voltage [V]	75
PM thickness [mm]	1	Rated speed [rpm]	1500
Rotor slot number	42	Pole number	14
Stator turns per coil	250	Magnetic material	M700-65A
Rotor turn per coil	250	PM material	BNP-6

A picture showing the real exciter stator with a zoom on 3 teeth is shown in Fig. 95, where the surface-mounted layout of the PMs as well as the CP arrangement can be observed, i.e. only one stator tooth in each pole pair is equipped with PMs. The mechanical air-gap thickness is constant (1 mm) under each stator tooth. The magnetic air-gap thickness under the teeth equipped with PMs is 2 mm, given that the PM thickness is 1 mm. The properties of the bonded BNP-6 PMs used in the exciter are reported in Table XL, whereas the stator and rotor coils' arrangement into the slots belonging to one pole pair are shown in Fig. 96.

The design methodology and performance figures of this case study are fully provided in [85], including its no-load and on-load operations as well as the temperature influence and demagnetization analysis on the PMs.

Fig. 95. Hybrid exciter stator highlighting the PM location and layout [85].

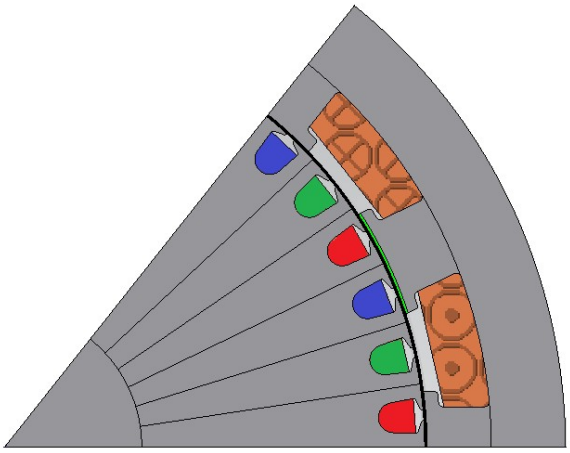

Fig. 96. Phases arrangement into the hybrid exciter's slots.

Table XL
PMs Main Properties

Type: Bonded NdFeB			
Remanence B_r [T]	0.55-0.62	Temp. Coeff. of H_{cJ} α(HcJ) [%/°K]	-0.35
Coercivity H_{cB} [kA/m]	285-370	Recoil Permeability	1.15
Intrinsic Ceorcivity H_{cJ} [kA/m]	600-755	Curie Temperature [°C]	300
Average Resistivity [mΩcm]	5.6	Max. Operating Temp. [°C]	130

C. Equivalent functions

This sub-section starts with the investigation on the case study of the analytical model described in Section 8.1.2. First, all the quantities involved in (26) are shown for the hybrid exciter at hand, then the machine inductances are also reported.

As mentioned in Section 8.1.1, the proposed analytical model aims at getting rid of any numerical analysis for its resolution. To such purpose, the first step involves

the use of step functions for the definition of the geometrical quantities involved in (27). The function $r_G(\beta,\gamma)$ is calculated as the average between an inner stator profile and outer rotor profile functions, taking into account the stator slots only, as this is deemed sufficient for the sake of this study. However, following the same rationale of using step descriptive functions, the rotor slots can be easily implemented within the model. In Fig. 97, the equivalent air-gap thickness function accounting for the PMs and derived in (29) is shown for one pole pair of the machine. To take into account the stator slot effect on the field lines, ε_E is increased by one order of magnitude in correspondence of the stator slot opening, thus the maximum value of ε_E is the result of this assumption. It can be also noticed from Fig. 97 that ε_E=1mm under the teeth where there are no PMs, whereas ε_E=2mm under the tooth equipped with PMs. Considering the above, the equivalent permeability function shown in Fig. 98 can be finally determined using (26).

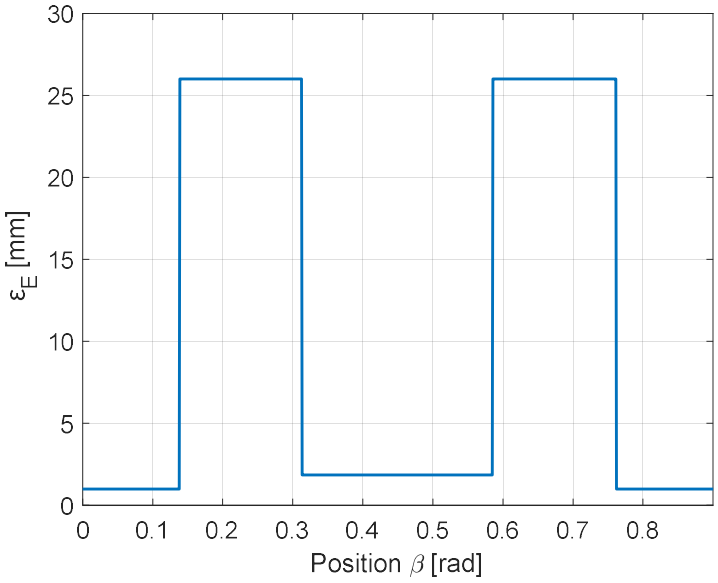

Fig. 97. Equivalent thickness function under one pole pair.

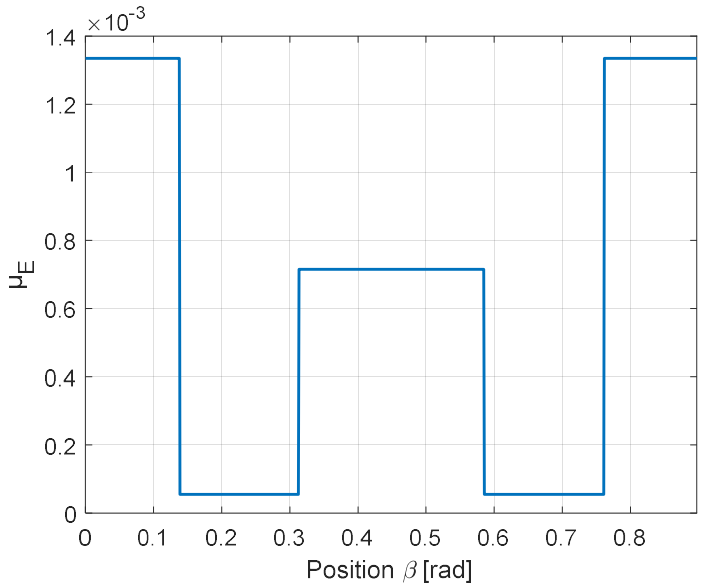

Fig. 98. Equivalent permeability function under one pole pair.

Concerning the other quantity involved in (26), i.e. $\overline{N_E}$, one of its element is shown in Fig. 99. In particular, the phase A WF and EWF determined as in (28) are plotted in continuous and dashed lines, respectively. The WF highlights the number of turns per slot (y-axis) and the position of the groups of active sides (x-axis). The WFs and EWFs of phases B and C are shifted by 2/3π and 4/3π electrical radians, respectively, with respect to those of phase A. The EWF of the field winding is also determined as in (28), considering the features highlighted in Table XXXIX and Fig. 96.

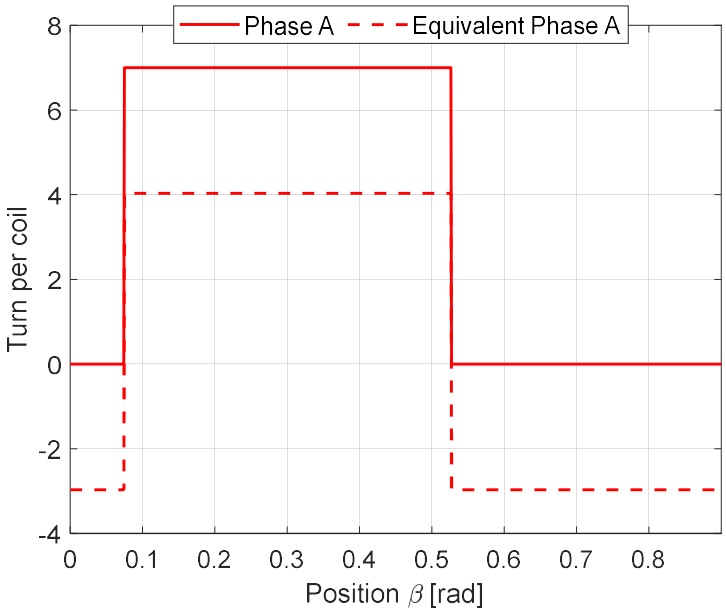

Fig. 99. WF and EWF of rotor phase A under one pole pair.

Having calculated $\mu_E(\beta,\gamma)$ and all the 4 EWFs contained in $\overline{N_E}$ (3 for the rotor phases and 1 for the field winding), all the machine inductances can be determined. The self-inductance of phase A and the mutual-inductance between phases A and B are plotted in Fig. 100, showing the effect of stator slots and magnets. The mean values of these 2 inductances, namely L and M, will be used in (25) for the evaluation of the commutation angle and thus of the phase current waveforms. For the sake of completeness, the mutual inductance between phase A and the stator excitation winding is shown in Fig. 101.

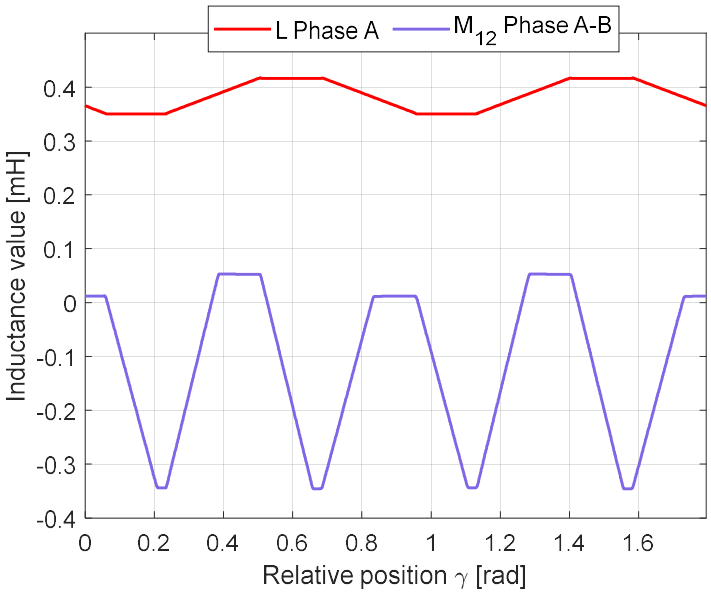

Fig. 100. Self-inductance of phase A and mutual-inductance between phases A and B as function of γ.

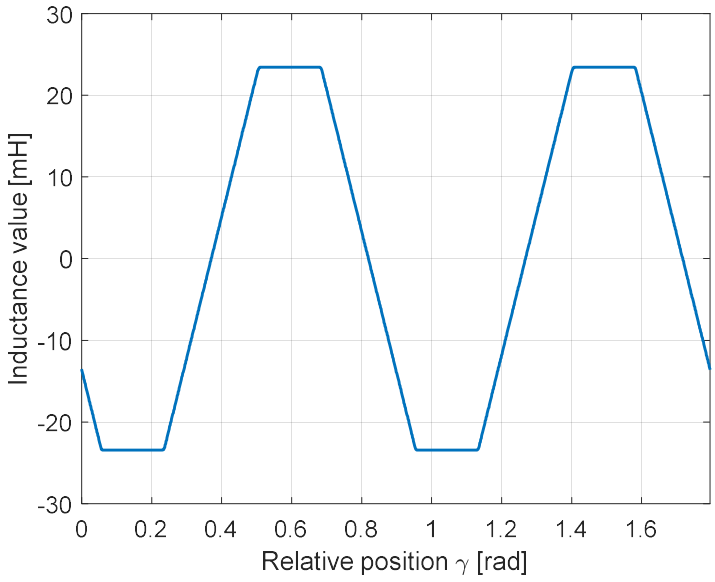

Fig. 101. Mutual-inductance between phase A and excitation winding as a function of γ.

D. Commutation angle

Using the results from Section 8.1.3.C, the commutation angle θ can be determined using (25). The exciter excitation current I_{F_EXC} is set according to the loading of the main WFSG. The considered loadings are 0kVA (no-load operation of the generator), 100kVA and 200kVA and the corresponding field current values I_L of the main WFSG are selected accordingly. These values obviously correspond to the amplitudes of the trapezoidal exciter armature current waveforms. The relevant results are summarized in Table XLI where, for each investigated loading, the values of I_{F_EXC}, I_L and θ are reported.

The results obtained from the analytical model, including no-load and on-load voltages and armature current waveforms, will be shown in Section 8.1.5. and compared against corresponding FE and experimental evaluations, aiming to prove the effectiveness of the proposed approach. Before showing the comparative analyses, the FE model and the experimental tests will be described in the next section.

Table XLI
ANALYTICAL RESULTS FOR THE COMMUTATION ANGLE Θ AT DIFFERENT LOADING CONDITIONS OF THE MAIN WFSG

Main WFSG Loading [kVA]	**θ [°]**	**I_{F_EXC} [A]**	**I_L [A]**
0	47.5	0.23	14.68
100	50.4	0.61	21.7
200	60	0.9	30.7

8.1.4 Validation Tools

The validation tools used in this work are a FE model and an experimental test campaign of the hybrid exciter. The full description of the built FE-model can be found in [85], where the hybrid excitation concept is fully validated against experimental results. However, both the FE and experimental tools are briefly recalled in this section for the sake of clarity.

A. FE model

For a fair comparison between analytical and FE results, the latter is implemented considering the 2D aspects only, whose computation burden is reduced compared to a full 3D analysis. The 2D FE model of the exciter under analysis has already

been shown in Fig. 96, where the details relative to the windings can be also observed. Thanks to the geometrical symmetry, only 1/7-th of the whole machine is simulated to reduce the simulation time. Concerning the electrical circuit coupled to the developed 2D FE model, the one reported in Fig. 93 is replicated for the armature winding, whereas for the field winding a DC current source is used to feed it.

B. Experimental testing

A prototype of the hybrid exciter was realized to investigate its operating behaviour and to validate the FE-model results. All the information on the experimental setup and tests are exhaustively reported in [85]. In short, three types of tests are used for validating the proposed analytical tool. These are:

1) The no-load operation of the exciter.
2) The no-load operation of the main generator.
3) The on-load operation of the main generator.

During the no-load operation of the exciter, the field winding of the main WFSG is disconnected from the rotating rectifier. The exciter field current is either set to zero, meaning that only the PMs produce the main flux in the air-gap, or equal to a positive value. The rotational speed is at its rated value of 1500 rpm. In these conditions, the line-to-line armature voltages are measured.

The no-load operation of the main generator is achieved by leaving its armature winding open, whereas its field winding is connected to the rotating rectifier. In these conditions, a certain current flows in both the armature winding of the exciter and the field winding of the generator. Also in the exciter field winding the current is not null and its value is such that the rated voltage is achieved at the main machine stator terminals. The exciter line-to-line voltages and the rectified voltage and current are measured.

The third type of test consists in loading the WFSG. This means that its armature winding is not open-circuited but is connected to the laboratory mains, while the rotating parts rotate at 1500 rpm. Besides the quantities measured in the previous type of tests, the output power, currents and voltages of the main machine are recorded.

C. Validation of the Proposed Analytical Model

The most relevant quantities for the sake of this study are the exciter armature current and voltage waveforms, as these both depend on the commutation angle significantly. In fact, on one hand the commutation angle makes the currents featuring a trapezoidal trend as described in Section 8.1.2.A and, on the other hand, it has a significant impact on the available rectified voltage. Therefore, in this section, the comparison focuses on the exciter armature current and voltage waveforms and their relevant amplitude spectra. While it is clear how the trapezoidal current waveforms are obtained, the exciter voltages are calculated using (30), where R is a diagonal 4x4 matrix containing the exciter field and armature resistance values, while L(γ) is the inductance matrix calculated through (26). The vector $\bar{\imath}$ is the vector containing the DC field current and the trapezoidal armature currents of the exciter, which are found analytically using the values of θ listed in Table XLI, without the need for a numerical solution. On the other hand, (30) can be also used to analyse transient operations of the exciter. In this case, the currents in $\bar{\imath}$ should be considered as state variables and, as such, should be calculated using a numerical solver [100].

$$\bar{v} = R\bar{\imath} + \left(\frac{\delta L(\gamma)}{\delta \gamma}\bar{\imath}\right)\frac{d\gamma}{dt} + L(\gamma)\frac{d\bar{\imath}}{dt} \tag{30}$$

1. No-load operation of the exciter

The no-load operation of the exciter is analyzed under two conditions: 1) only the PMs contribution is considered, i.e. the field current I_{F_EXC} is null; 2) I_{F_EXC} = 0.23A, which is the current value needed to achieve the rated armature voltage of the main WFSG. The comparison in terms of line-to-line voltages waveforms and harmonic spectra is shown in Fig. 102 for the case 1) and in Fig. 103 for the case 2).

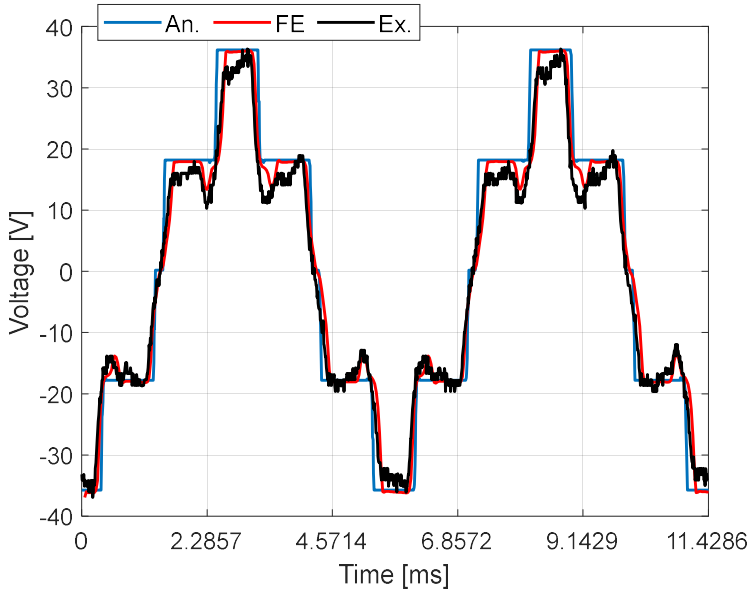

a)

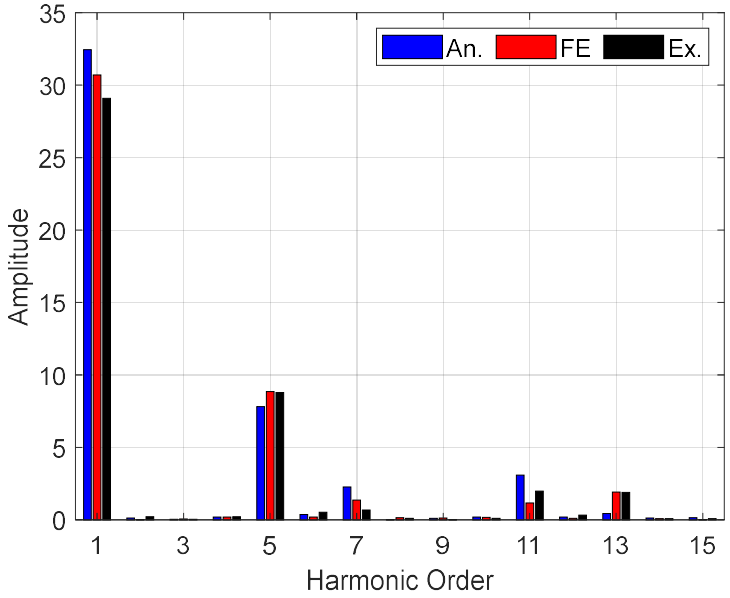

b)

Fig. 102. Comparison between analytical, FE and experimental line-to-line voltage waveforms of the exciter at rated speed (1500 rpm) and with null field current: a) waveforms, b) spectra.

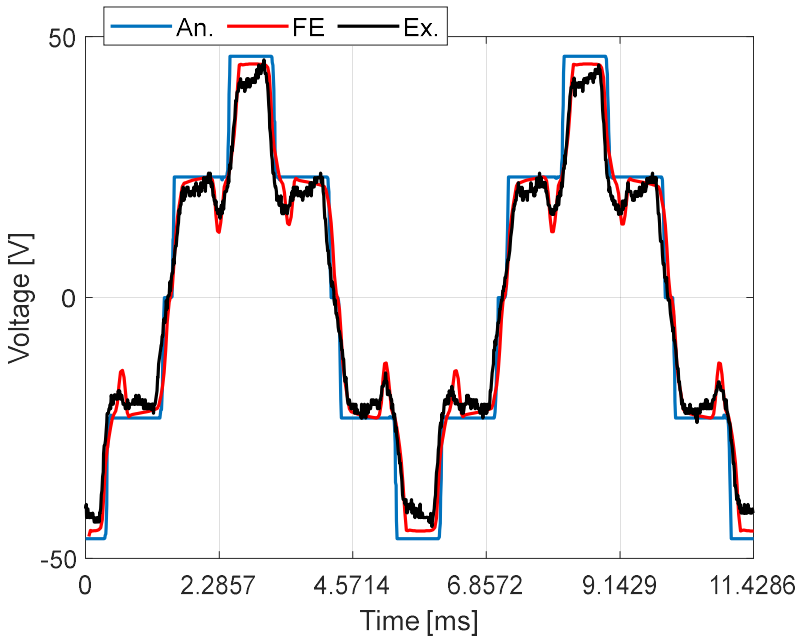

a)

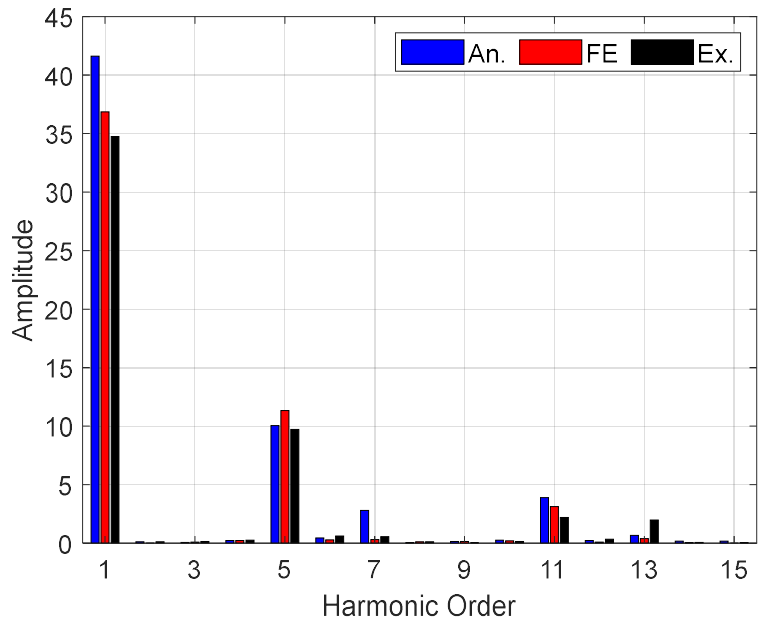

b)

Fig. 103. Comparison between analytical, FE and experimental line-to-line voltage waveforms of the exciter at rated speed (1500 rpm) and with the field current equal to 0.23A: a) waveforms, b) spectra.

Overall, the main phenomena are very well predicted. The main discrepancies relate to a) the fundamental harmonic, with an overestimation registered for the analytical model, probably due to the assumption of linear behavior of the ferromagnetic materials; b) the high-frequency effects, such as the rotor slotting ones, which are neglected in the analytical model. Furthermore, also any

difference between the declared materials' properties used in the analytical and FE tools and those actually in place for the prototype can cause divergence.

It is worth highlighting that, at this stage, the commutation angle does not play any role since the exciter is operating at no-load and the armature currents are set to zero.

2. On-load operation of the exciter

To comprehensively validate the presented analytical model is therefore necessary to include the effects of the exciter armature reaction in (30). This is done by considering the loaded operations reported in Table XLI, where 0kVA represents the no-load operation of the main generator, while the exciter is loaded and is providing current to the WFSG field winding.

First, using the values of θ reported in Table XLI, the analytical exciter current waveforms are obtained for the 3 investigated loaded conditions. These are then compared against the corresponding FE results, as shown in Fig. 104.

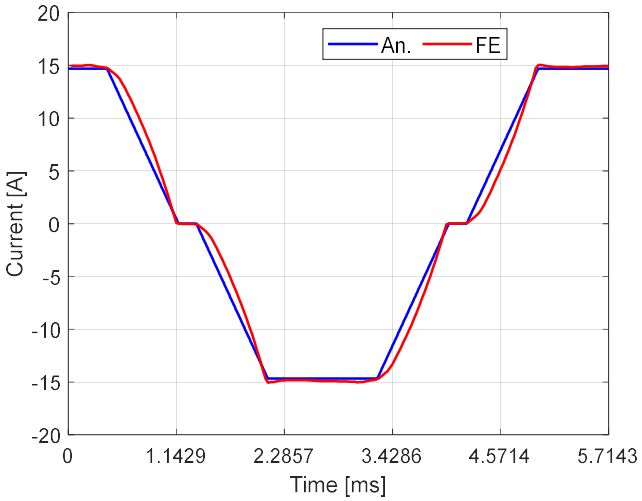

a)

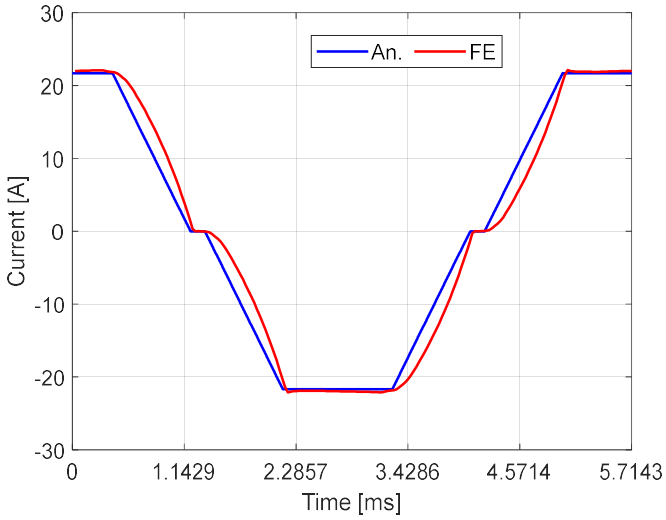

b)

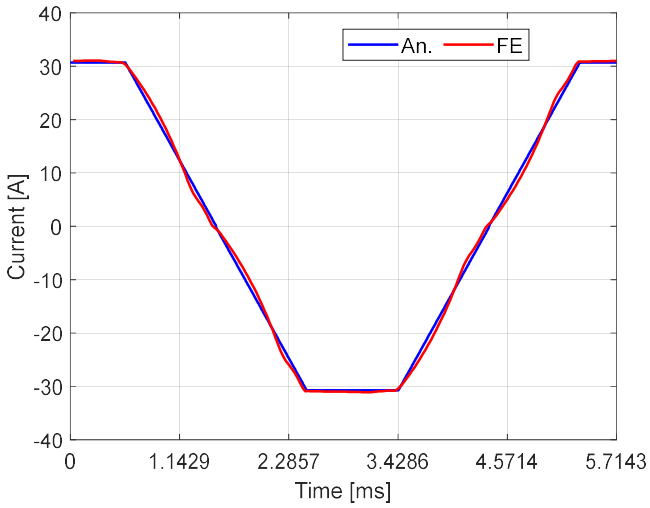

c)

Fig. 104. Comparison between analytical and FE exciter armature current waveforms at rated speed (1500rpm) at on-load operation of the exciter, while the generator is providing a) 0kVA b) 100kVA c) 200kVA.

The experimental current waveforms are not available, but the rectified DC currents recorded during testing perfectly match the maximum current values obtained through the analytical and FE models. Moreover, being the commutation angle a key parameter also for the line-to-line voltages, it can be safely concluded that, if the experimental line-to-line voltages were well predicted by the analytical results, then the experimental commutation angle would match that resulting from the models. The results of Fig. 104 prove a very good estimation of the commutation angle θ at any operating condition. Some discrepancies can be noted,

though, in the rising and the descendant parts of the waveform, which are not fully trapezoidal in the reality.

The analytical, numerical and experimental exciter line-to-line voltage waveforms and their relevant spectra are compared in Fig. 105, Fig. 106 and Fig. 107, respectively for the 0kVA, 100kVA and 200kVA loaded conditions. Although some discrepancies are observed in the waveforms and their spectra, overall the match is very good at any operating condition. This is especially true if one refers to the voltages rectified by the diode bridge, which however are not shown here since their footprint can be directly inferred from the line-to-line voltages of Fig. 105-Fig. 107. The rectified voltage available at the WFSG rotor terminals is in fact the most important quantity to predict for exciters of WFSGs during normal operating conditions. In conclusion, thanks to an accurate estimation of the commutation angle, it becomes possible to predict via a purely analytical way the rectified voltages and currents in conventional generating sets equipping brushless exciters.

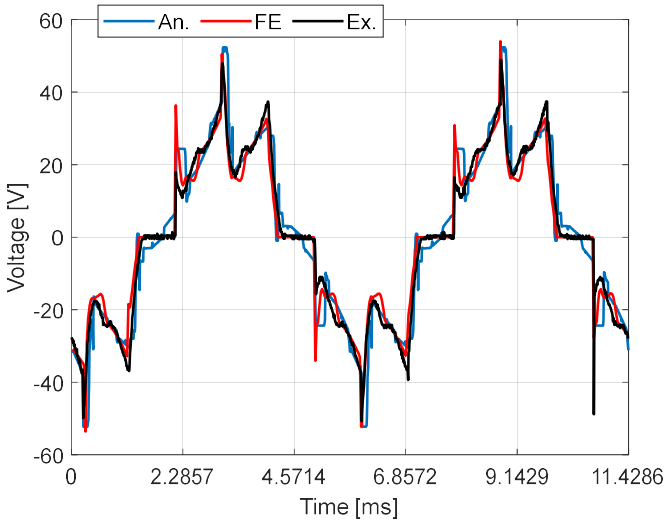

a)

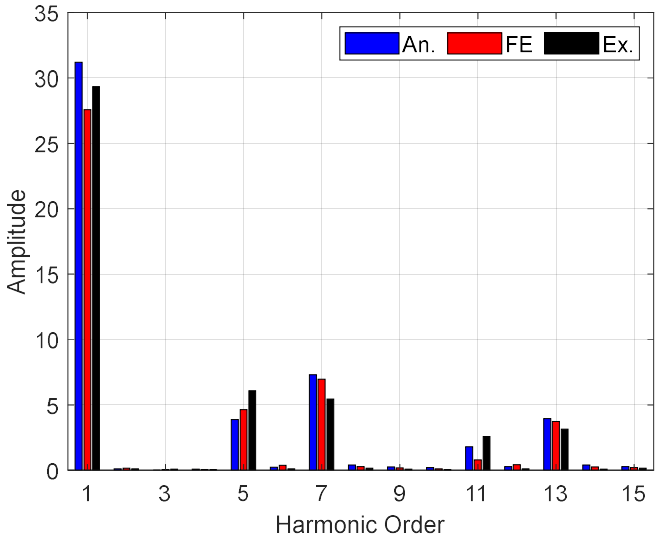

b)

Fig. 105. Comparison between analytical, FE and experimental exciter line-to-line voltages at rated speed (1500rpm) and at no-load operation of the main generator (0kVA): a) waveforms and b) spectra.

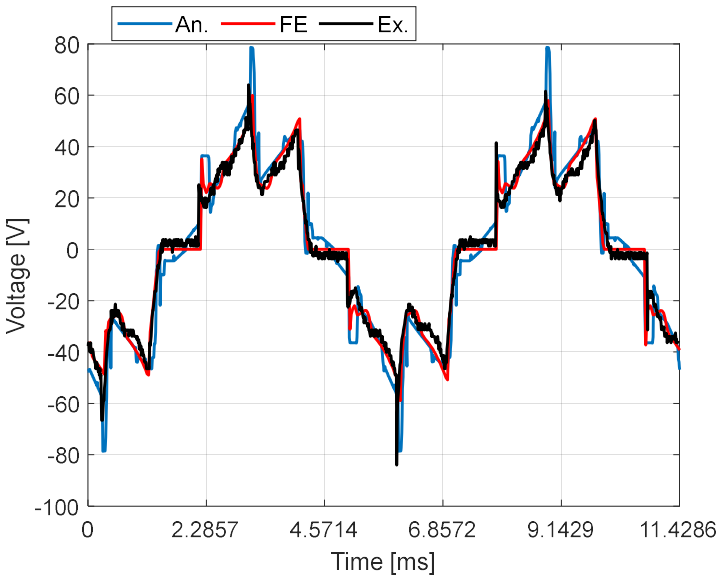

a)

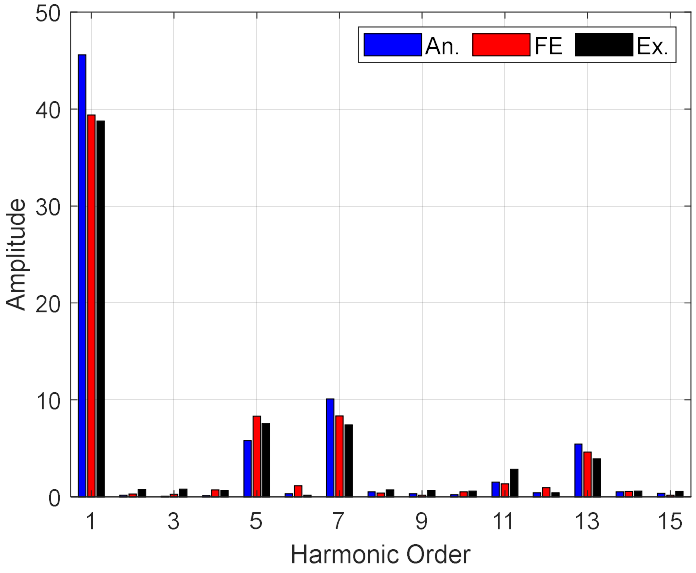

b)

Fig. 106. Comparison between analytical, FE and experimental exciter line-to-line voltages at rated speed (1500rpm) and at on-load operation of the main generator (100kVA): a) waveforms and b) spectra.

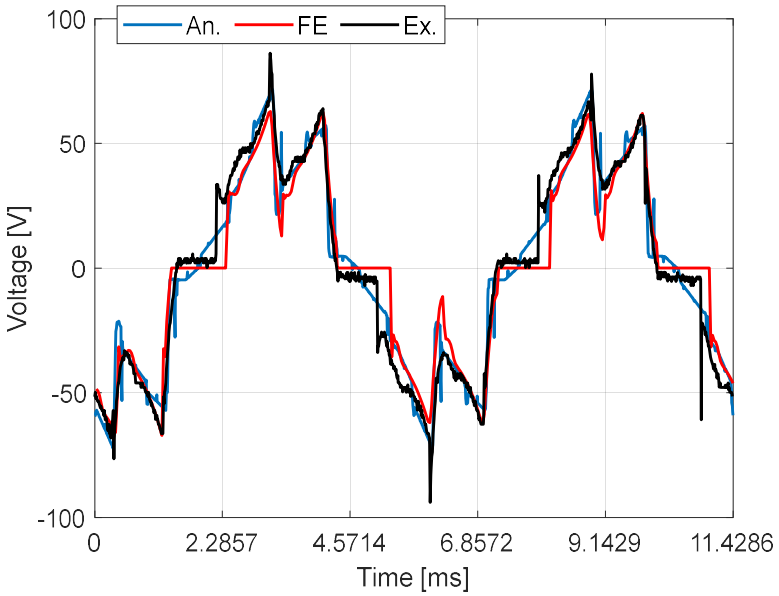

a)

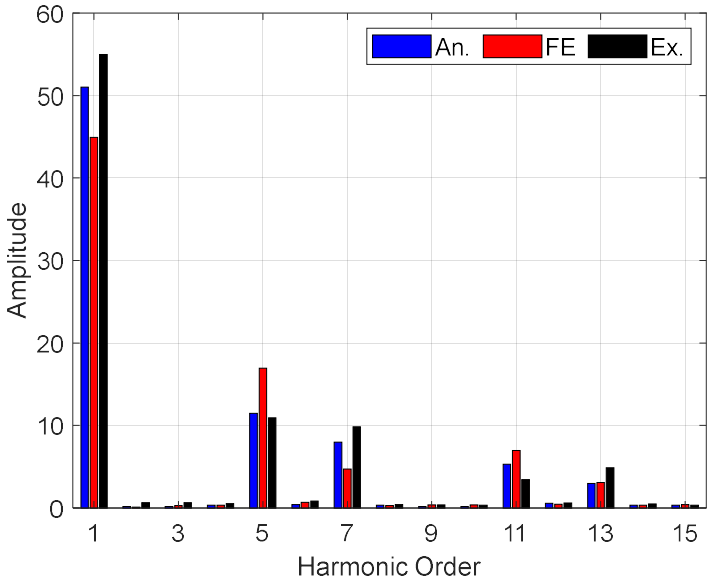

b)

Fig. 107. Comparison between analytical, FE and experimental exciter line-to-line voltages at rated speed (1500rpm) and at on-load operation of the main generator (200kVA): a) waveforms and b) spectra.

8.1.5 Discussion

The key advantage of using a fully analytical model which does not rely upon numerical analyses for the evaluation of some key quantities is the resolution speed. Specifically, the obtained computation time reduction is more than 80% compared to the FE method, using a processor Intel(R) Core(TM) i7-8700K CPU @ 3.70GHz 3.70 GHz. For the sake of completeness, the resolution speed of the proposed approach is also compared against the methodology in [90], where the permeability function is calculated using FE analyses and the system (26) is solved in Matlab Simulink. The obtained computation time reduction is ≈50% in this case. While the above significant improvements in resolution speed have been evaluated on a single machine design, i.e. the hybrid-excited CP exciter at hand, it is clear that further computation time reductions would be achieved when optimization processes were set up, as several design solutions need to be investigated. Therefore, the proposed analytical methodology can represent a powerful means for the manufacturers of generating sets to optimally design brushless exciters of WFSGs, which are still rather roughly sized (and often over-sized) in an industrial environment. In fact, this design approach is no longer acceptable in certain applications, especially in transport where weight and volume are extremely sensitive parameters.

The model is built aiming to maximize its simplicity, while keeping the accuracy as high as possible. Hence, the presented analytical approach neglects some "secondary" phenomena that, depending on the machine operating condition, can lead to more or less relevant errors. Furthermore, it assumes a linear behaviour of the ferromagnetic materials, i.e. saturation is neglected, which could somewhat compromise the accuracy. However, exciters usually operate in linear conditions when the main machine works during normal operating scenarios [82] Therefore, there is no need to add complications to the model that, despite the simplifications, showed an excellent match against FE and experimental results.

One of the key points of this model is that it does not need a numerical analysis neither for the permeability function evaluation nor for the solution of the dynamic model (30) which uses the currents as state variables. This is enabled by the use of simplified functions for the stator and rotor profiles as well as by an accurate estimation of the commutation angle, which in turn allows defining the shape of currents.

Another important aspect to mention is that the model can be easily adapted to investigate anomalous operating scenarios of the exciter, such as overloads or transients. For example, saturation factors and/or dynamic models can be envisioned for such purposes. However, the inclusion of such measures would require FE calibrations and/or numerical resolutions and, therefore, goes beyond the scope of this work, leveraging on the fact that exciters of WFSGs operate under normal loads for the great majority of their lifetime.

8.1.6 Conclusions

This chapter proposes a purely analytical model for the prediction of the electromagnetic behaviour of a brushless exciter with hybrid excitation, taking into account the effect of the commutation processes occurring in the rotating diode rectifier on the output rectified voltage.

The first part of the work introduces the analytical model, based on an equivalent circuit approach, for the calculation of the matrix inductance. This is found using simplified equivalent functions for the description of the machine phases as well as of the geometrical aspects, The key point is that these functions are determined without resorting to FE investigations, while not compromising the accuracy. Then, self- and mutual-inductances are used in the equations derived for the commutation angle evaluation, which is the basis of the proposed method as it

allows to estimate the real exciter's armature current waveforms. This, in turn, eliminates the inaccuracies deriving from a sinusoidal approximation or the need for dynamic models requiring a numerical resolution. Finally, FE and experimental results are used to validate the analytical findings, at both no-load and on-load operations of the exciter and, consequently, of the main generator. Despite the complexity of the phenomena involved in a generating set system, the comparative analyses showed an excellent match.

The main contribution of this model is that it is fully released from any numerical computation, making it simple, fast and accurate. Therefore, the proposed analytical approach enables improved design methodologies for this often-overlooked electrical machine. In this context future works will be oriented towards the minimization of the voltage drop ensuing from the diodes' commutation process, which will be achieved by setting up optimization procedures based on this purely analytical method.

8.1.7 Chapter's Closing Remarks

In this chapter, a mathematical model aimed at predicting the performance of a hybrid excitation system of WRSMs was developed. In particular, the voltage reductions due to uncontrolled commutation in the diode rectifiers of brushless excitation systems was studied. This work, while diverging from the primary focus on RE material reduction in electric motor design, addresses the performance of an electric machine whose use, in combination with a main WRSM, is intended for power generation on board of aircraft and/or ships.

While the previous chapters focused on propulsion systems without addressing the excitation aspect, this chapter broadens the scope by considering a complementary, yet distinct challenge in electric machine design. The insights gained here are not only applicable to traditional sectors like energy, but also hold potential relevance for aerospace and marine systems, where similar excitation technologies could be utilized.

By integrating this study into the broader context of the thesis, we complete the examination of sustainable electric machine solutions, encompassing both the motors and their control systems. This holistic approach enhances the robustness of the proposed innovations and lays a stronger foundation for future research and development in this field.

9. CONCLUSIONS

9.1 General Conclusions

9.1.1 General Considerations

The research presented in this thesis has demonstrated the potential to innovate within the field of electric motor design by significantly reducing or eliminating the use of RE materials. This effort is driven by the need to address the environmental, economic, and geopolitical challenges associated with the extraction and processing of these materials. The findings suggest that it is feasible to achieve high performance, efficiency, and reliability in electric motors using alternative materials (to PMs) and design methodologies.

The overarching conclusion is that the transition to more sustainable electric motor technologies is feasible and necessary to support the broader goals of environmental sustainability and resource efficiency. The research has highlighted the importance of rethinking conventional motor design paradigms, integrating sustainability as a core criterion alongside traditional performance metrics such as power density and torque output.

9.1.2 Implications for the Industry

The implications of this research are profound for various sectors, including automotive, mining, and aerospace. The adoption of electric motor technologies that minimize reliance on RE materials can lead to several benefits:

- Reduced Environmental Impact: By decreasing the dependency on RE elements, which have a significant environmental footprint due to mining and refining processes, industries can lower their ecological impact and contribute to global sustainability targets.
- Economic Viability: The shift towards more abundant and less expensive materials can reduce costs in the long term, particularly as demand for electric vehicles and machinery continues to grow.
- Geopolitical Stability: Diversifying the material base for electric motors reduces the reliance on specific regions for RE supply, thus enhancing the resilience of supply chains and mitigating geopolitical risks.

9.1.3 The Path Forward for Sustainable Electric Motor Technologies

The research underscores the necessity of a multifaceted approach to electric motor design that encompasses technical optimization, lifecycle considerations, economic feasibility, and scalability. Future advancements should focus on:

- Integrated Design Methodologies: Developing comprehensive design frameworks that balance performance, sustainability, and cost-effectiveness across various applications.
- Enhanced Simulation and Testing Techniques: Utilizing advanced simulation tools to predict long-term performance and environmental impact more accurately, complemented by rigorous experimental validation.
- Cross-Sector Collaboration: Fostering collaboration between academia, industry, and policymakers to accelerate the development and adoption of sustainable motor technologies.

9.1.4 Challenges and Opportunities

While the research has demonstrated promising avenues for the reduction of RE materials, several challenges remain:

- Material Innovation: The development of new materials that can match or exceed the performance of traditional RE magnets without the associated environmental and economic costs remains a critical challenge.
- Manufacturing Processes: Scaling up the production of motors using alternative materials requires innovation in manufacturing techniques to maintain quality and reduce costs.
- Market Adoption: For sustainable motor technologies to become mainstream, there needs to be greater alignment between technological innovation, market readiness, and regulatory support.

These challenges also present opportunities for further research and development, as overcoming them will pave the way for the widespread adoption of sustainable motor technologies.

9.1.5 Final Observations

The journey towards a more sustainable and resilient future in electric motor technology is complex and requires a rethinking of traditional approaches. This thesis has laid the groundwork for understanding how innovative design and material strategies can contribute to this transition. However, it is clear that achieving global sustainability goals will require continued efforts, collaboration, and a commitment to integrating environmental considerations into every aspect of motor development and application.

In conclusion, the research has made a significant contribution to the field, providing a clear path forward for the development of next-generation electric motors that are high-performing and aligned with the principles of sustainability and resource efficiency. This vision, if realized, will play a crucial role in supporting the global shift towards a more sustainable industrial ecosystem.

9.2 Contribution to Research

This thesis provides a substantial contribution to the field of electric propulsion systems by focusing on the development of sustainable motor technologies that minimize or eliminate the use of RE materials. Each work presented in this research tackles specific challenges in different sectors, offering different solutions for enhancing electric motor performance while reducing environmental impact. Below is an exploration of each contribution [1]-[9] following the thesis presentation order.

- Trends and Roles of Electric Motors towards Sustainable Automotive Systems [8]

This work explores the evolution and impact of electric motor technologies within the automotive industry, specifically emphasizing their role in enhancing vehicle performance while advancing sustainable mobility. It provides an extensive analysis of how electric motors have been adapted across different vehicle categories, from compact urban cars to high-performance hypercars and heavy-duty trucks.

The contribution highlights the increasing importance of eliminating RE materials due to environmental concerns and fluctuating material costs. As a response to these challenges, various motor topologies are discussed, including WRSM and

IPMs, both of which have shown potential to reduce or eliminate the need for RE elements.

Through several case studies, the work showcases how electric motors are tailored to meet the specific performance requirements of different vehicle types. For example, the research examines how city cars prioritize cost-effective, energy-efficient solutions, while high-end luxury vehicles employ sophisticated multi-motor configurations to achieve unparalleled performance. Heavy-duty trucks are another focus, where the demand for high torque at low speeds has driven the development of more robust motor solutions. By examining these trends, this contribution sets the stage for future developments in the electrification of vehicles, ultimately pushing the boundaries of sustainable motor design and application.

- Design of the Propulsion System for a Formula SAE Racing Car Based on a Brushless Motor [9]

This work contributes to sustainable motorsport by designing an efficient, cost-effective propulsion system for a Formula SAE racing car using a brushless motor. With the FSAE competition increasingly embracing electric propulsion, this research aims to develop a high-performance, low-budget electric drive tailored to meet competition constraints while maintaining competitive edge.

A central contribution of this study is the identification and implementation of a two-motor layout mounted on the rear axle, selected as an optimal balance between performance and cost-efficiency. This configuration allows for a streamlined design without the complexity and expense of a four-motor setup while still enhancing rear traction and minimizing mechanical transmission needs. The system's architecture includes a planetary gear for torque management, thus enabling a reduction in motor size and weight, both critical factors for high-speed racing.

The motor selection process, driven by data from past competitions, focuses on achieving high power density with minimal weight. This work applies both analytical sizing and FE validation, ultimately refining the motor to a compact, 20 kg design that produces 30 Nm of torque up to 12,730 rpm. A double-layer winding layout, introduced during refinement, reduces torque ripple and improves waveform quality, ensuring smooth operation during dynamic racing conditions.

In addition to achieving optimal design for Formula SAE, this study establishes a foundational procedure for identifying the optimal torque-speed characteristics of motors tailored to specific performance requirements. This methodological approach can be generalized and adapted for other applications, making it a valuable model for a wide range of electric vehicle and propulsion system designs. By focusing on both economic and performance constraints, this research successfully develops a propulsion system that aligns with Formula SAE's regulatory framework and competitive standards, offering a high-density, sustainable electric solution suitable for student-led racing applications.

- Multi-Physics and Multi-Objective Optimization of a Permanent Magnet-Assisted Synchronous Reluctance Machine for Traction Applications [3]

This study presents a comprehensive multi-objective optimization framework for designing a PMa-SynR machine specifically for traction applications. The key focus of this work is balancing multiple conflicting objectives, including minimizing torque ripple, reducing structural stress, and maximizing torque output.

A critical contribution of this research is the development of a FE model that allows for simultaneous consideration of electromagnetic and mechanical properties. By optimizing rotor geometry, magnet placement, and flux barrier shapes, the project achieves a 15.1% reduction in torque ripple, which is crucial for enhancing the smoothness of motor operation in traction systems.

In addition to the improved torque ripple, the work ensures that the mechanical stresses in the motor are kept within safe limits, making the design both high-performing and durable for real-world applications. This multi-objective optimization method can serve as a benchmark for the future development of electric motors that do not rely on RE elements, making significant strides towards more sustainable electric motor technologies.

- Combined Magnet Shaping and Asymmetries in Surface-Mounted Permanent Magnet Machines for Improved Torque Performance [1]

This contribution delves into the simultaneous use of magnet shaping and asymmetry in SPM machines to improve their torque performance. The project focuses on addressing one of the most common challenges in SPM machines,

torque ripple, which can lead to mechanical vibrations and noise, reducing motor efficiency and reliability.

By developing a detailed 2D-FE model, the study demonstrates that combining asymmetry in rotor design with unconventional magnet shaping can significantly reduce torque ripple without sacrificing overall motor performance. This is particularly valuable in high-performance applications like electric racing cars, where smooth operation is necessary.

One of the key insights from this work is the effectiveness of combining these two techniques, which have previously been explored separately in the literature but never integrated in this way. The result is a motor design that offers enhanced performance, particularly in applications requiring high precision and smooth torque delivery. This work provides a practical framework for improving the design of electric motors used in both automotive and industrial sectors, where performance and operational smoothness are critical.

- Rare Earth Materials Reduction in a Hypercar Propulsion System [2]

This study focuses on reducing the reliance on RE materials in hypercar propulsion systems, presenting a new approach to motor design. The work involves the reconfiguration of an IPM motor originally designed for the rear axle of a hypercar, adapting it for the front axle while minimizing the use of RE elements.

The main contribution of this project is the 45.5% reduction in RE material usage achieved through a combination of axial length adjustments and the strategic rearrangement of magnets over a conventional solution. This reduction is particularly impressive given the high torque and performance requirements of hypercars, which typically rely on RE elements for their exceptional magnetic properties.

FE analyses were conducted to compare different configurations, exploring both ferrite and RE magnets. The results show that it is possible to maintain high levels of torque density and efficiency while significantly reducing the use of RE materials. Additionally, the study highlights how structural and vibrational analyses can be integrated into motor design to ensure that the new configurations are both mechanically sound and optimized for performance. This contribution is a valuable step towards more sustainable electric motor technologies, especially in the high-performance automotive sector.

- Wound Rotor Synchronous Motor Design for a Mining Application [4]

This contribution presents the design of a WRSM as a sustainable alternative to IPM motors in mining truck propulsion systems. Mining trucks require motors capable of delivering high torque and operating reliably under harsh conditions, making them an ideal candidate for the implementation of WRSM technology.

Through a combination of electromagnetic, thermal, and structural analyses, the research demonstrates that WRSMs can meet the high-performance demands of mining trucks while completely eliminating the need for RE materials.

By maintaining a high torque output and ensuring that the motor operates efficiently even at low speeds, the work confirms the feasibility of WRSMs in this application. Furthermore, the research highlights the scalability of WRSM technology, showing that it can be applied to other heavy-duty vehicles beyond the mining sector. This contribution advances the field of sustainable motor design and provides solutions for industries seeking to reduce their environmental footprint.

- Design Optimization of a Starter Generator for More Sustainable High Power Density Aerospace Applications [5]

In this study, the focus shifts to the aerospace sector, where the design and optimization of high-power density starter-generators are critical for ensuring both performance and sustainability. This work contributes to the development of a SPM motor for fixed-speed starter-generator applications, with a focus on minimizing the use of copper and RE materials.

The research achieves good performance metrics, including a power density exceeding 2.3 kW/kg and an efficiency of 98%. These results are particularly significant in the aerospace industry, where reducing weight and maximizing efficiency are crucial for improving fuel efficiency and reducing emissions.

One of the key points in this project is the integration of environmental sustainability into the design process. By carefully selecting materials and optimizing thermal performance, the study demonstrates that high-performance electric motors can be designed with sustainability in mind, making it a valuable contribution to the ongoing efforts to create more environmentally friendly aerospace technologies.

- A Simplified Analytical Approach for Hybrid Exciters of Wound-Field Generators [6]

The final contribution of this thesis involves the development of an innovative analytical model for hybrid exciters in wound-field generators, which are widely used in mid-power applications such as naval ships and industrial power systems. This work simplifies the analysis of the diode commutation processes in these exciters, offering a faster and more efficient method for evaluating system performance.

By eliminating the need for complex numerical simulations, the proposed model allows for quicker design iterations while maintaining a high level of accuracy. The research validates the model through both FE analysis and experimental testing, ensuring that the results are reliable and applicable to real-world scenarios. This contribution is particularly valuable for the design of brushless excitation systems in wound-field generators, where efficiency, reliability, and performance are critical. By providing a simpler yet accurate analytical approach, this work offers practical tools for engineers working in design of electrical machines.

An additional contribution to research, not included in the thesis as it falls outside its primary topic but remains complementary for understanding and managing phenomena related to electric machines, is provided as follows:

- Optimal Sizing of Hairpin Conductors in Highway Operation with PWM Power Supply [7]

This work provides an advancement in understanding and reducing AC losses in hairpin windings for high-frequency operations, a critical challenge in the design of electric drives. By specifically targeting the high losses associated PWM supplies at highway speeds, the study focuses on optimizing hairpin conductor dimensions for efficient IPMs used in EV applications.

A major contribution of this research lies in the development of an optimized methodology for HW sizing under real-world driving conditions. Using the ARTEMIS drive cycle, which closely reflects European highway operations, the study assesses the harmonic content of currents generated by a PWM supply. The work's approach involves evaluating conductor losses under a broader frequency

range, providing an accurate assessment of HW performance under high-speed, high-frequency conditions.

The research employs both analytical and FE method to calculate and compare losses in different HW configurations. The optimized conductor layout identified in this study shows a considerable reduction in AC losses, approximately halving losses at 1 kHz when compared to benchmark hairpin winding configurations. This improvement is particularly notable at higher frequencies, which are less favourable for conventional hairpin windings. By refining conductor cross-sections to better suit high-speed conditions, the work achieves a 34.2% reduction in losses during peak-speed PWM operation, effectively enhancing motor efficiency and vehicle range.

The results demonstrate that careful conductor sizing, tailored specifically to the drive cycle's average velocity, allows for substantial improvements in EV powertrain efficiency. This work sets a precedent for future studies on hairpin winding optimization, underscoring the importance of dimensioning frequency selection in designing high-performance, sustainable electric drive systems for transportation.

9.3 Future Works

This section outlines the next steps necessary to consolidate the research conducted during the doctoral study. As highlighted in the previous sections, the construction of prototypes is essential to validate the engineering concepts and designs presented, particularly concerning the electric motor systems discussed throughout the thesis. Below is a summary of the ongoing or planned activities aimed at achieving these objectives.

- FSAE Electric Vehicle – Modena

The motor designed and presented in section 5.2 has been selected as the propulsion system for the future electric FSAE vehicle developed by the University of Modena and Reggio Emilia's team. This collaboration between my team (Melting Lab) and the mechanical engineers' team will focus on designing and developing the transmission system and analysing the propulsion system from a vibro-acoustic standpoint. This involves building a prototype of the motor from [2], which will be adapted in terms of length and active parts to meet the performance requirements. Once tested electromagnetically, thermally,

mechanically, vibrationally, and acoustically, this motor will become a crucial component of the FSAE vehicle.

- Wound Rotor Synchronous Motor Prototyping – Nottingham

As presented in subsection 3.2.2.B, a WRSM has been designed and analysed electromagnetically, thermally, and structurally using FE software. This project is part of a collaboration between the University of Modena and Reggio Emilia, the University of Nottingham (UK), and a UK-based company. The prototype has been manufactured in China and delivered to the UK for testing. These validation tests are expected to take place in the coming months.

- Starter/Generator Development – Malta

The starter/generator project presented in Chapter 7 arises from the collaboration between the University of Modena and Reggio Emilia and the University of Malta, where I completed my abroad research period. This project includes the development of a prototype and subsequent testing at the facilities in Modena. The next phase will involve adapting the project to integrate embedded power electronics.

REFERENCES

[1] G. Devito, S. Nuzzo, D. Barater, M. Soltani and G. Franceschini, "Combined Magnet Shaping and Asymmetries in Surface-Mounted Permanent Magnet Machines for Improved Torque Performance," 2022 International Conference on Electrical Machines (ICEM), Valencia, Spain, 2022, pp. 855-861, doi: 10.1109/ICEM51905.2022.9910726.

[2] G. Devito, F. Puglisi, D. Barater, S. Nuzzo, M. Giacalone and G. Franceschini, "Rare earth Materials Reduction in a Hypercar Propulsion System," 2023 AEIT International Conference on Electrical and Electronic Technologies for Automotive (AEIT AUTOMOTIVE), Modena, Italy, 2023, pp. 1-6, doi: 10.23919/AEITAUTOMOTIVE58986.2023.10217247.

[3] Puglisi F, Barbieri SG, Mantovani S, Devito G, Nuzzo S. “Multi-physics and multi-objective optimization of a permanent magnet-assisted synchronous reluctance machine for traction applications.” Proceedings of the Institution of Mechanical Engineers, Part C: Journal of Mechanical Engineering Science. 2024;0(0). doi:10.1177/09544062241240888.

[4] G. Devito et al., "Wound Rotor Synchronous Motor Design for a Mining Application," 2024 International Conference on Electrical Machines (ICEM), Torino, Italy, 2024, pp. 1-7, doi: 10.1109/ICEM60801.2024.10700511.

[5] G. Devito, D. Barater, A. Theofanous, S. Nuzzo, and M. Galea, "Design Optimization of a Starter Generator for More Sustainable High Power Density Aerospace Applications,", Accepted for IECON 2024.

[6] G. Devito, S. Nuzzo, D. Barater and G. Franceschini, "A Simplified Analytical Approach for Hybrid Exciters of Wound-Field Generators," in IEEE Transactions on Transportation Electrification, vol. 8, no. 4, pp. 4303-4312, Dec. 2022, doi: 10.1109/TTE.2022.3167797.

[7] R. Notari, G. Devito, F. Bernardi, M. Pastura, D. Barater and S. Nuzzo, "Optimal Sizing of Hairpin Conductors in highway operation with PWM power supply," 2023 IEEE Workshop on Electrical Machines Design, Control and Diagnosis (WEMDCD), Newcastle upon Tyne, United Kingdom, 2023, pp. 1-6, doi: 10.1109/WEMDCD55819.2023.10110896.

[8] G. Devito, S. Nuzzo, D. Barater, “Trends of Electric Motor Technologies and Their Role in Sustainable Automotive Design”. IEEE Industrial Electronics Magazine. Submitted to peer review process.

[9] G. Devito, S. Nuzzo, D. Barater, G. Franceschini, L. Papini and P. Bolognesi, "Design of the Propulsion System for a Formula SAE racing car based on a Brushless Motor," 2021 IEEE Workshop on Electrical Machines Design, Control and Diagnosis (WEMDCD), Modena, Italy, 2021, pp. 318-324, doi:

10.1109/WEMDCD51469.2021.9425626. (During the research fellow period - 2020/2021).

[10] Directorate-General for Research and Innovation, “Transport Electrification of the Transport System – Study and reports,” 2017. [Online]. Available: https://op.europa.eu/en/publication-detail/-/publication/253937e1-fff0-11e7-b8f5-01aa75ed71a1/language-en/format-PDF. [Accessed: Nov. 24, 2020].

[11] Reducing Europe’s reliance on REs, 2024. [Online]. Available: https://cordis.europa.eu/article/id/442771-reducing-europe-s-reliance-on-rare-earths. [Accessed: Oct. 23, 2024].

[12] S. S. H. Bukhari, G. J. Sirewal, M. Ayub, and J. -S. Ro, "A New Small-Scale Self-Excited Wound Rotor Synchronous Motor Topology," in IEEE Transactions on Magnetics, vol. 57, no. 2, pp. 1-5, Feb. 2021, Art no. 8200205, doi: 10.1109/TMAG.2020.3009372.

[13] W. Chai, H. -M. Yang, F. Xing, and B. -i. Kwon, "Analysis and Design of a PM-Assisted Wound Rotor Synchronous Machine With Reluctance Torque Enhancement," in IEEE Transactions on Industrial Electronics, vol. 68, no. 4, pp. 2887-2897, April 2021, doi: 10.1109/TIE.2020.2982100.

[14] F-SAE International, “Rules 2020.” [Online]. Available: https://www.fsaeonline.com/cdsweb/app/NewsItem.aspx?NewsItemID=2c1ab552-40c3-4b97-a258-582dca0ea505. [Accessed: Nov. 24, 2020].

[15] A. Tokosch, D. Hake, K. Meah, and J. Maier, “Design and Implementation of a Drivetrain for an FSAE Electric Vehicle,” in 2019 IEEE International Conference on Environment and Electrical Engineering and 2019 IEEE Industrial and Commercial Power Systems Europe (EEEIC / I&CPS Europe), Genova, Italy, 2019, pp. 1-4.

[16] P. B. Reddy, T. M. Jahns, P. J. McCleer, and T. P. Bohn, “Design analysis and fabrication of a high-performance fractional-slot concentrated winding surface PM machine,” in 2010 IEEE Energy Conversion Congress and Exposition, Atlanta, GA, 2010, pp. 1074-1081.

[17] A. F. Venzon, R. Carlson, and N. Sadowski, “Design And Optimization Of A Brushless Motor Applied To A Formula SAE Vehicle,” in IEEE Latin America Transactions, vol. 18, no. 04, pp. 756-763, April 2020.

[18] M. Munaro, N. Bianchi, and G. Meneghetti, “The Formula SAE Electric Vehicle Competition: A High-Torque Density Permanent Magnet Motor,” in IEEE Industry Applications Magazine, vol. 26, no. 6, pp. 76-86, Nov.-Dec. 2020.

[19] X. Hu, H. Guo, H. Qian, X. Ding, and Y. Yang, “Development of a high-power-density motor for formula SAE electric race car,” in IECON 2017 - 43rd Annual Conference of the IEEE Industrial Electronics Society, Beijing, 2017, pp. 6618-6622.

[20] E. Carraro, M. Degano, M. Morandin, and N. Bianchi, “Formula SAE electric competition: Electrical motor design,” in 2013 International Electric Machines & Drives Conference, Chicago, IL, 2013, pp. 1142-1148.

[21]A. Vagati, M. Pastorelli, G. Franceschini, and C. Petrache, “Design of low-torque-ripple synchronous reluctance motors,” in IAS '97. Conference Record of the 1997 IEEE Industry Applications Conference Thirty-Second IAS Annual Meeting, New Orleans, LA, USA, 1997, pp. 286-293 vol.1.

[22]A. Arzillo et al., “Challenges and Future opportunities of Hairpin Technologies,” in 2020 IEEE 29th International Symposium on Industrial Electronics (ISIE), Delft, Netherlands, 2020, pp. 277-282.

[23]D. Jung, Y. Kim, U. Lee, and H. Lee, “Optimum Design of the Electric Vehicle Traction Motor Using the Hairpin Winding,” in 2012 IEEE 75th Vehicular Technology Conference (VTC Spring), Yokohama, 2012, pp. 1-4.

[24]M. Aydin and M. Gulec, “A New Coreless Axial Flux Interior Permanent Magnet Synchronous Motor With Sinusoidal Rotor Segments,” in IEEE Transactions on Magnetics, vol. 52, no. 7, pp. 1-4, July 2016.

[25]M. Onsal, Y. Demir, and M. Aydin, “A New Nine-Phase Permanent Magnet Synchronous Motor With Consequent Pole Rotor for High-Power Traction Applications,” in IEEE Transactions on Magnetics, vol. 53, no. 11, pp. 1-6, Nov. 2017.

[26]Q. H. Quadri, S. Nuzzo, C. Gerada, and M. Galea, “Analysis and Modelling of High Frequency Effects on Synchronous Generator’s Armature Conductors,” in 2020 IEEE 29th International Symposium on Industrial Electronics (ISIE), Delft, Netherlands, 2020, pp. 253-258.

[27]Avon Tyres, “Formula Student SAE.” [Online]. Available: https://www.avontyres.com/it-it/cura-pneumatici/dati-tecnici-moto-sportive/tyre-applications/SAE-Formula-Student/. [Accessed: Nov. 24, 2020].

[28]V. B. Honsinger, “Sizing Equations for Electrical Machinery,” in IEEE Transactions on Energy Conversion, vol. EC-2, no. 1, pp. 116-121, March 1987.

[29]B. W. Steyaert, E. Swint, W. W. Pennington, and M. Preindl, "Piecewise Affine Modeling of Wound-Rotor Synchronous Machines for Real-Time Motor Control," in IEEE Transactions on Industrial Electronics, vol. 70, no. 6, pp. 5571-5580, June 2023, doi: 10.1109/TIE.2022.3196352.

[30]S. Ahmed, M. R. Siddiqi, Q. Ali, T. Yazdan, A. Hussain, and J. Hur, "Brushless Wound Rotor Synchronous Machine Topology Using Concentrated Winding for Dual Speed Applications," in IEEE Access, vol. 11, pp. 119560-119567, 2023, doi: 10.1109/ACCESS.2023.3327525.

[31]V. Dmitrievskii, V. Prakht, E. Valeev, A. Paramonov, V. Kazakbaev, and A. Anuchin, "Comparative Study of Induction and Wound Rotor Synchronous Motors for the Traction Drive of a Mining Dump Truck Operating in Wide Constant Power Speed Range," in IEEE Access, vol. 11, pp. 68395-68409, 2023, doi: 10.1109/ACCESS.2023.3292244.

[32]V. Dmitrievskii, V. Prakht, E. Valeev, A. Paramonov, V. Kazakbaev, and A. Anuchin, "Comparative Study of Induction and Wound Rotor Synchronous Motors for the Traction Drive of a Mining Dump Truck Operating in Wide

Constant Power Speed Range," in IEEE Access, vol. 11, pp. 68395-68409, 2023, doi: 10.1109/ACCESS.2023.3292244.

[33]R. Chattopadhyay and I. Husain, "High Saliency Ratio Segmented Rotor Wound Field Synchronous Machine for Traction Applications," 2023 IEEE International Electric Machines & Drives Conference (IEMDC), San Francisco, CA, USA, 2023, pp. 1-7, doi: 10.1109/IEMDC55163.2023.10239061.

[34]G. Petrelli, G. Cutuli, S. Nuzzo, D. Barater, T. Zou, and C. Gerada, "On Comparing Aluminum and Copper in Wound Field Synchronous Motors for Traction Applications,", to be pulished.

[35]P. Ragazzo, S. Ferrari, N. Rivière, M. Popescu and G. Pellegrino, "Efficient Multiphysics Design Workflow of Synchronous Reluctance Motors," 2020 International Conference on Electrical Machines (ICEM), Gothenburg, Sweden, 2020, pp. 2507-2513, doi: 10.1109/ICEM49940.2020.9270670.

[36]P. Lindh, J. Montonen, M. G. Tehrani and J. Pyrhönen, "Design process of a traction motor for a hybrid bus application," 2014 Electric Power Quality and Supply Reliability Conference (PQ), Rakvere, Estonia, 2014, pp. 255-258, doi: 10.1109/PQ.2014.6866823.

[37]P. Quassolo, F. Togni, E. Preci and A. Acquaviva, "Design Considerations For High Power Density Traction PM Motors With Hairpin Windings," 2022 International Conference on Electrical Machines (ICEM), Valencia, Spain, 2022, pp. 1669-1674, doi: 10.1109/ICEM51905.2022.9910656.

[38]D. Yu, X. Y. Huang, Y. T. Fang and J. Zhang, "Design and comparison of interior permanent magnet synchronous traction motors for high speed railway applications," 2017 IEEE Workshop on Electrical Machines Design, Control and Diagnosis (WEMDCD), Nottingham, UK, 2017, pp. 58-62, doi: 10.1109/WEMDCD.2017.7947724.

[39]Z. Zhang, "Dual Three Phase Rare-Earth Free Spoke-Type Permanent Magnet Synchronous Traction Motor Using Ferrite Magnets," 2020 IEEE Energy Conversion Congress and Exposition (ECCE), Detroit, MI, USA, 2020, pp. 1814-1821, doi: 10.1109/ECCE44975.2020.9235965.

[40]D. Zarko, S. Stipetic, M. Martinovic, M. Kovacic, T. Jercic and Z. Hanic, "Reduction of Computational Efforts in Finite Element-Based Permanent Magnet Traction Motor Optimization," in IEEE Transactions on Industrial Electronics, vol. 65, no. 2, pp. 1799-1807, Feb. 2018, doi: 10.1109/TIE.2017.2736485.

[41]D. S. Yadav and M. Manisha, "Electric Propulsion Motors: A Comparative Review for Electric and Hybrid Electric Vehicles," 2022 IEEE International Conference on Distributed Computing and Electrical Circuits and Electronics (ICDCECE), Ballari, India, 2022, pp. 1-6, doi: 10.1109/ICDCECE53908.2022.9793099.

[42]E. Sokolov, "Comparative study of electric car traction motors," 2017 15th International Conference on Electrical Machines, Drives and Power Systems

(ELMA), Sofia, Bulgaria, 2017, pp. 348-353, doi: 10.1109/ELMA.2017.7955461.

[43]S. Paul, J. -G. Lee, V. -K. Tran, P. -W. Han, J. Chang and Y. -D. Chun, "Electromagnetic Design and Thermal Analysis of Totally Enclosed Air Over Cooled Permanent Magnet Synchronous Motor for High-Speed Railway Distributed Traction," 2022 International Conference on Electrical Machines (ICEM), Valencia, Spain, 2022, pp. 373-379, doi: 10.1109/ICEM51905.2022.9910928.

[44]A. Fatemi, D. M. Ionel, M. Popescu, Y. C. Chong and N. A. O. Demerdash, "Design Optimization of a High Torque Density Spoke-Type PM Motor for a Formula E Race Drive Cycle," in IEEE Transactions on Industry Applications, vol. 54, no. 5, pp. 4343-4354, Sept.-Oct. 2018, doi: 10.1109/TIA.2018.2844804.

[45]M. Pastura, R. Notari, S. Nuzzo, D. Barater and G. Franceschini, "On the AC Losses in the End Conductors of Hairpin Windings," 2022 International Conference on Electrical Machines (ICEM), Valencia, Spain, 2022, pp. 1150-1155, doi: 10.1109/ICEM51905.2022.9910862.

[46]G. Petrelli, S. Nuzzo, D. Barater, T. Zou, G. Franceschini and C. Gerada, "Preliminary Sensitivity Analysis and Optimisation of a Wound Field Synchronous Motor for Traction Applications," 2023 AEIT International Conference on Electrical and Electronic Technologies for Automotive (AEIT AUTOMOTIVE), Modena, Italy, 2023, pp. 1-6, doi: 10.23919/AEITAUTOMOTIVE58986.2023.10217237.

[47]G. Cutuli, S. Nuzzo, T. Zou, G. Franceschini, C. Gerada and D. Barater, "Multi-objective Optimizations of Copper and Aluminum Hairpin Windings: a Comparison," 2023 IEEE Energy Conversion Congress and Exposition (ECCE), Nashville, TN, USA, 2023, pp. 3796-3801, doi: 10.1109/ECCE53617.2023.10362293.

[48]S. Nuzzo, D. Barater, C. Gerada and P. Vai, "Hairpin Windings: An Opportunity for Next-Generation E-Motors in Transportation," in IEEE Industrial Electronics Magazine, vol. 16, no. 4, pp. 52-59, Dec. 2022, doi: 10.1109/MIE.2021.3106571.

[49]G. Petrelli, S. Nuzzo, T. Zou, D. Barater, G. Franceschini and C. Gerada, "Review and Future Developments of Wound Field Synchronous Motors in Automotive," 2023 IEEE International Conference on Electrical Systems for Aircraft, Railway, Ship Propulsion and Road Vehicles & International Transportation Electrification Conference (ESARS-ITEC), Venice, Italy, 2023, pp. 1-6, doi: 10.1109/ESARS-ITEC57127.2023.10114826.

[50]N. F. Quattromini, G. Petrelli, S. Nuzzo, D. Barater, and C. Rossi, "Power Take-Off Electrification through Power Flow Analysis of a Specialized Tractor,", Under review on Transaction Transportation Electrification (TTE).

[51]D. Troncon and L. Alberti, “Case of Study of the Electrification of a Tractor: Electric Motor Performance Requirements and Design,” Energies, vol. 13, no. 9, 2020, doi: 10.3390/en13092197.

[52]A .F. Soofi, S. D. Manshadi and A. Saucedo, “Farm electrification: Aroad-map to decarbonize the agriculture sector,” The Electricity Journal, vol. 35, issue 2, 2022, doi: 10.1016/j.tej.2022.107076.

[53]D. Debroy and M. Bayya, "Systems Engineering Approach for Design of an Electric Tractor," 2023 IEEE 11th Region 10 Humanitarian Technology Conference (R10-HTC), Rajkot, India, 2023, pp. 952-955, doi: 10.1109/R10-HTC57504.2023.10461829.

[54]Armold magnetics, “Results”. [Online]. Available in: https://www.arnoldmagnetics.com/products/neodymium-iron-boron-magnets/. [Accessed Jul. 26, 2024]

[55]Krings and C. Monissen, "Review and Trends in Electric Traction Motors for Battery Electric and Hybrid Vehicles," 2020 International Conference on Electrical Machines (ICEM), Gothenburg, Sweden, 2020, pp. 1807-1813, doi: 10.1109/ICEM49940.2020.9270946.

[56]Barcaro M, Meneghetti G, Bianchi N. Structural analysis of the interior PM rotor considering both static and fatigue loading. IEEE Trans Ind Appl 2014; 50: 253–260. DOI:10.1109/TIA.2013.2268048.

[57]Gangl P. Sensitivity-Based Topology and Shape Optimization with Application to Electric Motors. 2018; 317–340. DOI:10.1007/978-1-4939-8636-1_9.

[58]Zhu X, Wu W, Quan L, et al. Design and Multi-Objective Stratified Optimization of a Less-Rare-Earth Hybrid Permanent Magnets Motor With High Torque Density and Low Cost. IEEE Trans Energy Convers 2018; 34: 1178–1189. DOI:10.1109/TEC.2018.2886316.

[59]Huang S, Zhang J, Gao J, et al. Optimization the electromagnetic torque ripple of permanent magnet synchronous motor. Proc - Int Conf Electr Control Eng ICECE 2010 2010; 3969–3972. DOI:10.1109/iCECE.2010.967.

[60]Dai J, Chang S, Liu L. Optimization analysis of electromagnetic linear actuator’s radial array permanent magnets. Int J Appl Electromagn Mech 2015; 47: 441–451. DOI:10.3233/JAE-140054.

[61]Credo A, Fabri G, Villani M, et al. Adopting the Topology Optimization in the Design of High-Speed Synchronous Reluctance Motors for Electric Vehicles. IEEE Trans Ind Appl 2020; 56: 5429–5438. DOI:10.1109/TIA.2020.3007366.

[62]Abdallah SH, Tounsi S. Geometric Optimization Improving Performances of Permanent Magnet Synchronous Motors Using Analytical and Finite Element Methods Combined. SAE Int J Electrified Veh 2021; 11: 14-11-01–0004. DOI:10.4271/14-11-01-0004.

[63]Kant K, Kirtley JL, Iyer LV, et al. Finite Element Simulation-Based Design Optimization of Permanent Magnet Motors considering Drive Cycle. SAE Int J Altern Powertrains 2021; 7: 14-10-02–0012. DOI:10.4271/14-10-02-0012.

[64]Chang-Chou Hwang, Cho YH. Effects of leakage flux on magnetic fields of interior permanent magnet synchronous motors. IEEE Trans Magn 2001; 37: 3021–3024. DOI:10.1109/20.947055.

[65]Rao J, Qu R, Ma J, et al. Investigate the influence of magnetic bridge design on mechanical strength and electromagnetic characteristics in high speed IPM machines. 2014 17th Int Conf Electr Mach Syst ICEMS 2014 2014; 22–27. DOI:10.1109/ICEMS.2014.7013444.

[66]Al-Ani M, Paciura K, McQueen A, et al. Multi-physics Design Optimisation of PM-assisted Synchronous Reluctance Motor for Traction Application. IECON 2019 - 45th Annu Conf IEEE Ind Electron Soc 2019; 1: 4353–4359. DOI:10.1109/IECON.2019.8926697.

[67]Di Nardo M, Galea M, Gerada C, et al. Multi-physics optimization strategies for high speed synchronous reluctance machines. 2015 IEEE Energy Convers Congr Expo ECCE 2015 2015; 2813–2820. DOI:10.1109/ECCE.2015.7310054.

[68]Di Nardo M, Lo Calzo G, Galea M, et al. Design Optimization of a High-Speed Synchronous Reluctance Machine. IEEE Trans Ind Appl 2018; 54: 233–243. DOI:10.1109/TIA.2017.2758759.

[69]Lin R, Sudhoff SD, Nascimento VCD. A Multi-Physics Design Method for V-Shape Interior Permanent-Magnet Machines Based on Multi-Objective Optimization. IEEE Trans Energy Convers 2020; 35: 651–661. DOI:10.1109/TEC.2019.2958928.

[70]Timoshenko SP. On the correction for shear of the differential equation for transverse vibrations of prismatic bars. London, Edinburgh, Dublin Philos Mag J Sci 1921; 41: 744–746. DOI:10.1080/14786442108636264.

[71]Ou J, Liu Y, Breining P, et al. Study of the Electromagnetic and Mechanical Properties of a High-silicon Steel for a High-speed Interior PM Rotor. In: 2019 22nd International Conference on Electrical Machines and Systems (ICEMS). IEEE, 2019, pp. 1–4. DOI:10.1109/ICEMS.2019.8921800.

[72]Pedersen NL. Stress concentration and optimal design of pinned connections. J Strain Anal Eng Des 2019; 54: 95–104. DOI:10.1177/0309324719842766.

[73]Guiducci A, Barbieri SG, Nuzzo S, et al. Refined Structural Design and Thermal Analyses of a High-Speed Wound-Field Generator for the More Electrical Aircraft. In: 2023 IEEE Workshop on Electrical Machines Design, Control and Diagnosis (WEMDCD). IEEE, pp. 1–6. DOI: 10.1109/WEMDCD55819.2023.10110937.

[74]Formula ata, “Event Info”. [Online]. Available in: https://www.formula-ata.it/. [Accessed Nov. 24, 2020].

[75]A. Guiducci et al., "Refined Structural Design and Thermal Analyses of a High-Speed Wound-Field Generator for the More Electrical Aircraft," 2023 IEEE Workshop on Electrical Machines Design, Control and Diagnosis (WEMDCD), Newcastle upon Tyne, United Kingdom, 2023, pp. 1-6, doi: 10.1109/WEMDCD55819.2023.10110937.

[76]Jiang, J., Tian, Y., and Meng, Y., 2011, “Role of External Magnetic Field during 721 Friction of Ferromagnetic Materials”, Wear, 271(11–12), pp. 2991–2997. 722 DOI:10.1016/j.wear.2011.07.003.

[77]M. Barcaro and N. Bianchi, "Interior PM machines using Ferrite to substitute rare-earth surface PM machines," 2012 XXth International Conference on Electrical Machines, Marseille, France, 2012, pp. 1339-1345, doi: 10.1109/ICElMach.2012.6350051.

[78]D. -K. Woo and B. H. Jeong, "Irreversible Demagnetization of Permanent Magnet in a Surface-Mounted Permanent Magnet Motor With Overhang Structure," in IEEE Transactions on Magnetics, vol. 52, no. 4, pp. 1-6, April 2016, Art no. 8102606, doi: 10.1109/TMAG.2015.2476782.

[79]P. Liang, F. Chai, K. Shen and W. Liu, "Thermal design and optimization of a water-cooling permanent magnet synchronous in-wheel motor," 2019 22nd International Conference on Electrical Machines and Systems (ICEMS), Harbin, China, 2019, pp. 1-6, doi: 10.1109/ICEMS.2019.8922510.

[80]G. D. Demetriades, H. Zelaya De La Parra, E. Andersson and H. Olsson, "A Real-Time Thermal Model of a Permanent Magnet Synchronous Motor Based on geometrical measures," 2008 IEEE Power Electronics Specialists Conference, Rhodes, Greece, 2008, pp. 3061-3067, doi: 10.1109/PESC.2008.4592420.

[81]“Applications: NEWAGE: Stamford: Avk,” STAMFORD. [Online]. Available: https://www.stamford-avk.com/alternators/applications. [Accessed: 12-Jan-2022].

[82]J. K. Nøland, S. Nuzzo, A. Tessarolo and E. F. Alves, "Excitation System Technologies for Wound-Field Synchronous Machines: Survey of Solutions and Evolving Trends," in IEEE Access, vol. 7, pp. 109699-109718, 2019, doi: 10.1109/ACCESS.2019.2933493.

[83]K.J. Yost, W. Perdikakis, BA Robbins e C. Kitzmiller, "Time Response of a De-energizing Aerospace Synchronous Generator," 2019 IEEE National Aerospace and Electronics Conference (NAECON) , Dayton, OH, USA, 2019, pagg. 1- 6, doi: 10.1109 / NAECON46414.2019.9058036.

[84]S. Nuzzo, M. Galea, C. Gerada, D. Gerada, A. Mebarki and N. L. Brown, "Damper cage loss reduction and no-load voltage THD improvements in salient-pole synchronous generators," 8th IET International Conference on Power Electronics, Machines and Drives (PEMD 2016), 2016, pp. 1-7, doi: 10.1049/cp.2016.0203.

[85]S. Nuzzo, P. Bolognesi, G. Decuzzi, P. Giangrande and M. Galea, "A Consequent-Pole Hybrid Exciter for Synchronous Generators," in IEEE Transactions on Energy Conversion, vol. 36, no. 1, pp. 368-379, March 2021, doi: 10.1109/TEC.2020.3012198.

[86]H. M. Woo and D. Lee, "Starting and Dynamic Performance of a Parallel Field Rotor Type Hybrid Generator with PM Exciter," 2019 IEEE International Conference on Industrial Technology (ICIT), Melbourne, VIC, Australia, 2019, pp. 317-322, doi: 10.1109/ICIT.2019.8755225.

[87]S. McDonald, "Hybrid excitation of synchronous generators for wind turbines," 2nd IET Renewable Power Generation Conference (RPG 2013), Beijing, 2013, pp. 1-4, doi: 10.1049/cp.2013.1861.

[88]J. F. Hansen and F. Wendt, "History and State of the Art in Commercial Electric Ship Propulsion, Integrated Power Systems, and Future Trends," in Proceedings of the IEEE, vol. 103, no. 12, pp. 2229-2242, Dec. 2015, doi: 10.1109/JPROC.2015.2458990.

[89]Y. Wang, S. Nuzzo, H. Zhang, W. Zhao, C. Gerada and M. Galea, "Challenges and Opportunities for Wound Field Synchronous Generators in Future More Electric Aircraft," in IEEE Transactions on Transportation Electrification, vol. 6, no. 4, pp. 1466-1477, Dec. 2020, doi: 10.1109/TTE.2020.2980189.

[90]S. Nuzzo, P. Bolognesi, C. Gerada and M. Galea, "Simplified Damper Cage Circuital Model and Fast Analytical–Numerical Approach for the Analysis of Synchronous Generators," in IEEE Transactions on Industrial Electronics, vol. 66, no. 11, pp. 8361-8371, Nov. 2019, doi: 10.1109/TIE.2018.2885737.

[91]A.M. Knight, H. Karmaker and K. Weeber, "Use of a permeance model to predict force harmonic components and damper winding effects in salient-pole synchronous machines", IEEE Trans. Energy Convers., vol. 17, no. 4, pp. 709-716, Dec. 2002.

[92]H. Karmaker and A. M. Knight, "Investigation and simulation of fields in large salient-pole synchronous machines with skewed stator slots", IEEE Trans. Energy Convers., vol. 20, no. 3, pp. 604-610, Sep. 2005.

[93]A.Tessarolo, C. Bassi and D. Giulivo, "Time-stepping finite-element analysis of a 14-MVA salient-pole shipboard for different damper winding design solution", IEEE Trans. Ind. Electron., vol. 59, no. 6, pp. 2524-2535, Jun. 2012.

[94]G. Traxler-Samek, T. Lugand and A. Schwery, "Additional losses in the damper winding of large hydrogenerators at open-circuit and load conditions", IEEE Trans. Ind. Electron., vol. 57, no. 1, pp. 154-160, Jan. 2010.

[95]K. Diao, X. Sun, G. Lei, G. Bramerdorfer, Y. Guo and J. Zhu, "Robust Design Optimization of Switched Reluctance Motor Drive Systems Based on System-Level Sequential Taguchi Method," in IEEE Transactions on Energy Conversion, doi: 10.1109/TEC.2021.3085668.

[96]H. Karmaker e AM Knight, "Investigation and Simulation of fields in large salient-pole synchronous Machines with skeked stator slot", in IEEE Transactions on Energy Conversion , vol. 20, n. 3, pagg. 604-610, settembre 2005, doi: 10.1109 / TEC.2005.852955.

[97]S. Luo, Y. Jian and Q. Gao, "Synchronous generator modeling and semi - physical simulation," 2019 22nd International Conference on Electrical Machines and Systems (ICEMS), 2019, pp. 1-6, doi: 10.1109/ICEMS.2019.8921721.

[98]G. Harb, M. Arnaout, L. Hatab and M. Ramadan, "Two-dimensional analytical modeling of permanent magnet synchronous generator," 2017 29th International

Conference on Microelectronics (ICM), 2017, pp. 1-4, doi: 10.1109/ICM.2017.8268856.

[99] S. Nuzzo, M. Galea, C. Gerada and N. Brown, "Analysis, Modeling, and Design Considerations for the Excitation Systems of Synchronous Generators," in IEEE Transactions on Industrial Electronics, vol. 65, no. 4, pp. 2996-3007, April 2018, doi: 10.1109/TIE.2017.2756592.

[100] S. Nuzzo, P. Bolognesi, M. Galea and D. Barater, "An Improved Automatic Voltage Regulator for Self-Excited, Small-to-Medium Power Generating Sets equipped with Brushless Excitation Systems," IECON 2019 - 45th Annual Conference of the IEEE Industrial Electronics Society, 2019, pp. 904-909, doi: 10.1109/IECON.2019.8927675.

[101] Q. Y. Wang and A. Moshref, "Saturation factors and T'do in WECC/NERC generator model validation," 2011 24th Canadian Conference on Electrical and Computer Engineering(CCECE), 2011, pp. 000593-000596, doi: 10.1109/CCECE.2011.6030520.